May 2015

A STUDY OF CERTAIN ELECTROMAGNETIC INTERACTIONS AMONG HIGH OPTICAL CONDUCTIVITY NANOSPHERES AND DIELECTRIC HALF-SPACES

Satvik Navin Wani
Syracuse University

ABSTRACT

Electromagnetic coupling between a sphere and a semi-infinite substrate, and among several spheres present in the form of a composite were studied in this dissertation. Specifically, spheres made of noble metals such as Ag, Au and Cu and relatively high refractive index substrates and composite matrices. Such interactions need to be studied in order to understand and be able to design better devices such as plasmonic light devices as well as composites and fluids that have suspended plasmonic nanoparticles that have recently been shown to be technologically relevant in the context of device processing technologies and fluidic devices. For a sphere present near a relatively high refractive index substrate, coupling effects were found to significantly change the value of the induced electric dipole moment. It was found that the radiated power had a very strong dependence on the distance between the sphere and the substrate as well as the polarization and the angle of the incident plane wave. The wavelength dependence was also found to change significantly allowing access to regions of relatively larger values of the wavelength for the same material system and incident field as well as wavelength selective amplification of the response. The linear response of plasmonic composites was studied using an effective medium approximation. The effective permittivity was calculated using an effective medium model that was sensitive to a random composite's radial distribution function. The effect of the size of the monodisperse spheres, their volume fraction and material constituents were studied. A strong dependence on the microstructure was found for composites made of a relatively large refractive index matrix.

A STUDY OF CERTAIN ELECTROMAGNETIC INTERACTIONS AMONG HIGH OPTICAL CONDUCTIVITY NANOSPHERES AND DIELECTRIC HALF-SPACES

By

Satvik N Wani

(MS, Chemical Engineering, Washington University in St. Louis, 2010)

DISSERTATION

Submitted in partial fulfillment of the requirements for the degree of

Doctor of Philosophy in Chemical Engineering

Syracuse University

May 2015

CONTENTS

TABLE OF FIGURES

1 INTRODUCTION

1.1 INTRODUCTION

Metals such as Al, Ag, Au and Cu have a relatively high conduction electron concentration that renders them good conductors of electricity even at frequencies that lie in the optical range ($O(10^{14})$ Hz). The electrons in such materials can be, typically, modeled as a gas, i.e., electron-electron correlations can be neglected [1]. The metal can be seen as plasma of positive ions and negative electrons. Nanoparticles of such metals can sustain a localized plasma resonance that, in some sense, results from a damped harmonic oscillator system made of electrons (mass), nuclear binding (harmonic force) and finite conductivity (damping). The metals' electric permittivity ε_D can be modeled with the Drude model as follows [1].

$$\varepsilon_D = 1 - \frac{\omega_P^2}{\omega^2 + i\omega\omega_C}. \tag{1.1}$$

Here, ω is the angular frequency of incident radiation, ω_p is the plasma frequency of the metal and ω_C is the collision frequency that corresponds to resistive damping. The real part $\mathrm{Re}[\varepsilon_D]$ is a negative number for frequencies larger than the plasma frequency and the imaginary part $\mathrm{Im}[\varepsilon_D]$ is a positive in that range. For the metals considered here, this is valid for the ultraviolet-visible-near-infrared region of the electromagnetic spectrum. The electric polarizability per unit volume of a nanosphere of such a material that is small compared to the wavelength of incident radiation (rigorously, $k^* a \to 0$, $k^* \equiv \sqrt{\frac{\varepsilon_p}{\varepsilon_m}}\frac{2\pi}{\lambda}$ and a is the sphere radius [2]) is given by

$$\beta = \left(\frac{\varepsilon_p - \varepsilon_m}{\varepsilon_p + 2\varepsilon_m} \right) \tag{1.2}$$

where, ε_p is the permittivity of the material and ε_m is the permittivity of the embedding medium. A resonance can be seen in the β vs. λ curve for Ag, Au and Cu nanospheres. Their permittivities are shown in Fig.1 and the calculated values of β are shown in Fig. 2. Ag has the least $\mathrm{Im}[\varepsilon_p]$ and consequently the most prominent values of β. Medium permittivity was assumed to be $\varepsilon_m = 7$ so that the resonance peak of $\mathrm{Im}[\beta]$ occurs approximately in the middle of the visible spectrum at $\lambda \approx 600$ nm. Transparent high refractive index materials such as TiO_2, ZnO, Si_3N_4, etc. have similar values of real permittivity.

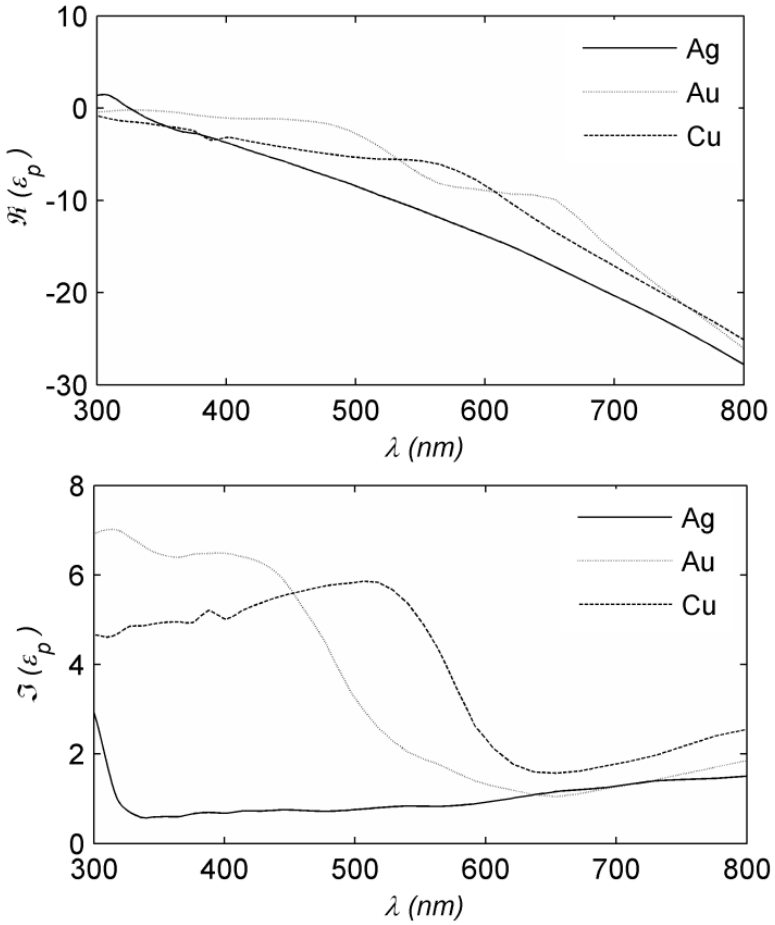

Figure 1.1: Permittivity ε_p for various optical conductivity metals Ag, Au and Cu. Ag has the least imaginary permittivity over a broad range of wavelengths. Permittivity data was taken from an online resource [3].

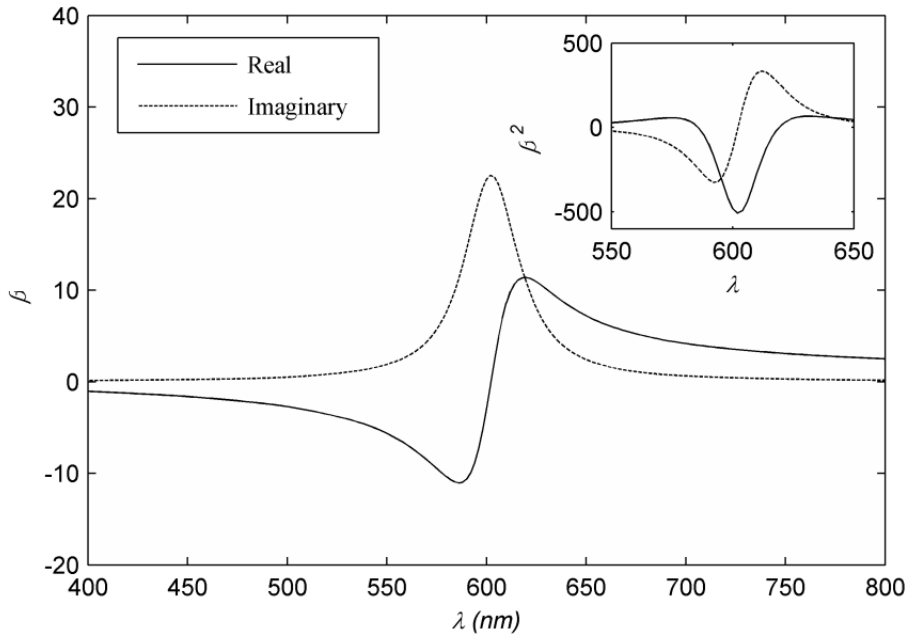

Figure 1.2: β for Ag spheres in a $\varepsilon_m = 7$ medium. Resonance occurs for $\lambda \approx 600$ nm and $\beta \approx 23i$. $\Im(\beta)$ is a small number away from resonance and $\Re(\beta)$ changes sign from negative to positive on moving from blue to red regions about resonance.

Electric field localization occurs at the poles outside a resonant sphere. A dipole resonance would lead to localization at the north and south poles for example. Inside, however, there is a uniform high energy density since the electric field inside small spheres is a constant vector as shown in Ref. [2]. The localized internal energy can be stored and/or transported. A 'plasmon' can store a quantum of energy for a period of time that is dependent on its plasmon decay time scale T_2. For Ag and Au nanoparticles, $T_2 = O(1)$ fs [4]. The energy can be released as radiation or heat depending on the experimental condition. Under steady state or for system time scales that are much larger than the plasmon lifetime, the energy transfer can be seen as a continuous process where there is no accumulation. Hence, a fraction of incident radiant energy can be dissipated as heat and the rest can be radiated away in a way that depends on the surrounding geometry. The

generated heat can be utilized for various applications where photo-thermal heating is required (see, for e.g. Ref. [5]). The radiatively dissipated energy can also be channelized into objects near such a nanoparticle. This is particularly interesting because the coupling of light that can be achieved through plasmonic nanostructures defies ray-optics and requires one to solve Maxwell-equations in the "near-field" region of a source. In other words, the so-called "Near-field" optics or nano-optics based approaches become necessary. Another feature of nano-optics worth noting is that the involved length scales are generally much smaller than the wavelength of the involved light. One popular application is wave-guiding of light into solar energy harvesting devices such as a solar cell [6-8]. The inverse situation that involves light generation through Light Emitting Diodes etc. can also benefit from this kind of radiative coupling. As a consequence, solar cells can generate more current, and LEDs can radiate more light [9] etc. These applications, in principle, only need a single nanostructure to interact with the device. Recently, field-coupled plasmon resonance or radiant excitation of two or more plasmonic nanostructures that are close to each other has become important due to special lineshapes of their optical spectra that resemble Fano resonance [2, 10-12]. Moreover, several basic questions related to the linear optical response of a bulk composite of plasmonic nanoparticles are also of interest. These include modeling approaches based on effective medium theories [13]. The models are not only important to just study the interesting optical response of plasmonic composites but also as a prediction, design and measurement device for application of such composites as optical filters, reflectors, scatterers and reconfigurable opto-fluids [14, 15].

In this work, the optical properties of coupled plasmonic structures will be investigated using theoretical and numerical analysis. In particular, (1) noble metal nanoparticulate coatings on dielectric substrates and (2) composites of such nanoparticles embedded in a dielectric matrix. The

dissertation contains six chapters. Mathematical aspects of electromagnetic coupling are described in some detail in Chap. 2, Chap. 3 contains information about the permittivity of several relevant materials. Chap. 4 contains the work related to (1), Chap. 5 contains the theoretical framework, results and discussion related to (2). Conclusions are offered in Chap. 6.

2 ELECTROMAGNETIC INTERACTIONS

2.1 INTRODUCTION

Dielectric objects interact directly with an optical frequency electromagnetic field by becoming polarized. The resulting perturbed field can have very interesting properties that may result in the development of several potential applications besides just being non-trivial. In this section, the mathematical and numerical methods, and involved approximations that are applicable for electromagnetic interactions between dielectric objects and an applied field will be discussed. The problem of interest involves non-magnetic spheres and semi-infinite slabs subject to an externally applied optical electromagnetic field.

2.1.1 Maxwell equations and plane waves

Maxwell equations relate the electric field **E**, the electric displacement field **D**, the magnetic field **H** and the magnetic induction field **B** to charge and current sources. They represent existing phenomenological laws such as the Gauss' law, Faraday's law and Ampere's law. The equations are given below.

$$\partial_i D_i = \rho^f , \tag{2.1a}$$

$$\partial_i B_i = 0, \tag{2.1b}$$

$$\varepsilon_{ijk}\partial_j E_k = -\partial_t B_i , \tag{2.1c}$$

and

$$\varepsilon_{ijk}\partial_j H_k = \partial_t D_i + J_i^f . \tag{2.1d}$$

The fields **D** and **B**, respectively, result upon the application of **E** and **H**. In an isotropic and local medium, i.e., a medium in which the applied field and its result are only related at specific point in space but can depend on values in the past, the material constants are called electric permittivity ε and magnetic permeability μ. This ε is not the same as the one in the Levi-Cevita symbol ε_{ijk}. The magnetic response is assumed to be the same as that of vacuum for the purpose of this work. It is a good approximation for optical frequencies in case of the materials of interest since their magnetic permittivity is very close to that of vacuum in the optical wavelength range. The fields are interrelated through the following constitutive relationships:

$$D_i(t) = \int_{-\infty}^{t} \varepsilon(t-\tau)\, E_i(\tau) d\tau, \tag{2.2a}$$

and

$$B_i = \mu_0 H_i . \tag{2.2b}$$

The subscript '0' denotes vacuum. Eq 2.2a for **D** can be Fourier transformed to give the following linear relationship between the corresponding Fourier amplitudes:

$$D_i(\omega) = \varepsilon(\omega) E_i(\omega). \tag{2.3}$$

In Eq 2.1a, the quantity ρ^f is the free charge density. It does not have a magnetic dual because there are no real magnetic monopoles or sources. The quantity $\mathbf{J}^f$ is known as the free

current density. It can be made to have a magnetic dual $\mathbf{M}^f$ that can appear on the right-hand side of curl of **E** equation (Eq. 2.1c). Since the interest is only in situations where the magnetic response is that of vacuum and there are no free surface charges or currents present, the source terms are disregarded from the very beginning of the current analyses. The curl equations contain time derivatives—for which we will assume, without loss of generality, that all the fields **F** (= **E**, **H**, **D** or **B**) can be represented as function of the position **r** and time *t*. For a given angular frequency ω, it is given by:

$$F_j(\mathbf{r},t) \equiv F_j(\mathbf{r})\exp(-i\omega t). \tag{2.4}$$

Under the time-harmonic assumption, one can eliminate the time derivatives in Eqs. 2.1c and d to give the following set of curl equations:

$$\varepsilon_{jkl}\partial_k E_l = i\omega\mu_0 H_j, \tag{2.5a}$$

and

$$\varepsilon_{jkl}\partial_k H_l = -i\omega\varepsilon E_j. \tag{2.5b}$$

They can be further simplified by eliminating **H** in the following way: first, a curl operation can be performed on Eq. 2.5a to give $\varepsilon_{jkl}\partial_k\varepsilon_{lmn}\partial_m E_n = \varepsilon_{jkl}\partial_k i\omega\mu_0 H_l$, followed by substitution of Eq. 2.5b in it to give $\varepsilon_{jkl}\partial_k\varepsilon_{lmn}\partial_m E_n = \omega^2\mu_0\varepsilon E_j$. Using the identity $\varepsilon_{jkl}\varepsilon_{lmn} = (\delta_{jm}\delta_{kn} - \delta_{jn}\delta_{km})$ along with the fact that in a source free medium $\partial_i E_i = 0$, the following equation can be derived: $[\partial_j\partial_j + \omega^2\mu_0\varepsilon]E_i = 0$. The wave number can be defined as $k^2 \equiv \omega^2\mu_0\varepsilon$ and the following wave equation can be derived:

$$[\partial_j \partial_j + k^2]E_i = 0. \tag{2.6}$$

It can be shown that Eq. 2.6 is valid for both **E** and **H**. Its solution in Cartesian co-ordinates will be briefly discussed here onward. Consider the following general solution:

$$E_j = E_j^0 \exp(ik_m x_m). \tag{2.7}$$

Here, **k** can be in any direction relative to $\mathbf{E}^0$. Even though it is required that $\partial_i E_i$ equal zero for the derivation of Eq. 2.6, the condition needs to be re-applied to the general solution. Upon application, $\partial_j E_j = (\partial_j E_j^0)\exp(ik_m x_m) + E_j^0 \exp(ik_m x_m) ik_m \partial_j x_m = 0$, which simplifies to give the following relationship between $\mathbf{E}^0$ and **k**:

$$E_i^0 k_i = 0. \tag{2.8}$$

At this point, it is not known which one of $\mathbf{E}^0$ and **k** is to be fixed. It can be shown that **k** is the one that needs to be fixed using the following argument.

> *In order for the solution to be called a plane wave of radiation, it needs to carry radiation in a specific direction—the direction along which the energy is transported. The solution should be consistent with the concept of radiation: it must emanate from a source and move away from it. Such a condition cannot be imposed on the electric field. So,* ***k*** *needs to be that direction since there are only two characteristic directions.*

A relationship between the amplitudes of the **H** and **E** wave solutions can be further derived by substituting Eq. 2.7 into Eq. 2.5a to evaluate H_j to be given by $H_j = \dfrac{\varepsilon_{jlm} k_l E_m^0}{\omega \mu_0} \exp(ik_n x_n)$. The

amplitudes of the two fields can be related by a comparison with Eq. 2.7 to give the following expression:

$$H_i^0 = \frac{1}{\omega\mu_0}\varepsilon_{ijl}k_j E_l^0. \tag{2.9}$$

Similar to Eq. 2.9, it can also be shown that $H_i^0 k_i = 0$ and from it, it can be further inferred that $E_i^0 H_i^0 = 0$ for such plane waves.

2.1.2 Boundary conditions

The boundary conditions for **E** and **H** can be derived from the Maxwell equations given in Eqs. 2.1. Using the divergence equations, one can show that for a a very small box whose two parallel sides are parallel to a boundary separating regions 1 and 2, the divergence theorem necessitates that

$$D_i n_i\big|_1 = D_i n_i\big|_2 \tag{2.10a}$$

and

$$B_i n_i\big|_1 = B_i n_i\big|_2 \tag{2.10b}$$

when the boundary contains no free charge. The curl equations, in conjunction with the Stokes' theorem, can lead to the boundary condition for the tangential components of the fields. For a boundary that separates regions 1 and 2 and contains no free current sources, one can show that

$$\mathbf{E}\times\hat{\mathbf{n}}\big|_1 = \mathbf{E}\times\hat{\mathbf{n}}\big|_2 \tag{2.11a}$$

and

$$\mathbf{H}\times\hat{\mathbf{n}}\big|_1 = \mathbf{H}\times\hat{\mathbf{n}}\big|_2. \tag{2.11b}$$

Here, $\hat{\mathbf{n}}$ represents the unit normal that is ascribed based on a consistent convention.

2.1.3 Energy in electromagnetic fields

In this section, the energy balance in the context of classical electromagnetics is discussed. Energy balance equations can be derived from the Maxwell curl equations given in Eqs. 2.1 by performing the following algebraic procedure [16]. Noticing that

$$\varepsilon_{ijk} H_i \partial_j E_k = -H_i \partial_t B_i, \tag{2.12a}$$

$$\varepsilon_{ijk} E_i \partial_j H_k = E_i \partial_t D_i \tag{2.12b}$$

and

$$\varepsilon_{ijk} \partial_i E_j H_k = \varepsilon_{ijk} H_i \partial_j E_k - \varepsilon_{ijk} E_i \partial_j H_k; \tag{2.12c}$$

it can be shown that

$$\partial_i S_i = \partial_t [u_E + u_H], \tag{2.13}$$

where $S_i \equiv \varepsilon_{ijk} E_j H_k$ is the Poynting vector, $u_E \equiv \frac{1}{2} E_i D_i$ is the electric energy density and $u_H \equiv \frac{1}{2} H_i B_i$ is the magnetic energy density. Here, **S** can be interpreted as the flux of energy that

balances the changes in the stored energies over time. Of course, a source term can be put on the left-hand side of Eq. 2.13, but for the purpose of this work, it won't be considered. Further, here, we want to make all the variables time-harmonic in order to simplify Eq. 2.13 by eliminating the time dependence. The time dependence of **S** can be removed by integrating over a time period for a given angular frequency ω. Since time harmonic variables are complex, it is required that only the real parts be considered so that complex **E** and **H** can be related to real variables such as **S**. The integral equals zero if the fields are assumed to have complex values. It can be shown that $\mathbf{S} \equiv \mathrm{Re}[\mathbf{E}] \times \mathrm{Re}[\mathbf{H}]$ can be analyzed since

$\mathrm{Re}[\mathbf{E}] \times \mathrm{Re}[\mathbf{H}] = \frac{1}{2}[\mathbf{E}e^{-i\omega t} + \mathbf{E}^* e^{-i\omega t}] \times \frac{1}{2}[\mathbf{H}e^{-i\omega t} + \mathbf{H}^* e^{-i\omega t}]$ and eventually, after some rearrangement,

$$\mathbf{S} = \frac{1}{2}\mathrm{Re}[(\mathbf{E} \times \mathbf{H})e^{-2i\omega t}] + \frac{1}{2}\mathrm{Re}[(\mathbf{E} \times \mathbf{H}^*)]. \tag{2.14}$$

Integration over a time-period yields [17]

$$\langle \mathbf{S} \rangle \equiv \frac{1}{2\pi}\int_0^{2\pi} \mathbf{S}d(\omega t) = \frac{1}{2}\mathrm{Re}[(\mathbf{E} \times \mathbf{H}^*)] = \frac{1}{2}\mathrm{Re}[(\mathbf{E}^* \times \mathbf{H})]. \tag{2.15}$$

Averaged Poynting flux $\langle \mathbf{S} \rangle$ will be denoted by **F** from here to differentiate between time-averaged and actual fluxes. Using a similar algebraic procedure described as Eqs. 2.14, it can be shown that the energy balance equation for time harmonic fields is

$$\partial_i F_i = -\frac{1}{2}\mathrm{Im}[\omega\{H_i^* B_i - E_i D_i^*\}]. \tag{2.16}$$

It can further be found that only the electric term contributes to the divergence of **F** in a medium where there is no magnetic dissipation and that only the electric term remains nonzero because of the presence an imaginary part in a medium's electric permittivity. Hence,

$$\partial_i F_i = -\frac{\omega}{2}\mathrm{Im}[\varepsilon]E_i E_i. \tag{2.17}$$

Since the imaginary part of the permittivity represents dissipation, a medium with such a permittivity behaves as a sink for the energy flux. In the presence of a source given by a current density J_i, Eqs. 2.14 can be adjusted to give the following equation:

$$\partial_i F_i + \frac{\omega}{2}\mathrm{Im}[\varepsilon]E_i E_i + \frac{1}{2}\mathrm{Re}[E_i J_i^*] = 0.$$

2.1.4 Interaction of plane waves with a semi-infinite dielectric interface

In this section, the interaction of a plane with a semi-infinite plane made of a dielectric material will be analyzed in order to be able to calculate the values of the fields outside and within the dielectric. It will be assumed, without loss of generality, that the plane wave is incident from outside the dielectric. Further, the following steps are used to define the problem:

- The plane interface has a unit normal $\mathbf{m}$ that points away from the interface—in the half-space from which the plane wave is incident. We will set $\mathbf{m} \equiv \delta_{j1}$ and the incident wave's wave vector as $\mathbf{k}^i$. We need $k_1^i < 0$ so that the wave is incident on to the dielectric half-plane located in $x_1 < 0$. Since $\mathbf{k}^i$ and $\hat{\mathbf{x}}_1$ form a unique plane, we

will let $\hat{\mathbf{x}}_3 \equiv \hat{\mathbf{x}}_1 \times \hat{\mathbf{k}}^i$ so that it points into the plane. $\hat{\mathbf{x}}_2$ Can be defined from this information. We will choose $k_2^i > 0$ without any loss of generality.

- In order to satisfy the boundary condition at the interface, we need to put another wave solution in the $x_1 < 0$ region. Since the plane waves contain a phase factor, the boundary conditions can be consistently satisfied only if $\exp(ik_j x_j) \mid j = 2,3$ is the same on both sides of the interface and for both wave solutions. Further, all $\mathbf{k}$s should lie in one plane—the plane containing $\mathbf{k}^i$ and $\hat{\mathbf{x}}_1$. We will denote the wave vector in the $x_1 < 0$ region as $\mathbf{k}^t$. We also require a third, reflected wave $\mathbf{k}^r$ because tangential components of **E** and **H** cannot simultaneously be made equal across the interface without a third wave. Since all $k_j^\mu, j = 2,3 \& \mu = i,r,t$ are equal, it follows that the angles made with $\hat{\mathbf{x}}_1$, $\theta^\mu, \mu = i,r$ are also equal. The condition is called the Snell's Law and can be expressed as:

$$k_j^i = k_j^r = k_j^t, \; j \neq 1 \tag{2.18}$$

for the current statement of the problem.

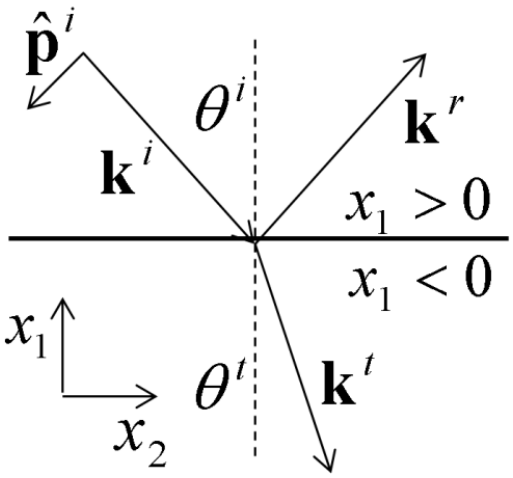

Figure 2.1: Orientations of the incident (*i*), reflected (*r*) and transmitted (*t*) wavevectors with respect to the axes, the interface with the dielectric half-plane and its normal. Only one polarization vector is shown since all other orientations can be found from its and the wavevector's orientations.

Fig. 2.1 shows how the $\mathbf{k}^{\mu}$ are oriented with respect to the dielectric interface as well as the relative orientation of the coordinate axes. In order to evaluate the fields, they need to be represented in some orthonormal vector basis that is based on the geometry of the problem. One unique direction is the one perpendicular to the plane—$\hat{\mathbf{x}}_3$. It can be called the transverse direction of polarization $\hat{\mathbf{p}}^{\mu T}$. An 'in plane' direction can be defined as $\hat{\mathbf{p}}^{\mu P} \equiv \hat{\mathbf{p}}^{\mu T} \times \hat{\mathbf{k}}^{\mu}$. The incident wave can be decomposed into two separate components based on which of **E** or **H** are in the $\hat{\mathbf{p}}^{\mu T}$ direction. So, one has:

$$\begin{aligned} \mathbf{E}^{iT} &= E^{i0}\hat{\mathbf{p}}^{iT}\exp(i\mathbf{k}^i\cdot\mathbf{r}), \\ \mathbf{H}^{iP} &= \frac{k^i}{\omega\mu_0}E^{i0}\hat{\mathbf{p}}^{iP}\exp(i\mathbf{k}^i\cdot\mathbf{r}), \end{aligned} \tag{2.19}$$

and,

$$\begin{aligned}\mathbf{H}^{iT} &= H^{i0}\hat{\mathbf{p}}^{iT}\exp(i\mathbf{k}^{i}\cdot\mathbf{r}),\\ \mathbf{E}^{iP} &= \frac{-k^{i}}{\omega\varepsilon}H^{i0}\hat{\mathbf{p}}^{iP}\exp(i\mathbf{k}^{i}\cdot\mathbf{r})\end{aligned} \tag{2.20}$$

with

$$\begin{aligned}\hat{\mathbf{p}}^{iT} &= \hat{\mathbf{x}}_3,\\ \hat{\mathbf{p}}^{iP} &= -\sin\theta^{i}\hat{\mathbf{x}}_1 - \cos\theta^{i}\hat{\mathbf{x}}_2.\end{aligned} \tag{2.21}$$

Reflection or transmission, it can be shown, cannot cause a TE wave to have a P component of **E** and vice versa so that the boundary condition is satisfied self-consistently for each type of wave. Alternatively, the T and P type decomposition of the waves remains valid for all waves in the problem—reflected and transmitted because of the uniqueness of the directions once $\mathbf{k}^{i}$ is fixed. In general, for Eqs. 2.17 and 2.18, the origin needs to be moved such that the interface is at $x_1 = 0.$ In case this is not done, a phase factor that arises from the exponential term will have to be incorporated into the complex amplitudes $E^{\mu 0}$ and $E^{\mu 0}$. There is also a phase factor that will come about based on the location of the point of incidence on the (2,3)-plane representing the interface. The same argument, as before, can be used here since the parallel components of $\mathbf{k}^{\mu}$ are equal. So, the related phase factor can be thought as being incorporated into the complex amplitudes of the waves—making the representation of the waves independent of the location of the point of incidence.

The reflected field is the following:

$$\begin{aligned}\mathbf{E}^{rT} &= R^{T}E^{i0}\hat{\mathbf{p}}^{rT}\exp(i\mathbf{k}^{r}\cdot\mathbf{r}),\\ \mathbf{H}^{rP} &= \frac{k^{r}}{\omega\mu_0}R^{T}E^{i0}\hat{\mathbf{p}}^{rP}\exp(i\mathbf{k}^{r}\cdot\mathbf{r}),\end{aligned} \tag{2.22}$$

and

$$\begin{aligned}\mathbf{H}^{rT} &= R^{P} H^{i0} \hat{\mathbf{p}}^{rT} \exp(i\mathbf{k}^{r} \cdot \mathbf{r}),\\ \mathbf{E}^{iP} &= \frac{-k^{r}}{\omega\varepsilon} R^{P} H^{i0} \hat{\mathbf{p}}^{rP} \exp(i\mathbf{k}^{r} \cdot \mathbf{r}),\end{aligned} \tag{2.23}$$

with

$$\begin{aligned}\hat{\mathbf{p}}^{rT} &= \hat{\mathbf{x}}_3,\\ \hat{\mathbf{p}}^{rP} &= -\sin\theta^{r}\hat{\mathbf{x}}_1 + \cos\theta^{r}\hat{\mathbf{x}}_2.\end{aligned} \tag{2.24}$$

The transmitted field is similarly given as:

$$\begin{aligned}\mathbf{E}^{tT} &= T^{T} E^{i0} \hat{\mathbf{p}}^{tT} \exp(i\mathbf{k}^{t} \cdot \mathbf{r}),\\ \mathbf{H}^{tP} &= \frac{k^{t}}{\omega\mu_0} T^{T} E^{i0} \hat{\mathbf{p}}^{tP} \exp(i\mathbf{k}^{t} \cdot \mathbf{r}),\end{aligned} \tag{2.25}$$

and

$$\begin{aligned}\mathbf{H}^{tT} &= T^{P} H^{i0} \hat{\mathbf{p}}^{tT} \exp(i\mathbf{k}^{t} \cdot \mathbf{r}),\\ \mathbf{E}^{tP} &= \frac{-k^{t}}{\omega\varepsilon} T^{P} H^{i0} \hat{\mathbf{p}}^{tP} \exp(i\mathbf{k}^{t} \cdot \mathbf{r}),\end{aligned} \tag{2.26}$$

With

$$\begin{aligned}\hat{\mathbf{p}}^{tT} &= \hat{\mathbf{x}}_3,\\ \hat{\mathbf{p}}^{tP} &= -\sin\theta^{t}\hat{\mathbf{x}}_1 - \cos\theta^{t}\hat{\mathbf{x}}_2.\end{aligned} \tag{2.27}$$

The coefficients R^{T}, R^{P}, T^{T} &T^{P} are introduced for the reflected and transmitted wave so that they can change their magnitude in order to accommodate the boundary conditions on **E** and **H**.

The letter *R* represents reflection coefficient and *T*, the transmission coefficient. Their values can be evaluated by applying the boundary conditions in the following manner:

Tangential **E** *continuity for* T *waves*

$$1 + R^T = T^T \tag{2.28}$$

Tangential **H** *continuity for* T *waves*

$$\cos\theta^i [1 - R^T] = \sqrt{\varepsilon_S} T^T \cos\theta^t \tag{2.29}$$

In a similar manner,

Tangential **E** *continuity for* P *waves*

$$1 + R^P = T^P \tag{2.30}$$

Tangential **H** *continuity for* P *waves*

$$\cos\theta^i [1 - R^P] = \frac{1}{\sqrt{\varepsilon_S}} T^P \cos\theta^t \tag{2.31}$$

The parameter ε_S is the relative electric permittivity of the substrate. It appears in Eqs. 2.28 and 2.30 because the ratios $\frac{k^t}{k^i}$ and $\frac{k^t}{k^r}$ are equal and have a value of $\sqrt{\varepsilon_S}$. The reflection angle θ^r does not seem to appear because it is equal to θ^i. Eqs. 2.27-30 can be solved to give the following relationships for $R^T, R^P, T^T \& T^P$.

$$
\begin{aligned}
T^T &= \frac{2\cos\theta^i}{\cos\theta^i + \sqrt{\varepsilon_S}\cos\theta^t}, \\
R^T &= \frac{\cos\theta^i - \sqrt{\varepsilon_S}\cos\theta^t}{\cos\theta^i + \sqrt{\varepsilon_S}\cos\theta^t},
\end{aligned}
\tag{2.32}
$$

$$
\begin{aligned}
T^P &= \frac{2\sqrt{\varepsilon_S}\cos\theta^i}{\sqrt{\varepsilon_S}\cos\theta^i + \cos\theta^t}, \\
R^P &= \frac{\sqrt{\varepsilon_S}\cos\theta^i - \cos\theta^t}{\sqrt{\varepsilon_S}\cos\theta^i + \cos\theta^t}.
\end{aligned}
\tag{2.33}
$$

Using Eqs. 2.31 and 2.32, the incident, reflected and transmitted electric field can be written as

$$
\begin{aligned}
\mathbf{E}^i &= (E^{i0T}\hat{\mathbf{p}}^{iT} + E^{i0P}\hat{\mathbf{p}}^{iP})\exp(i\mathbf{k}^i \cdot \mathbf{r}), \\
\mathbf{E}^r &= (R^T E^{i0T}\hat{\mathbf{p}}^{rT} + R^P E^{i0P}\hat{\mathbf{p}}^{rP})\exp(i\mathbf{k}^r \cdot \mathbf{r}), \\
\mathbf{E}^t &= (T^T E^{i0T}\hat{\mathbf{p}}^{tT} + T^P E^{i0P}\hat{\mathbf{p}}^{tP})\exp(i\mathbf{k}^t \cdot \mathbf{r}).
\end{aligned}
\tag{2.34}
$$

2.2 SOLUTIONS FOR A SPHERE

In this section the solution of Maxwell equations for a plane wave incident on a spherical particle made of a material that has a relative permittivity ε_p will be discussed. The solution requires working with spherical coordinate system for ease of analysis. Without loss of generality, we will have the sphere centered at the origin. Any effects of it not being at the origin will be accounted for by adjusting the phase and direction of the incident wave since the solution should only depend on the relative location of the sphere with respect to the wave. Moreover, it is rather difficult to work with spherical coordinates that are centered at a point that is not the centre of the spherical symmetry. The sphere or the medium around it do not contain any free charge or current that can contribute at sources in the Maxwell equations given in Eqs. 2.1—in other words, $\partial_i E_i = 0$ and so, one can work with

$$[\partial_j \partial_j + k^2]E_i = 0 \tag{2.35}$$

rather than $[\partial_j \partial_j + k^2]E_i - \partial_i \partial_l E_l = 0.$ We can decompose **E** and **H** or any field **F** into the following independent scalar fields—which in the spherical coordinate system take the following form:

$$\mathbf{F} = \nabla f + \nabla \times (\mathbf{r}\Psi) + \nabla \times \nabla \times (\mathbf{r}\Phi). \tag{2.36}$$

Here, $f, \Psi \,\&\, \Phi$ are scalar fields. In the context of Maxwell equations given in Eqs. 2.1, if we let **E**=**F**, we get the following equation for *f* since **E** is divergence free:

$$\nabla^2 f = 0. \tag{2.37}$$

The other scalar fields can be shown to be the solutions of the Helmholtz equations given in Eq. 2.35 allowing **F** to be given by

$$\mathbf{F} = \nabla \times (\mathbf{r}\Psi) + \nabla \times \nabla \times (\mathbf{r}\Phi). \tag{2.38}$$

It can further be observed that if one sets

$$\mathbf{E} = \nabla \times (\mathbf{r}\Psi) + \nabla \times \nabla \times (\mathbf{r}\Phi), \tag{2.39}$$

then, the equation for **H** is given by

$$\mathbf{H} = -i\omega\varepsilon \nabla \times (\mathbf{r}\Phi) + \frac{1}{i\omega\mu_0} \nabla \times \nabla \times (\mathbf{r}\Psi). \tag{2.40}$$

The scalar potentials are known as the toroidal and polodial potentials or Debye potentials depending on whether one is reading fluid-mechanics, hydrodynamics and/or plasma physics literature or electromagnetics literature. The solutions of the scalar Helmholtz equation in spherical coordinates can be found by separating the dependencies on $r, \theta \& \phi$. For Ψ, the solutions are:

$$\Psi(r,\theta,\phi) = \sum_{n=0}^{\infty} \sum_{m=-n}^{n} [A_{nm} j_n(kr) + B_{nm} y_n(kr)] Y_{nm}(\theta,\phi), \tag{2.41}$$

Where

$$Y_{nm}(\theta,\phi) = P_n^m(\cos\theta)\exp(im\phi). \tag{2.42}$$

The functions j_n and y_n are, respectively, the regular and singular spherical Bessel functions, Y_{nm} are the spherical harmonics and P_n^m are the associated Legendre polynomials. The representation in Eq. 2.42 allows *m* to take negative values by combining the $\sin(m\phi)$ and $\cos(m\phi)$ terms into a $\exp(im\phi)$ term. The amplitudes A_{nm} and B_{nm} are unknowns that need to be determined. Since the boundary conditions given in Eqs. 2.12 and 2.13 cannot be decoupled in terms of Ψ and $_\Phi$ for finite values of *k*, one has to work with the components of the **E** and **H** fields. The following components can be obtained from Eqs. 2.40 and 2.41[16]:

$$\begin{aligned} E_r &= [\partial_r^2 + k^2](r\Phi), \\ E_\theta &= \frac{1}{\sin\theta}\partial_\phi \Psi + \frac{1}{r}\partial_{r\theta}(r\Phi), \\ E_\phi &= -\partial_\theta \Psi + \frac{1}{r}\partial_{r\phi}(r\Phi), \end{aligned} \tag{2.43}$$

and

$$\begin{aligned} H_r &= \frac{1}{i\omega\mu_0}[\partial_r^2 + k^2](r\Psi), \\ H_\theta &= -\frac{i\omega\varepsilon}{\sin\theta}\partial_\phi \Phi + \frac{1}{i\omega\mu_0}\frac{1}{r}\partial_{r\theta}(r\Psi), \\ H_\phi &= i\omega\varepsilon\,\partial_\theta \Phi + \frac{1}{i\omega\mu_0}\frac{1}{r}\partial_{r\phi}(r\Psi). \end{aligned} \tag{2.44}$$

The incident field described by $E_j = E_j^0 \exp(ik_l x_l)$, has an arbitrarily oriented **k**. It can be fixed to be oriented along $\hat{\mathbf{X}}_1$ without loss of generality. Further, one can fix one of the polarization directions to be along $\hat{\mathbf{X}}_2$ and another along $\hat{\mathbf{X}}_3$, again, without a loss of generality. The difference in the algebra created because of the choice $\hat{\mathbf{X}}_2$ or $\hat{\mathbf{X}}_3$ is minor. So, for now, only **E**

polarization along $\hat{\mathbf{x}}_2$ will be analyzed. The incident field given by $E_2^i = E^0 \exp(ikr\cos\theta)$ has a *r*- component given by $E_r^i = E^0 \sin\theta\cos\phi\exp(ikr\cos\theta)$ that can be re-framed as:

$$E_r^i = -\frac{\cos\phi}{ikr} E^0 \partial_\theta [\exp(ikr\cos\theta)]. \tag{2.45}$$

Thereafter, the following identity needs to be used:

$$\exp(ir\cos\theta) = \sum_{n=0}^{\infty} i^n (2n+1) j_n(r) P_n(\cos\theta); \tag{2.46}$$

along with the fact that

$$\partial_\theta P_n(\cos\theta) = P_n^1(\cos\theta),\ \partial_\theta P_n(\cos\theta) = P_n^1(\cos\theta), \tag{2.47}$$

one can obtain the following equation for E_r^i:

$$E_r^i = -\frac{\cos\phi}{ikr} E^0 \sum_{n=0}^{\infty} i^n (2n+1) j_n(kr) P_n^1(\cos\theta). \tag{2.48}$$

It can be observed that E_r^i arises only from Φ and not Ψ. So, it is sensible to derive an expression for Φ from only Eq. 2.48. However, since $E_r^i = [\partial_r^2 + k^2](r\Phi^i)$ as given in one of Eqs. 2.43, a *r* needs to be included in Eq. 2.48 in the following way

$$E_r^i = \frac{i\cos\phi}{(kr)^2} E^0 \sum_{n=0}^{\infty} i^n (2n+1) S_n(kr) P_n^1(\cos\theta) \tag{2.49}$$

with

$$S_n(z) \equiv z j_n(z). \tag{2.50}$$

The set of functions that are obtained by multiplying the spherical Bessel functions with their argument are known as the Riccati-Bessel functions. In general, the Riccati-Bessel functions are defined as $F_n(z) \equiv z f_n(z)$ for all spherical Bessel functions $f_n(z)$. Further, it can be observed that the following identity holds true for $F_n(z)$ [16]:

$$\left[\partial_r^2 + k^2\right] F_n(kr) = \frac{n(n+1)}{r^2} F_n(kr), \tag{2.51}$$

and therefore, the following expansion for Φ^i can be obtained:

$$\Phi^i = \frac{i\cos\phi}{k} E^0 \sum_{n=1}^{\infty} i^n \frac{(2n+1)}{n(n+1)} j_n(kr) P_n^1(\cos\theta). \tag{2.52}$$

It can be seen that $\mathbf{H}^i$ has only one component that is in the $\hat{\mathbf{x}}_3$ direction. The following equation that is similar to Eq. 2.45 can be derived for the *r*-component of $\mathbf{H}^i$ by noticing that for the incident field given by $H_3^i = H^0 \exp(ikr\cos\theta)$, $H_r^i = H^0 \sin\theta \sin\phi \exp(ikr\cos\theta)$ can be re-structured to give:

$$H_r^i = -\frac{\sin\phi}{ikr} H^0 \partial_\theta [\exp(ikr\cos\theta)]. \tag{2.53}$$

Using Eqs. 2.11, H^0 can be related to E^0 by $H^0 = \frac{1}{\eta} E^0$. Here, $\eta \equiv \sqrt{\frac{\mu}{\varepsilon}}$ is a material property that is known as wave impedance.[1] An expression for Ψ^i can be derived using arguments that are similar to those used for Φ^i. Noting that $H_r^i = \frac{\tan\phi}{\eta} E_r^i$, the first equation in Eqs. 2.46 can be used to obtain the following equation for Ψ^i:

$$\Psi^i = -\sin\phi E^0 \sum_{n=1}^{\infty} i^n \frac{(2n+1)}{n(n+1)} j_n(kr) P_{n1}(\mu). \tag{2.54}$$

Eqs. 2.54 and 2.56 differ only slightly when the direction of polarization of $\mathbf{E}^i$ is changed from $\hat{\mathbf{x}}_2$ to $\hat{\mathbf{x}}_3$ since only the ϕ-dependence of E_r^i and H_r^i change. The summed terms remain the same for both, Φ^i and Ψ^i.

The fields inside the sphere can be constructed in a similar manner since modes with $m \neq 1$ cannot be excited by the given incident field. They can be expressed in the following way:

$$\begin{aligned} \Phi^p &= \frac{i\cos\phi}{k} E^0 \sum_{n=0}^{\infty} c_n j_n(kr) P_{n1}(\cos\theta), \\ \Psi^p &= -\sin\phi E^0 \sum_{n=0}^{\infty} d_n j_n(kr) P_{n1}(\cos\theta). \end{aligned} \tag{2.55}$$

---

[1] We have $\mu = \mu_0$ for materials of current interest as discussed in Sec. 1.1 of this chapter. So, one can set $\eta_0 = \sqrt{\frac{\mu_0}{\varepsilon_0}}$ and $\eta = \frac{1}{n}\eta_0$, where $\eta_0 \approx 120\pi\,\Omega \approx 377\,\Omega$ and *n* is the complex refractive indeed of a material defined by $n \equiv \sqrt{\varepsilon}$. ε denotes the relative permittivity of a material here. However, at some places in the document it denotes the actual permittivity (ε_0) depending on the context of the discussion. It may seem confusing at first, but the reader will be able to appreciate the utility of such a denotation as they read further through the document.

For the perturbed or scattered field, the outward propagating nature of the solutions can only be captured with spherical Hankel functions of the second kind that are defined as $h_n^{(2)} \equiv j_n - iy_n$, where y_n are the spherical Bessel functions of the second kind, since an outward propagating wave, for the current convention, should contain an $\exp(ikr)$ type term that can only come from the use of $h_n^{(2)}$. Hence, the scattered fields can be defined in the following manner:

$$\begin{aligned} \Phi^s &= \frac{i\cos\phi}{k} E^0 \sum_{n=0}^{\infty} a_n h_n^{(2)}(kr) P_{n1}(\cos\theta), \\ \Psi^s &= -\sin\phi E^0 \sum_{n=0}^{\infty} b_n h_n^{(2)}(kr) P_{n1}(\cos\theta). \end{aligned} \tag{2.56}$$

The boundary conditions can be applied to the tangential components of **E** and **H** at the spherical interface in the following way:

$$\begin{aligned} E_\theta^p &= E_\theta^i + E_\theta^s, \\ H_\theta^p &= H_\theta^i + H_\theta^s, \\ E_\phi^p &= E_\phi^i + E_\phi^s, \\ H_\phi^p &= H_\phi^i + H_\phi^s. \end{aligned} \tag{2.57}$$

The field components can be evaluated from Φ and Ψ. Calling the coefficients of the incident fields A_n; a_n, b_n, c_n and d_n can be evaluated to have the following values for a spherical particle with a relative permittivity ε^p. However, it becomes simpler to solve if one decouples the two scalar fields by observing that Eqs. 2.45 and 2.46 can be used with Eqs. 2.59 to give the following boundary conditions:

$$
\begin{aligned}
&\Psi^p = \Psi^i + \Psi^s, \\
&\varepsilon^p \Phi^p = \Phi^i + \Phi^s, \\
&\partial_r (r\,\Psi^p) = \partial_r (r\,\Psi^i) + \partial_r (r\,\Psi^s), \\
&\partial_r (r\,\Phi^p) = \partial_r (r\,\Phi^i) + \partial_r (r\,\Phi^s).
\end{aligned}
\tag{2.58}
$$

The coefficients fall into the following simultaneous equations for a sphere of radius *a* by noticing that $\frac{1}{k}\partial_{[kr]}[krj_n(kr)]$ is, essentially, $S_n'(kr)$.

$$
\begin{aligned}
&d_n j_n(k^p a) = j_n(ka) + b_n h_n^{(1)}(ka), \\
&\varepsilon^p c_n j_n(k^p a) = j_n(ka) + a_n h_n^{(1)}(ka), \\
&d_n S_n'(k^p a) = S_n'(ka) + b_n \xi_n'(ka), \\
&c_n S_n'(k^p a) = S_n'(ka) + a_n \xi_n'(ka).
\end{aligned}
\tag{2.59}
$$

These equations can be solved to give the following expressions for the coefficients:

$$
\begin{aligned}
a_n &= A_n \frac{S_n'(k^p a)\, j_n(ka) - \varepsilon^p j_n(k^p a) S_n'(ka)}{\varepsilon^p j_n(k^p a)\xi_n'(ka) - S_n'(k^p a) h_n^{(1)}(ka)}, \\
b_n &= A_n \frac{S_n'(k^p a)\, j_n(ka) - j_n(k^p a) S_n'(ka)}{j_n(k^p a)\xi_n'(ka) - S_n'(k^p a) h_n^{(1)}(ka)}, \\
c_n &= A_n \frac{j_n(ka)\xi_n'(ka) - h_n^{(1)}(ka) S_n'(ka)}{\varepsilon^p j_n(k^p a)\xi_n'(ka) - S_n'(k^p a) h_n^{(1)}(ka)}, \\
d_n &= A_n \frac{j_n(ka)\xi_n'(ka) - h_n^{(1)}(ka) S_n'(ka)}{j_n(k^p a)\xi_n'(ka) - S_n'(k^p a) h_n^{(1)}(ka)}.
\end{aligned}
\tag{2.60}
$$

As discussed in the literature, a recurrence algorithm can be constructed from the derivation to find a solution for the case of several concentric-spheres [3].

2.3 SOLUTION FOR A SPHERE IN THE LIMIT AS *KA* → *0*

Several problems of current interest involve situations in which the spheres of interest have radii that are significantly smaller than the length scale of the electromagnetic field disturbances k^{-1}—the inverse of the medium dependent wavenumber that appears in Helmholtz type equations. Essentially, it translates to $ka \to 0$ for a sphere of radius *a*. In such a situation, one can consider *a* as the representative length scale for the Maxwell equations. In the rescaled position variables, for the Helmholtz equation in one of the scalar potentials for **E** as given in Eq. 2.39, we have

$$[\nabla^{*2} + (ka)^2]\Phi = 0, \tag{2.61}$$

where, the superscript * denotes rescaled differentiation with respect to the variables $x_i^* \equiv x_i / a$. From now on we will not continue to use the superscript * for aesthetic reasons. It will be assumed that whenever the Laplace equation is used as an approximation for the Helmholtz wave equation, it is the *'d position variables. A situation may arise where a problem contains multiple length scales—several radii and/or several k^{-1}s. The maximum value of ka, $(ka)_{\max}$ should be made vanishingly small in order to have the Laplace equation approximation uniformly valid for the entire domain of the problem. Further, the rescaled position variable would be defined with respect to $a_{\max}$ rather than a.

In the limit as $ka \to 0$, the second term in the brackets of Eq. 2.61 would become vanishingly small, making the solution tend to that of a Laplace equation. One may want to resort to solving only the Laplace equations given by $\nabla^2\Phi = 0$ and $\nabla^2\Psi = 0$, followed by the substitution of their solutions in Eqs. 2.39 and 2.40 to evaluate **E** and **H**. In general, the limit

behavior of Φ which is a solution of the Helmholtz equation can be expressed as a series given by $\Phi = \sum_{n=0}^{\infty} (i\chi)^n \Phi_n$ such that $\nabla^2 \Phi_n = \Phi_{n-2},\ n \geq 0$ with $\Phi_n = 0$ for $n < 0$. The non-dimensional parameter χ is defined as $\chi \equiv ka$. Ψ can also be expanded in a similar manner. The far-field behavior of the solutions should coincide with the incident **E** and **H** fields given in Eqs. 2.8 and 2.11. In order to do that, on can analyze Eqs. 2.54 and 2.56 keeping in mind that *k* should be replaced with χ and that *r* is in radius *a* units. In the limit as $\chi \to 0$ such that $\chi r \to 0$ but $r \to \infty$ i.e., *r* is large but not large enough to make χr finite, the incident fields Φ^i and Ψ^i can be expressed in the following form:

$$F^i(\mathbf{r}) = \sum_{n=0}^{\infty} \sum_{m=-n}^{n} f_{nm} (\chi r)^n P_{nm}(\cos\theta) \exp(im\phi). \tag{2.62}$$

The radial dependence is of the form $(\chi r)^n$ rather than $j_n(\chi r)$ since, for small arguments, $j_n(z) \to \frac{z^n}{(2n+1)!!}$ [18]. The expression, essentially, represents the regular Laplace harmonics that allow one to begin with a leading order approximation of Φ to be given by just the regular harmonics that match with the coefficients given in Eq. 2.60. The coefficients f_{nm} can be evaluated from the incident field directly. Higher order terms are at least $O(\chi)$—allowing one to disregard them while evaluating the leading order contribution from the boundary. Eventually, if higher order corrections are required, they can be evaluated by solving $\nabla^2 \Phi_n = \Phi_{n-2},\ n \geq 0$ successively for all values of *n*. In the case of *n* =1 as for the $O(\chi)$ term, only the regular Laplace harmonics are necessary to express the far-field; however, such terms needs to match with higher order terms of the applied field's expansion. It can be observed in Eqs. 2.54 and 2.56

that if the $O(\chi)$ term is to be considered, it needs to match the incident field's magnetic dominant component Ψ^i. Essentially, $\Phi = \sum_{n=0}^{\infty} (i\chi)^{2n} \Phi_{2n}$ and $\Psi = \sum_{n=0}^{\infty} (i\chi)^{2n+1} \Psi_{2n}$ so that $\nabla^2 \Phi_n = \Phi_{n-2},\ n \geq 0$ and $\nabla^2 \Psi_n = \Psi_{n-2},\ n \geq 0$. The next significant correction is the second term in the Φ series that is of $O(\chi^2)$. It needs to be matched with next higher order term in the expansion of $j_n(\chi r)$, that has a z^{n+2} dependence, of the incident electric field's electric component Φ^i. Albeit, this cannot be known for a fact unless the algebra is worked out—it may very well be that the $O(\chi^2)$ term may correspond to several other higher order terms in the expansion of Φ^i. At this stage, the interest is only in the $O(\chi)$ effects. It may suffice to say that the evaluation of higher Φ and Ψ terms will require the solution of the eigenvalue problem given by the modified Helmholtz equations for $F = \Phi, \Psi$ given by $[\nabla^2 - \varsigma^2]F = 0$—the solution of which can serve as an orthogonal basis for the solution of the Poisson equations for Φ and Ψ. Clearly, the solution of the modified Helmholtz equation for this case are known and are given in the previous section. They only need to be slightly adjusted to suit the particularities. The next task is to expand the inhomogeneous term in this basis, followed by term by term matching and evaluation of the required new coefficients. The task will amount to representing regular Laplace harmonics in terms of the Helmholtz basis that may or may not permit analytically evaluatable integrals.

The solutions, for the case of one sphere and a layered sphere can be derived either by studying the limiting behavior of the solutions given in the previous section or by solving the differential equations subject to the boundary conditions in asymptotic limit of $\chi \to 0$. This would, eventually, amount to the analysis of the coefficients given Eqs. 2.62 in the limit. Such a

"shortcut" can be justified based on the consideration of the symmetry within the operations required to solve the problem in and not in the limit. All the coefficients given in Eqs. 2.62 can be evaluated in the limit as $ka \to 0$, and effectively, $k^p a \to 0$ to give the asymptotic behavior of each a_n, b_n, c_n and d_n. The small argument behavior of $y_n(z)$ is given by $\frac{-(2n-1)!!}{z^{n+1}}$ [18]. The small argument behaviors of $S_n(z)$ and $h_n^{(2)}(z)$ are consequently given by $\frac{z^{n+1}}{(2n+1)!!}$ and $\frac{z^n}{(2n+1)!!} - i\frac{(2n-1)!!}{z^{n+1}}$ respectively. The small argument behaviors of the coefficients can be evaluated using the behaviors of the involved Bessel functions. Since one would expect that the higher order terms would have higher order dependence of χ, it may be sensible to analyze only the *n*=1 coefficients' asymptotic behavior. It can be found that the most significant dependence of the coefficients on ka and ε^p are given by:

$$
\begin{aligned}
a_1 &\to -\left[\frac{\varepsilon^p - 1}{\varepsilon^p + 2}\right](ka)^3, \\
b_1 &\to 0, \\
c_1 &\to i\frac{9}{2}\frac{1}{\sqrt{\varepsilon^p}(\varepsilon^p + 2)}, \\
d_1 &\to i\frac{3}{2}\frac{1}{\sqrt{\varepsilon^p}}.
\end{aligned}
\tag{2.63}
$$

It may be tempting to think that when the material permittivity ε^p is made to tend to zero, internal field coefficients c_1 and d_1 blow up. It is, in fact, not true because the behavior for vanishingly small values of ε^p needs to be analyzed by incorporating it from beginning of the analysis. It can be clearly seen that the leading order size dependence of the scattered field is

through a_1 . As a consequence, it seems that one can work with relatively large values of *ka*—upto ~0.46 in order to have a $(ka)^3$ that is ~0.1 and the next higher term is ~0.02. The *ka* that matters does not incorporate the permittivity of the sphere; rather, just the wavenumber in the medium along with the radius of the sphere. Any effect that may arise due to singular behavior in the term in the square bracket in the first expression in 2.65 is in addition to the "size effect" which may seem to operate independent of the "material effect". They, however, are coupled and it may very well be possible that under certain special circumstances, a higher order terms becomes significant due only to the "material effect". In general, though, the size effect would always try to reduce the influence of the higher order terms for *ka* values that are less that ~0.5.

It may be safe to guess that in the presence of several other spheres that are small enough with respect to some relevant problem specific length scale, it would be sensible to analyze the problem of evaluating the electromagnetic fields for such a domain with the consideration of only the leading order effects, i.e., only solve the corresponding Laplace problem for the electric generating field Φ. However, the procedure for constructing the solution of the full wave equation under the perturbation is somewhat different than the refinement discussed above. The full details of the construction procedure will be discussed in the relevant chapter. Here, only certain significant details will be discussed. The solutions of the Laplace field that are obtained using the numerical method discussed in the following section will correspond to Φ_0 in the perturbation series given by $\Phi = \sum_{n=0}^{\infty} (i\chi)^{2n} \Phi_{2n}$. The Helmholtz harmonics for the scalar fields permit non-wave-like *r*-dependent solutions $j_n(\chi r)$ and $y_n(\chi r)$ that can be replaced with

Laplace like terms $\frac{\chi^n r^n}{(2n+1)!!}$ and $\frac{(2n-1)!!}{\chi^{n+1} r^{n+1}}$ respectively while moving from the Helmholtz to the Laplace approximation. Similarly, Henkel functions $h_n^{(1)}(\chi r)$ are replaced by $\frac{\chi^n r^n}{(2n+1)!!} - i\frac{(2n-1)!!}{\chi^{n+1} r^{n+1}}$ which, for small arguments, are just $\frac{-i(2n-1)!!}{\chi^{n+1} r^{n+1}}$. Clearly, "going back" to Helmholtz from Laplace would require that the less significant term corresponding to the Hankel function be added so that the wave behavior can be incorporated into the non-wave-like solution. As an example, consider the a regular solution set for the Laplace problem given by $\Phi_{nm}^p = R_{nm} r^n P_n^1(\mu) e^{im\phi}$. Since it is supposed to correspond to $\Phi_{nm}^p = C_{nm} j_n(\chi r) P_n^m(\mu) e^{im\phi}$, it can be seen that $C_{nm} = \frac{(2n+1)!!}{\chi^n} R_{nm}$. Similarly, the corresponding scattered field coefficients A_{nm} are related to the singular Laplace coefficients S_{nm} by $A_{nm} = \frac{i\chi^{n+1}}{(2n-1)!!} S_{nm}$. **E** and **H** can be constructed, thereafter, using Eqs. 2.40 and 2.41. In a situation where only the leading order Φ behavior is to be studied, the expressions can analyzed by substituting the expression for Φ_0. Following the previously discussed argument about Ψ_0 being $O(\chi)$, it is safe to disregard it, at least in the beginning of the analysis. The double curl term for **E** can be simplified in the following way:

$$\nabla \times \nabla \times (\mathbf{r}\Phi) = -\nabla^2(\mathbf{r}\Phi) + \nabla[\nabla \cdot (\mathbf{r}\Phi)] = [-\partial_i - r_i \partial_j \partial_j + 2\partial_i + r_j \partial_j \partial_i]\Phi = \chi^2 \mathbf{r}\Phi + (1 + \mathbf{r} \cdot \nabla)\nabla\Phi.$$

The first term can be disregarded since, in the near-field, at least, it is multiplied by two small numbers, χ and χr. The second term, in either situation, near or far-field, is an $O(1)$ constant times $\nabla\Phi$ which can be easily evaluated for, both, singular and regular Laplace harmonics. The singular and regular Laplace harmonics, respectively, simplify to the following expressions:

$$\mathbf{E} = -\sum_{n,m} n\nabla\Phi^{S}_{nm} \tag{2.64a}$$

and

$$\mathbf{E} = \sum_{n,m} (n+1)\nabla\Phi^{R}_{nm}. \tag{2.64b}$$

The magnetic field **H** corresponding to Φ_0 doesn't really simplify to such an expression, however, it does for Ψ_0. The expression for **H** can be expressed in the following way:

$$\mathbf{H} = \frac{-i\chi}{\eta}\nabla\times(\mathbf{r}\Phi) + \frac{1}{i\eta\chi}[\chi^2\mathbf{r}\Psi + (1+\mathbf{r}\cdot\nabla)\nabla\Psi]. \tag{2.65}$$

Clearly, because the last term in the square brackets is $O(\chi)$, it has an $O(\eta^{-1})$ effect—a material effect that is independent of the wavenumber χ. Hence, the leading order effect of Ψ_0 for **H** is $O(1)$ permitting expressions similar to Eqs. 2.64. They are:

$$\mathbf{H} = \frac{-1}{i\eta\chi}\sum_{n,m} n\nabla\Psi^{S}_{nm} \tag{2.66b}$$

and

$$\mathbf{H} = \frac{1}{i\eta\chi}\sum_{n,m} (n+1)\nabla\Psi^{R}_{nm}. \tag{2.66b}$$

2.4 SOLUTIONS FOR SEVERAL SPHERES IN THE LIMIT AS $KA \rightarrow 0$

In the situation that several spheres comprise a domain in which the fields are to be evaluated, an analytical solution would not seem likely based on the fact that it is not possible to represent the field in such a domain with a unique set of orthogonal functions whole amplitudes need to be evaluated using the boundary conditions. Although, it clearly is possible to represent a given field in terms of the spherical Laplace harmonics about any point in the domain; be it the centre of the spheres, because there is a contribution that comes in from the interaction through the other spheres, the coefficients of the representation about the points of choice within the domain cannot be explicitly evaluated from the known incident or applied fields. An implicit evaluation of the harmonics amplitudes can be performed simply by solving a matrix equation for the form $\overline{\mathbf{A}}\mathbf{x} = \mathbf{b}$ because of linearity. The vector **x** would contain unknown harmonics amplitudes, **b** would contain the known applied field harmonics amplitudes and the matrix $\overline{\mathbf{A}}$ contains the information regarding the problem domain in terms of the linear coefficients of the simultaneous equations that connect the amplitudes. In general, for a Laplace field subject to some far-field boundary condition, the scheme, given below, can be used to evaluate the multipole coefficients corresponding to each sphere.

The regular harmonics for the field inside the γ^{th} sphere can be expressed as:

$$\Phi_{nm}^{R\gamma}(\mathbf{r}) = R_{nm}^{\gamma} r^{n} P_{nm}(\mu) e^{im\phi}, \tag{2.67}$$

and the singular harmonics are:

$$\Phi_{nm}^{S\gamma}(\mathbf{r}) = S_{nm}^{\gamma} r^{-n-1} P_{nm}(\mu) e^{im\phi}. \tag{2.68}$$

Here, the position vector **r** is defined from the center of the γ^{th} sphere and is given by $\mathbf{r} \equiv \mathbf{R} - \mathbf{r}^{\gamma}$, where **R** denotes the position vector with respect to some origin and $\mathbf{r}^{\gamma}$ denotes the position vector pointing toward the center of the sphere with respect to the same origin. Similarly, $\mu \equiv \cos\theta$ and ϕ are defined based on the angular displacements of **r** rather than any other position vector. For monodisperse spheres, one can work in non-dimensional units that were discussed before—it, essentially, amounts to setting the radius of the spheres equal to one. In the case of polydisperse spheres, a specific sphere radius, either some kind of average, largest or smallest, can be chosen to be the length scale with respect to which all lengths are normalized. The only place where the dispersity will figure in is in the expressions for the boundary conditions about the spheres where the values of the radii become important. In general, the sphere boundary conditions will form a set of $2N_pN(2N+1)$ simultaneous linear equations, where the factor 2 accounts for the two boundary conditions that are required for second order differential equations, N_p is the number of spheres in the domain and N is the global maximum number of multipoles that are used in the calculation. Since the multipole degrees *m* can have $(2N+1)$ values, a factor of $(2N+1)$ is also incorporated. On the surface of a sphere (*r* =1), depending on physics of the problem, i.e., whether it is the electromagnetic scalar field or a thermal field, different conditions need to be applied. Both conditions will be discussed here so that they can be related eventually to demonstrate the possibility of a one to one mapping among the resulting solutions. The continuity of scalar field boundary condition for a thermal field is given by:

$$R_{nm}^{\gamma} = \{a^{\gamma}\}^{-2n-1} S_{nm}^{\gamma} + F_{nm}^{\gamma} + \sum_{\delta,\delta\neq\gamma} R_{nm}^{\gamma\delta}, \tag{2.69}$$

where, F_{nm}^{γ} represents the applied or incident far-field expanded about center of the γ^{th} sphere and the last terms $R_{nm}^{\gamma\delta}$ represent the regular contributions of the singularities present at other spheres that are labeled δ such that $\delta \neq \gamma$. To account for the presence of polydispersity, the factor of $\{a^{\gamma}\}^{-2n-1}$ is incorporated. a^{γ} Represents the dimensionless radius of the γ^{th} sphere based on some length scale associated with the polydispersity as was discussed before in this section. The electromagnetic scalar field Φ is not continuous and is given by the second equation in Eqs. 2.60. As a result, the conditions for the coefficients can be translated to the following equations:

$$\varepsilon^{\gamma} R_{nm}^{\gamma} = \{a^{\gamma}\}^{-2n-1} S_{nm}^{\gamma} + F_{nm}^{\gamma} + \sum_{\delta,\delta\neq\gamma} R_{nm}^{\gamma\delta}, \tag{2.70}$$

where the electric permittivity of the sphere under consideration is ε^{γ} relative to the embedding medium. The continuity of thermal flux results in the following set of equations

$$\alpha^{\gamma} n R_{nm}^{\gamma} = -\{a^{\gamma}\}^{-2n-1}(n+1) S_{nm}^{\gamma} + n F_{nm}^{\gamma} + n \sum_{\delta,\delta\neq\gamma} R_{nm}^{\gamma\delta}, \tag{2.71}$$

and the continuity of tangential **E** and **H** results in the fourth condition given in Eqs. 2.60

$$(n+1) R_{nm}^{\gamma} = -\{a^{\gamma}\}^{-2n-1} n S_{nm}^{\gamma} + (n+1) F_{nm}^{\gamma} + (n+1) \sum_{\delta,\delta\neq\gamma} R_{nm}^{\gamma\delta}. \tag{2.72}$$

The re-expansion terms recur in all the boundary condition equations. Depending on the problem, the re-expansion term can be evaluated based the choice of representation of the ϕ-dependent term in the Laplace harmonics. For real valued functions, it makes sense to not use $e^{im\phi}$, but rather, two separate harmonics containing either $\sin m\phi$ or $\cos m\phi$. Such would be the

case for dealing with thermal or time-stable fluid fields; where it is traditional to deal only with real quantities. However, in the literature related to electromagnetics and other field theories that build on it, such as quantum mechanics and quantum field theories, it is customary to use the complex representation—primarily to aid the incorporation of complex phase information into the amplitude of the wave type solutions. On may rationalize further by considering the fact that most thermal or time-stable fluid fields—unless there is an oscillatory flow—permit non-wavelike solutions most of the time. In the case of oscillatory flows and the study of stability of non-linear and/or time-unstable flows, time harmonic complex term such as $e^{i\omega t}$ are typically included to account for oscillations in time—making mode amplitudes complex quantities. Wave solution permitting differential equations have solutions that have an oscillatory nature, both, in space and time coordinates. So, the same phase can result in a change in either the space or time coordinate. In spherical harmonics that represent outgoing or incoming waves for a time harmonic solution, complex Hankel functions, that allow wavelike behavior, are used to represent the radial dependence. The, θ-dependent, associated Legendre polynomials in $\cos\theta$ do not span a complete space—disallowing them to sustain a wave solution that can travel in space and time. Hence, there is always a standing wave in θ. In ϕ, however, a full circle is spanned. So, a travelling wave can be permitted. One can think of such a wave as circulating ripples on a closed loop of an elastic string. In dealing with the current problem, for the purpose of this work, the complex notations would be preferred even though they will, at some point, seem to complicate the algebra related to the re-expansion of the singular harmonics.

Given a singular harmonic located at $\mathbf{r}^{\gamma}$, $\Phi_{nm}^{S\gamma}(\mathbf{r}_{\gamma}) = S_{nm}^{\gamma} r_{\gamma}^{-n-1} P_{nm}(\mu_{\gamma}) e^{im\phi_{\gamma}}$, we wish to represent it with regular harmonics located at another point $\mathbf{r}^{\delta}$, $\Phi_{kl}^{R\delta}(\mathbf{r}_{\delta}) = R_{kl}^{\delta} r_{\delta}^{k} P_{kl}(\mu_{\delta}) e^{il\phi_{\delta}}$. The subscripted position vector represents the position vector emanating from the centre of the

sphere. Clearly, it can be expected that in a linear system, $R_{kl}^{\delta} = \sum_{n}\sum_{m} T_{nm}(\mathbf{r}_{\delta} - \mathbf{r}_{\gamma} \mid k,l) S_{nm}^{\gamma}$. The coefficients need to be evaluated with the aid of certain algebraic properties of the harmonics [19, 20]. For the purpose of this work, the coefficients are not derived. The coefficients used by Mo and Sangani [20], although relatively more straightforward, need to be modified in order to accommodate the complex ϕ term in the harmonics and the resulting negative values of the degree *m*. The modification, effectively, amounts to the results of the analysis presented by Epton and Dembart—they look less complicated and easier to approach [19]. The re-expansion coefficients are given below:

$$T_{nm}(\mathbf{r} \mid k,l) = \tau_{nmkl} r^{-(n+k+1)} P_{n+k,m-l}(\mu) e^{i(m-l)\phi}, \tag{2.73}$$

where

$$\tau_{nmkl} = \frac{(-1)^n i^{|m-l|-|l|-|m|} \varepsilon_{m-l} \varepsilon_l}{\varepsilon_m} \frac{(n+k-m+l)!}{(n-m)!(k+l)!} \tag{2.74}$$

and

$$\varepsilon_m \equiv \begin{cases} (-1)^m & if \;\; m \geq 0, \\ 1 & if \;\; m < 0. \end{cases} \tag{2.75}$$

The associated Legendre polynomials, that are used here, are usually denoted by P_n^m rather than P_{nm}, i.e., $P_{nm}(x) = P_n^m(x) \equiv \frac{1}{2^n n!} \frac{(n+m)!}{(n-m)!} (1-x^2)^{-m/2} \frac{d^{n-m}}{dx^{n-m}} (x^2-1)^n$ with $-n \leq m \leq n$ [19]. Such a definition accommodates negative *m* values.

Laplace harmonics are scale independent, allowing them to be translated or re-expanded at any distance far away from a given singularity. Of course, there are certain mathematical constraints related to the quality of convergence of the re-expansion such as the distance between the two points and the related angles so that non-convergence can be avoided. A convergence may be induced in case of a slowly converging sequence however. Helmholtz harmonics, as one would expect, have a dependence on not just the length scale of the particles, but also the inverse wavenumber χ^{-1}, making it necessary to incorporate a phase factor given by $e^{i\chi r}$ when re-expanding a Helmholtz harmonic as a Laplace harmonic in the far-field—in which case, only the $n = 1$ harmonic would remain significant and the phase factor would only affect its amplitude—essentially, one would just be re-expanding a dipole into several near-field multipoles at the far-field point. In the inner region, defined by $\chi r \to 0$, the exponential would not matter and all re-expansions with Laplace harmonics would remain valid. However, in the intermediate region, a re-expansion using Laplace approximation will not remain valid; even in the case where the re-expansion is in the near-field, since, the Helmholtz harmonics behave significantly differently. It may be possible to work out such an expansion and other combinations involving near, intermediate and far fields, but, our current discussion will be restricted to near to far, far to near, near to near and far to far re-expansions that, essentially, correspond to a combination of either $\chi r \to 0$ or $\chi r \to \infty$ in the context of some origin. Full-wave potentials are needed to treat the intermediate region, even for a vanishingly small χ because of the arguments in Bessel functions that depend on χr. The intermediate region can be though to begin after r becomes $O(1)$. Re-expansions involving vector Helmholtz harmonics require different operations due to the dependence on both displacement and orientation [19]. In case only scalar Helmholtz

harmonics are being used, the algebraic operations that can generate the harmonics form the Green's function is are different than those needed for the Laplace equation [21].

A slight change needs to be made to the coefficient in Eq. 2.73 in order to incorporate the fact that the quantity that is being re-expanded behaves differently than the actual physical quantity whose effect one is interested in determining at a point that is far away from a given singularity. Because the regular harmonics generate a field that is different from that generated by singular harmonics, the field-re-expansion coefficients differ from T_{nm}. For a singular harmonic given by Φ^{γ}_{nm} that is located at a point γ, the corresponding "electric field multipole" would be $-n\nabla\Phi^{S\gamma}_{nm}$ which needs to be re-expanded to regular field multipole at a point δ given by $(k+1)\nabla\Phi^{R\delta}_{kl}$ as discussed in Eqs. 2.66 in the previous subsection. Clearly, then, T_{nm} need to be modified to $\mathrm{T}_{nm} = -\dfrac{n}{k+1}T_{nm}.$ The coefficients remain valid for the modified magnetic field given by $i\eta\chi\mathbf{H}$ as can be gleaned from Eqs. 2.68.

The singular and regular coefficients can be evaluated by solving the matrix equations given in Eqs. 2.72 and 2.74. For the purpose of numerical evaluation, here, the regular coefficients were eliminated to give a single equation in S^{γ}_{nm} that can be structured as a 1-D matrix or higher dimensional matrix depending on the programming requirements. The equation in S^{γ}_{nm} is:

$$\frac{(n\varepsilon^{\gamma}+n+1)}{(n+1)}\{a^{\gamma}\}^{-2n-1}S^{\gamma}_{nm}-(\varepsilon^{\gamma}-1)\sum_{\delta,\delta\neq\gamma}R^{\gamma\delta}_{nm}=(\varepsilon^{\gamma}-1)F^{\gamma}_{nm}. \tag{2.76}$$

The $(\varepsilon^{\gamma}-1)$ term is kept as it is to avoid division by zero in case a sphere has a relative permittivity equal to one. The second term on the left of the equal sign is also a linear operation on $\mathcal{S}_{kl}^{\delta}$. All operations on the left side can be lumped into a matrix denoted by $\mathrm{M}_{nmkl}^{\gamma\delta}$ that operates on $\mathcal{S}_{kl}^{\delta}$. The vector on the right side of Eq. 2.76 contains information about the applied or incident field. The unknown coefficients can be obtained by, simply, solving the matrix equation. For the most part of this work, this has been accomplished using the MATLAB environment [22] —which, essentially, amounts to choosing the best possible method for solution based on the type of the matrix. The matrix $\mathrm{M}_{nmkl}^{\gamma\delta}$, in case $\mathcal{S}_{kl}^{\delta}$ is arranged as a vector, is a non-singular and full-matrix in general—it does not expected to contain zeros. A problem specific condition may give rise to some elements within it to assume values that render the matrix ill-conditioned and, possibly, sparse—a situation in which one would be required to use a matrix regularization method such as the Tikhonov regularization in which problem of minimizing the residual is redefined [23].

The scalar field corresponding to the magnetic field will also fall into a similar algebraic structure as that for the electric scalar field. However, it is immediately clear that in non-magnetic media, the permeability of all the media are the same—implying that, in Eq. 2.76, the vector $\mathcal{S}_{kl}^{\delta}$ is identically zero. Since this is a leading order effect for **H** due to the Ψ field, it may make sense to ask about the contribution due to the next higher order term in Eq. 2.65. Since the term is symmetric for regular and singular harmonics, it will also be affected by the same issue that the media are non-magnetic. Hence, the only magnetic field contribution, to the leading order in χ, is due to the Φ field. The regular magnetic multipoles are not zero however. They are simply equal to those corresponding to the applied field.

An interesting concluding observation can be made regarding the fact that the solution to the thermal field problem that is given by:

$$-\frac{(n\alpha^{\gamma}+n+1)}{n}\{a^{\gamma}\}^{-2n-1}S_{nm}^{\gamma}-(\alpha^{\gamma}-1)\sum_{\delta,\delta\neq\gamma}R_{nm}^{\gamma\delta}=(\alpha^{\gamma}-1)F_{nm}^{\gamma}, \tag{2.77}$$

can be adjusted to solve Eq. 2.76 for a given value of F_{nm}^{γ} and setting $\alpha^{\gamma}=\varepsilon^{\gamma}$. Let such a constant be C_{nm} such that $C_{nm}S_{nm}^{\gamma}$ solves Eq. 2.76. Substitution in Eq. 2.77 followed by equation of the left sides of Eqs. 2.76 and 2.77 yields the following relation for the constants:

$$\begin{aligned}&-\frac{(n\varepsilon^{\gamma}+n+1)}{n}\{a^{\gamma}\}^{-2n-1}S_{nm}^{\gamma}-(\varepsilon^{\gamma}-1)\sum_{\delta,\delta\neq\gamma}R_{nm}^{\delta}\\&=\frac{(n\varepsilon^{\gamma}+n+1)}{(n+1)}\{a^{\gamma}\}^{-2n-1}C_{nm}S_{nm}^{\gamma}-(\varepsilon^{\gamma}-1)\sum_{\delta,\delta\neq\gamma}R_{nm}^{\delta}.\end{aligned} \tag{2.78}$$

From Eqs. 2.69, 2.71 and 2.70, 2.72, it can be found that the expressions for R_{nm}^{γ} are identical for the thermal and electromagnetic case—implying that the regular harmonic amplitudes are all equal for the two problems. Clearly, the constants C_{nm} have to have the following values:

$C_{nm}=-\frac{n+1}{n}$. The two problems are the same except for a constant factor.

3 OPTICAL CONSTANTS OF MATERIALS

3.1 INTRODUCTION

The responses of materials to electromagnetic field are typically linear unless laser or other forms of relatively intense sources are used. Only linear properties of isotropic and homogenous materials are of interest here. Their electromagnetic constitutive relationships are defined separately for electric and magnetic fields since the fields only become coupled at non-zero frequencies. Under the influence of a constant electric field, the following constitutive relation is valid:

$$\mathbf{D} = \varepsilon \mathbf{E}. \tag{3.1}$$

D is known as electric displacement, a consequence of polarization of a material under the influence of an applied electric field **E**. ε is the electric permittivity of a material. It represents the propensity of a material to become polarized under the effect of an applied field. Because of the way the units are chosen and due to the fact that a vacuum should have a zero polarization, **D** is further related to a quantity called polarization **P** through

$$\mathbf{D} = \varepsilon_0 \mathbf{E} + \mathbf{P} \tag{3.2}$$

where, ε_0 is a universal quantity representing the permittivity of vacuum. Because this quantity is non-zero, the polarization is accounted for separately. **P** depends linearly on the applied field as

$$\mathbf{P} = \chi \varepsilon_0 \mathbf{E}. \tag{3.3}$$

Here, χ is known as electric susceptibility. It is zero for vacuum.

The magnetic field is a dual of the electric field, and so, it's interaction with a materials have a similar set of constitutive relationships. The magnetic induction field **B** is related to an applied magnetic field **H** as

$$\mathbf{B} = \mu \mathbf{H}. \tag{3.4}$$

In this work, the materials under consideration do not have a significant magnetic response to an applied field at optical frequency. Consequently, we don't have to worry about the magnetization response of materials. We can set the magnetic permittivity to be that of vacuum.

$$\mu = \mu_0. \tag{3.5}$$

The relations are defined for situations where the applied fields are constant and the polarization response of the material has achieved a steady state. While for the magnetic field, the linear response is related to the applied field through a universal material independent constant, in the case of the electric field the following convolution relationship is required to relate the polarization, susceptibility and the applied field. In case of a linear medium, it is

$$\mathbf{P}(t) = \varepsilon_0 \int_{-\infty}^{t} \chi(t-\tau)\,\mathbf{E}(\tau) d\tau. \tag{3.7}$$

Fourier transformation of the equations given above with the aid of the convolution theorem leads to

$$\mathbf{P}(\omega) = \varepsilon_0 \chi(\omega)\mathbf{E}(\omega), \tag{3.7}$$

and

$$\mathbf{D}(\omega) = \varepsilon(\omega)\mathbf{E}(\omega) \tag{3.8}$$

or, simply,

$$\mathbf{D} = \varepsilon\mathbf{E} \text{ with } , \varepsilon = \varepsilon_0[\chi(\omega)+1]. \tag{3.9}$$

The expression ties in with time harmonic Maxwell equations discussed in Chap. 2 to give the following equations under no free charge and current conditions in a homogenous medium:

$$(\nabla^2 + k^2)\mathbf{E} = \mathbf{0}. \tag{3.10}$$

Here, $k^2 \equiv \omega^2\mu\varepsilon$. As a result, the propagation of light in a medium depends on its permittivity. At optical frequencies, it is impossible to disregard the wave nature of the fields. A material's optical properties are usually measured by probing a material with light waves of different wavelengths. Reflection or transmission of the probe light is usually measured and the material properties are indirectly inferred from that information. The Fourier transformed permittivity is typically measured as a function of the frequency or wavelength of the incident light.

A material can be seen as a collection of charged particles from the perspective of electromagnetics. The way those charges interact with one other decide the state, phase and, as a consequence, its electromagnetic response. Outside of the nucleus, the only force field that holds a material together is electromagnetic in nature. The mechanical response of a charge under an electromagnetic field is governed by the Lorentz force given by

$$\mathbf{F} = q[\mathbf{E} + \mathbf{v} \times \mathbf{B}]. \tag{3.11}$$

The magnetic field affects a moving charge through a normal force. In Eq. 3.11, **v** is the velocity of the charge under consideration. The relative strengths of the forces induced by the coupled fields **E** and **B** can be analyzed. The length scale for waves in homogenous material is inverse wavenumber k^{-1}. So, the effect of a $\nabla\times$ is $O(k^{-1})$. Since, $\nabla \times \mathbf{H} = -i\omega\varepsilon\,\mathbf{E}(\omega)$, it can be said that $\frac{H}{E}$ is $O(\eta)$ such that $\eta = \sqrt{\frac{\varepsilon}{\mu}}$. Consequently, $\frac{B}{E}$ has a magnitude of the order of $\mu\eta = \sqrt{\mu\varepsilon}$ —the speed of light in that medium. Hence, unless charges in a medium move at relativistic speeds, the magnetic force is much smaller in comparison to the electric force for an applied electromagnetic wave.

3.2 PERMITTIVITY MODELS

The electric response of several materials can be modeled using relatively simple models that are based only on the averaged behavior of electrons within the material. The way in which the electrons are bound would result in the type of balancing forces they would experience while under the influence of an applied field. In general, for an electron, a classical, linearized force balance equation is be given by

$$m\ddot{\mathbf{x}} + \beta\dot{\mathbf{x}} + \eta\mathbf{x} = -e\mathbf{E}. \tag{3.12}$$

Here, m is the mass of an electron, β is the averaged drag to the motion created by the collisions within the material, η is a spring constant for the restoring forces with the material and e is the magnitude of an electron's charge.

Depending on the type of distribution of charge within a specific type of material, which could either have all electrons bound to nuclei through spring like forces or could contain electrons that are rather free to delocalize over the entire span of the material, the $\eta\mathbf{x}$ term has to be excluded in Eq. 3.12.. In the case of a conducting material—a material that can permit electron delocalization—the dissipation term comes about because of the classical collisions among electrons and the lattice. In the case of materials that have bound electrons, dissipation may arise due to a coupling between lattice vibration modes and the vibrating electron-nucleus system.

3.2.1 Metals

One can set $\eta = 0$ for metals. The dielectric response of a material depends on how its electrons and ions respond to a time-varying applied electric field. Metals, at ordinary

temperatures and applied electric fields, can be thought of as a plasma made of an ordered crystal of positive ions and a fluid made of electrons. In a very simple approximation, one can see the electrons to resemble a gas wherein the inter-electron interactions are negligible. The ion lattice can be assumed to vibrate due to a finite temperature and impede the motion of electrons through collisions—leading to a finite conductivity.

Let the number density of electrons in a gas be *n*, mass of an electron *m*, charge of an electron *e* and gas velocity **u**. The gas can be thought of as an incompressible, slow-moving, irrotational and invicid fluid in one dimension. It follows the following equation under the influence of an applied electric field **E**(t).

$$\rho \frac{d\mathbf{v}}{dt} + \gamma \mathbf{v} = \mathbf{f}, \rho = nm \ \& \mathbf{f} = -ne\mathbf{E}. \tag{3.13}$$

The constant γ represents dissipation due to collisions with the ion lattice. Fourier transformation leads to $\mathbf{v}(\omega)(-i\omega\rho + \gamma) = -ne\mathbf{E}(\omega)$. Since the current density is defined as $\mathbf{J}(\omega) \equiv -ne\mathbf{v}(\omega)$, it can be seen that $-ne\mathbf{v}(\omega) = \frac{n^2e^2}{(\gamma - i\omega\rho)}\mathbf{E}(\omega)$. Further, since $\mathbf{J}(\omega) = \sigma(\omega)\mathbf{E}(\omega),$ it can be shown that the Fourier transformed conductivity $\sigma(\omega)$ is

$$\sigma(\omega) = \frac{n^2e^2}{(\gamma - i\omega\rho)}. \tag{3.14}$$

The conductivity is complex valued with negative real part and positive imaginary part. In order to incorporate it into the permittivity, one can assume the current to be a free current for the vacuum that contains the material. Then, using Maxwell curl equation, it can be observed that $\nabla \times \mathbf{H}(\omega) = -i\omega\varepsilon_0 \mathbf{E}(\omega) + \sigma(\omega)\mathbf{E}(\omega).$ The general complex relative permittivity can be defined

from here as $\varepsilon(\omega) = 1 - \frac{\sigma(\omega)}{i\omega\varepsilon_0}$. A substitution of Eq. 3.14 leads to the following equation:

$\varepsilon(\omega) = 1 - \frac{n^2 e^2}{i\omega\varepsilon_0(\gamma - i\omega\rho)}$. Renaming, γ / ρ as the collision frequency ω_C and $n^2e^2 \big/ \varepsilon_0\rho$ the square of a plasma frequency ω_P,

$$\varepsilon(\omega) = 1 - \frac{\omega_P^2}{(\omega^2 + i\omega\omega_C)}. \tag{3.15}$$

The permittivity is also complex valued with a negative real part and a positive imaginary part for intermediate values of frequencies. The model is generally referred to as the Drude model. It is known to fit the experimental data for high conductivity metals such as silver and aluminum very well.

3.2.2 Insulators

Materials that cannot sustain an electric current within them are known as insulators. This, typically, implies the presence of 'bound' electrons that cannot participate in the formation of a current. At low temperatures, the force balance equation for one electron-nucleus pair can be generalized to represent the bulk. This, of course, can be done under the assumption that the electron's thermal energy and correlation length scales are, both, very small compared to the electrostatics-induced kinetic energy due to the displacement and mean inter-nuclear distance and electron's mean free path. These assumptions can, in principle, be valid for solids whose electrons are very strongly correlated to their nuclei that lead to a negligible cross-atom interaction. The electron 'fluid' can now be seen to follow the following equation.

$$\rho\frac{\partial \mathbf{v}}{\partial t}+\gamma\mathbf{v}+\kappa\mathbf{x}=\mathbf{f},\ \mathbf{x}=\int_0^t \mathbf{v}d\tau,\ \rho=nm,\ \mathbf{f}=-ne\mathbf{E} \tag{3.16}$$

However, the absence of a current can be accounted for by re-writing the equation in terms of the displacement **x**. Eventually, the polarization of the material can be seen as arising from local dipoles that are created due a non-zero **x**. Fourier transforming the force balance equation leads to $\mathbf{x}(\omega)(\omega^2\rho-i\omega\gamma+\kappa)=-ne\mathbf{E}(\omega)$. Since $\mathbf{P}(\omega)\equiv ne\mathbf{x}(\omega)$ and $\mathbf{P}(\omega)=\varepsilon_0\chi(\omega)\mathbf{E}(\omega)$, it can be shown that $\varepsilon_0\chi\mathbf{E}=-\dfrac{n^2e^2}{(\omega^2\rho-i\omega\gamma+\kappa)}\mathbf{E}$ and hence,

$$\chi=-\frac{n^2e^2}{\varepsilon_0(\omega^2\rho-i\omega\gamma+\kappa)}. \tag{3.17}$$

Calling γ/ρ collision frequency ω_C, κ/ρ the square of natural frequency ω_0 and $n^2e^2/\varepsilon_0\rho$ the square of a plasma frequency ω_P,

$$\varepsilon=1-\frac{\omega_P^2}{(\omega^2-i\omega\omega_C+\omega_0^2)}. \tag{3.18}$$

Such models are called Lorentz oscillator models.

3.3 PERMITTIVITIES OF MATERIALS OF INTEREST

Most bulk materials, under the influence of small amplitude electromagnetic fields, can be modeled with either the Drude model or the Lorentz model or a combination of the two. In this section, the permittivity data of several metals (Ag, Au and Cu) and dielectric materials (Si and TiO_2) are given. The data was taken from a public domain webpage, refractiveindex.info [24]. A brief discussion of the permittivities of the materials will also follow. Typically, the data is measured with an optical spectrometer or an ellipsometer and reported in the form of the refractive index rather than the permittivity. The permittivity and the refractive index are related through the following relationship when the quantities have complex values:

$$\varepsilon = (n + ik)^2 = n^2 - k^2 + i2nk. \tag{3.19}$$

Using the above equation, the refractive index data was converted to permittivity data. The range of interest for the purpose of this work is the UV-Vis-IR region that is dominated by the solar radiation. In terms of wavelength, the range approximates to 100-1200 nm. Even thought the visible region ends at about 800 nm, several semiconductors such as Si have their bandgaps at wavelengths that are larger. Since such materials are often used for manufacturing solar cells, it makes sense to extend the range of interest to the IR region upto 1200 nm.

3.3.1 Ag, Au and Cu

The permittivity of Ag in the visible range, 300-800 nm, is shown in Fig.3.1. The blue curve represents the real part $\mathrm{Re}[\varepsilon]$ and the green curve, the imaginary part $\mathrm{Im}[\varepsilon]$. The real part reduces from a positive value of $O(1)$ in the UV region, λ~300nm, to a relatively large negative

value of ~-30 in the red-IR region where λ > 700nm. The imaginary part tends to remain at a relatively constant value of ~2 for all λ > 350nm. The features for λ > 350nm are very similar to what would be expected for a Drude model given in Eq. 3.15. However, the features for λ < 350 nm are not Drude like but rather resemble a Lorentz oscillator model given in Eq. 3.18. The main features of a Lorentz model are: (i) $\mathrm{Re}[\varepsilon]$ shows an inflection at the resonant wavelength about which its value changes from a relatively large value to a smaller value in the direction of increasing wavelength. At lower wavelengths, there is a larger polarization response to the applied field whereas, at larger values of λ, the polarization is diminished. However, at λ values that are far away, in either direction, the values of $\mathrm{Re}[\varepsilon]$ have equal asymptotes. (ii) $\mathrm{Im}[\varepsilon]$ has a similar asymptotic behavior, however their values are zero. Faraway from resonance, there is no loss in the material. At resonance, $\mathrm{Im}[\varepsilon]$ has a maximum. The Drude model, in contrast, has a monotonic behavior with an increasing, positive $\mathrm{Re}[\varepsilon]$ and decreasing and eventually negative $\mathrm{Im}[\varepsilon]$ in the direction of increasing λ.

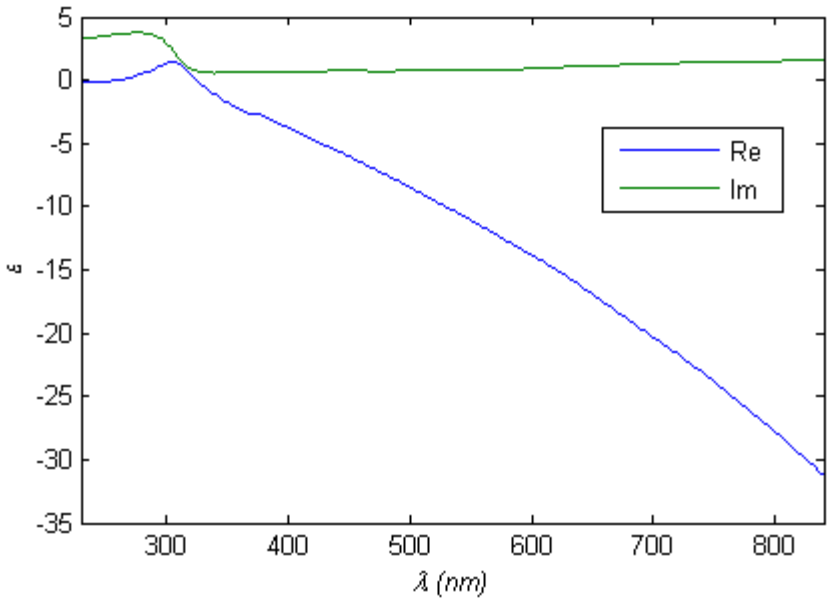

Figure 3.1: Complex permittivity of Ag as a function of wavelength of light in the visible range. The real part is negative and monotonically decreasing in magnitude for the most part of the range. The imaginary part has values in the range of 0 to 5 that become an order of magnitude smaller than the real part for $\lambda > 750$ nm.

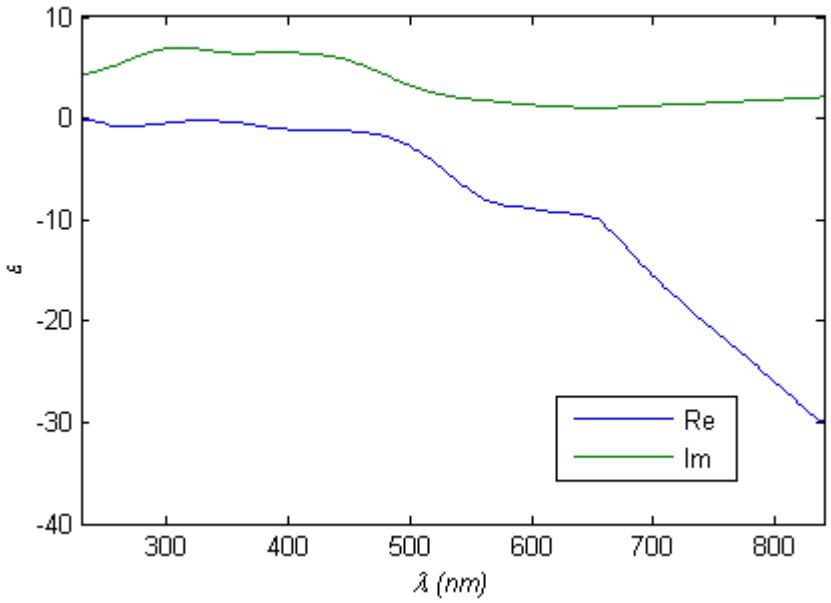

Figure 3.2: Complex permittivity of Au as a function of wavelength of light in the visible range. The real part is negative and monotonically decreasing in magnitude for the most part of the range. The imaginary part has values in the range of 0 to 10 that become an order of magnitude smaller than the real part for $\lambda > 750$ nm.

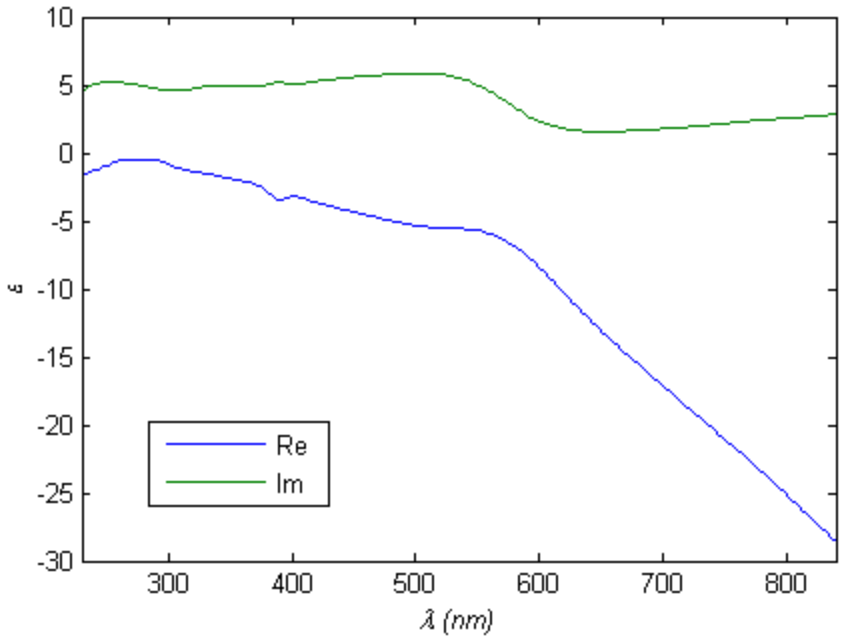

Figure 3.3: Complex permittivity of Cu as a function of wavelength of light in the visible range. The real part is negative and monotonically decreasing in magnitude for the most part of the range. The imaginary part has values in the range of 0 to 7 that become an order of magnitude smaller than the real part for $\lambda > 750$ nm.

Lorentz oscillator, in case of a metal, represents the resonance of bound electrons that do not participate in conduction. Figs. 3.2 and 3.3 show the behavior of the complex permittivity of Au and Cu respectively. In contrast to Ag, several non-Drude-like features can be observed upto a $\lambda < 650$ nm for Au and Cu.

3.3.2 Si and TiO_2

Semiconductors, typically, have a band-gap. The electronic structure of semiconductors is such that, unlike metals, most electrons that participate in optical interactions cannot possess all possible values of total energies that they may obtain from an incident photon. Instead, such

continua of energies are separated by a gap that is generally referred to as a band-gap. The continuum with the lower energy is called a valence band, mainly because it is supposed to represent only the most labile electrons in the atoms that can be easily ionized to form positive ions. The unoccupied, at least at low temperatures, continuum that has a higher minimum energy is called the conduction band since it represents a state in which electrons can assume unbounded kinetic energy—making them behave as if they are a part of a metal's conducting electrons [25]. Some semiconductors have an indirect band-gap in their electronic structure which requires their valence electrons to have a specific crystal momentum in order to jump the energy gap. Effectively, it results in an extra energy requirement. The extra energy is, however, much smaller than that required for the energy corresponding to the gap. The transition is made less probable by the fact that the crystal momentum needs to be supplied by the lattice vibration states known as phonons. Of course, this means that at relatively large temperatures, the transition becomes more likely [25].

The permittivity of Si is shown in Fig. 3.4. The data was taken from an online resource [24]. Unlike metals, the relative permittivity of semiconductors has all positive values in the visible range due to the lack of free electrons. $\mathrm{Re}[\varepsilon]$ is relatively large for silicon compared to several other insulting materials such as TiO_2, SiO_2, Al_2O_3 and Si_3N_4. A relatively large value of $\mathrm{Re}[\varepsilon]$ leads to a relatively strong plasmonic coupling between a nano-antenna and a planar device (discussed further in Chap. 4). As a result, Si is more relevant for the current study. Moreover, it is a very popular solar cell material because it is inexpensive and has relatively well established processing technology. The spectral permittivity of Si in the visible region shows two characteristic resonances that correspond to the two direct transitions at the Γ point of the valence band [25, 26]. The indirect gap corresponding to ~1100 nm that is not covered in the

range does not really show any specific spectral features since the corresponding absorption process is much less likely.

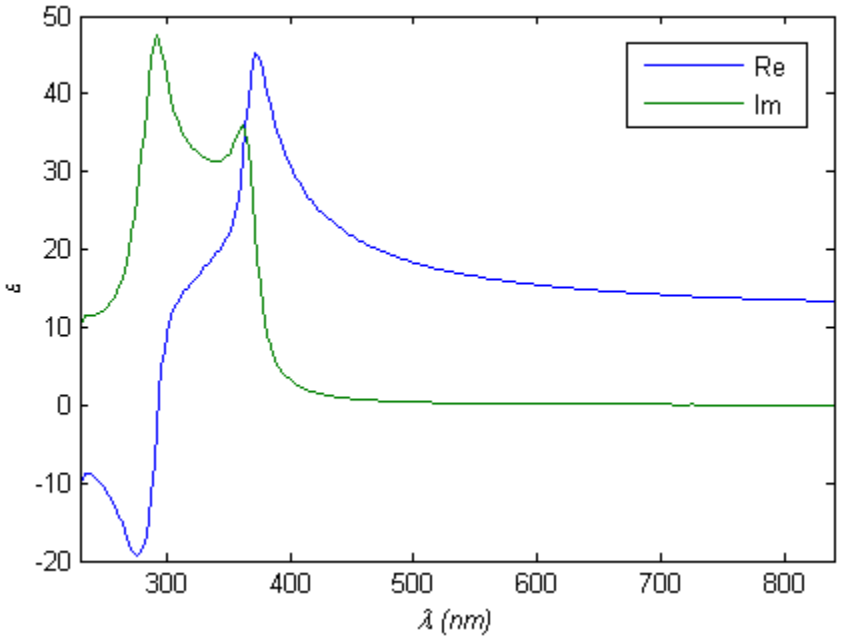

Figure 3.4: Complex permittivity of Si as a function of wavelength of light in the visible range. The real part is positive and larger than 10 for the most part of the range shown here. The imaginary part is very close to zero until $\lambda < 400$ nm because the band-gap becomes direct only for relatively larger energies corresponding to ~400 nm. The real part shows a corresponding resonance in its values. The second resonance peak at ~300 nm corresponds to another direct transition with relatively larger band energy [25].

TiO_2 is a popular electrode material for technologies for photocatalytic water-splitting [27, 28]. It is a direct band-gap semiconductor that is known to perform better with plasmonic coupling. Hence, there is interest in studying the fields near a coupled nano-antenna. Although TiO_2 can be found in one of several crystal structures, here, only one structure called Rutile will be considered to study how TiO_2 couples with plasmonic nanospheres. Such a choice is justified, vaguely, since the relative permittivity data for the other phases—Anatase and Brookite—are rather difficult to

find. Moreover, the only difference between them arises near the wavelength corresponding to their optical absorption—which, only in the case of Anatase corresponds to an indirect bandgap. The values of ε for the other parts of the spectrum must be similar for each phase since, to the leading order, the permittivity arises due to the dipole polarizability of each atom. Further, the polarizability has to come about from all electrons that do not interact to form bonds.

Rutile is known to be a birefringent material. Here, only data for its larger value of relative permittivity that is known as the extraordinary permittivity in the birefringent optics literature is used. Since it was not possible to find data for the other, ordinary permittivity, Rutile is considered to be isotropic for the current calculations. The goal of the calculations is to get some idea about how a nanosphere couples to a slab made of TiO_2. As shown in Fig. 3.5, there one distinct absorption peak around ~ 300 nm and a corresponding inflection in $\mathrm{Re}[\varepsilon]$. Above λ = 400 nm, the behavior is predominantly similar to a transparent material with $\mathrm{Re}[\varepsilon] \sim 7$. The increase in $\mathrm{Im}[\varepsilon]$ is much sharper than that for Si because of a direct band-gap.

In devices, typically, an inert spacer is put over the active semiconductor layer so that the active layer remains chemically and tribologically protected. Although the optical consequence of such spacers is to reduce the plasmonic coupling [29], hence, the optical properties of such materials are discussed here to develop a detailed understanding.

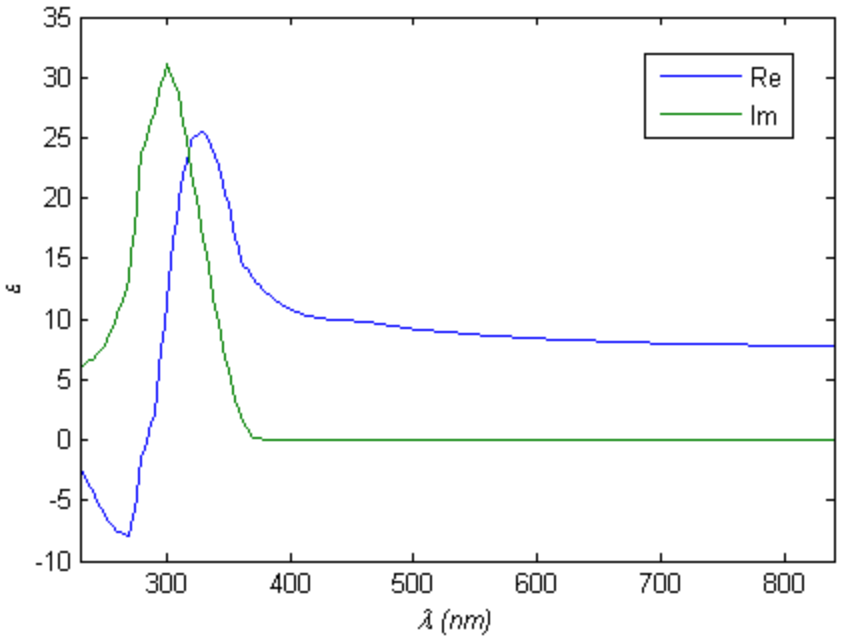

Figure 3.5: Complex permittivity of TiO_2 as a function of wavelength of light in the visible range. The real part is positive and larger than 7 for the most part of the range shown here. The imaginary part is very close to zero until $\lambda < 400$ nm because the band-gap. The real part shows a corresponding resonance in its values [25].

3.3.3 SiO_2

One of the most popular transparent materials used in a laboratory is either pure SiO_2 in the form of quartz, fused silica or a SiO_2 based glass such as soda-lime glass. The additives in the glass make it less temperature resistant while giving it better flow properties that can help in low temperature processing. Here, we will just look at the relative permittivity of crystalline SiO_2 rather than its glassy versions. Their permittivities differ only slightly and all of them are transparent in the visible range of the spectrum. None of them undergoes any transitions to give rise to a non-zero $\mathrm{Im}[\varepsilon]$ in the visible region.

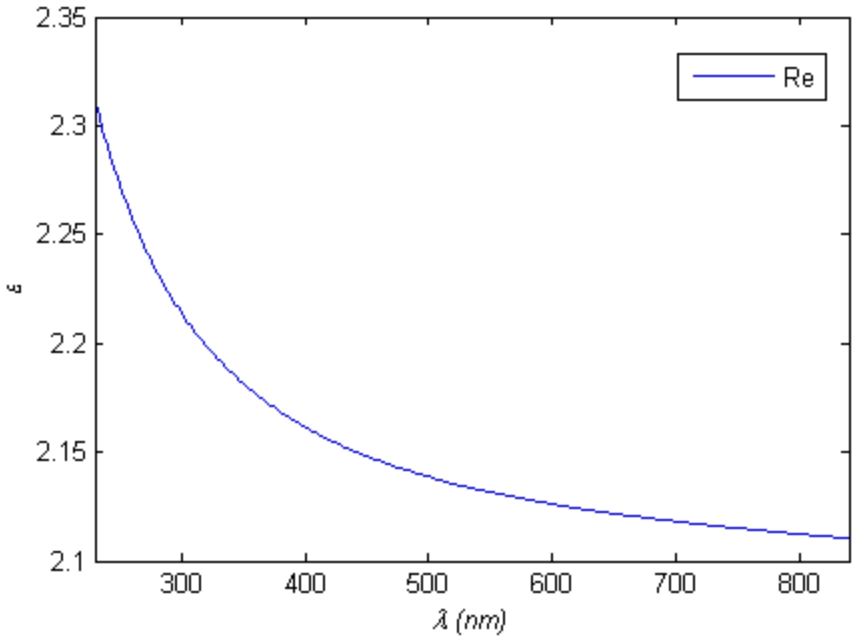

Figure 3.6: Permittivity of SiO_2 as a function of wavelength of light in the visible range. The real part is positive and larger than 2 for the most part of the range shown here. The imaginary part is zero for practical purposes [25].

The relative permittivity of SiO_2 is in between 2.1 and 2.35 for the wavelength range shown in Fig. 3.6. It is relatively lower than that of Si or TiO_2.

3.3.4 Ideal Drude Metals

The Drude model given in Eq. 3.15 can be used to evaluate the relative permittivities for given values of the plasma frequency ω_P and the collision frequency ω_C. Both frequencies are relatively large in the wavelength range of interest. Here, instead, the corresponding plasma wavelength $\lambda_P \equiv \frac{2\pi c}{\omega_P}$ and collision energy $E_C \equiv \hbar\omega_C$ will be used since their values, as will be

seen, are more tangible to deal with. As can be seen from Eq. 3.15, λ_P is the wavelength at which $\varepsilon = 0$ for $E_C = 0$. Since we require $\varepsilon \sim -2$ near plasmon resonance in a medium with relative permittivity equal to one, it makes sense to choose a λ_P that lies in the lower end of the wavelength range of interest. We will set $\lambda_P = 290$ nm. The collision energy E_C will be allowed to assume the following values: 0.1, 1 and 2 eV. The corresponding energy value for the plasma wavelength is $E_P \sim 4.3$ eV.

An expression for $\mathrm{Re}[\varepsilon]$ can be derived from Eq. 3.15. After some simple algebra, one finds $\mathrm{Re}[\varepsilon] = 1 - \dfrac{\omega_P^2}{\omega^2 + \omega_C^2}$. As shown in Fig. 3.7, the curves asymptote at $\mathrm{Re}[\varepsilon] = 1$ as $E_C \to \infty$. Metals with a relatively large E_C have a relatively small value of $|\mathrm{Re}[\varepsilon]|$ and cross over from a positive value to a negative value at a relatively large λ. Similar to $\mathrm{Re}[\varepsilon]$, an expression for the imaginary part $\mathrm{Im}[\varepsilon]$ derived from Eq. 3.15 is given by $\mathrm{Im}[\varepsilon] = \dfrac{\omega_C}{\omega} \dfrac{\omega_P^2}{\omega^2 + \omega_C^2}$. It stays positive throughout the spectrum and seems to increase in value as the value of E_C is increased from 0.1 to 2 eV as shown in Fig. 3.8. However, unlike $\mathrm{Re}[\varepsilon]$, $\mathrm{Im}[\varepsilon]$ approaches zero, both, as $E_C \to 0$ and as $E_C \to \infty$; implying that there is a maximum for a given ω_P and ω. However, for applications of interest in the current work, a relatively small $\mathrm{Im}[\varepsilon]$ and a relatively large $\mathrm{Re}[\varepsilon]$ are required, necessitating a situation where $E_C \to 0$.

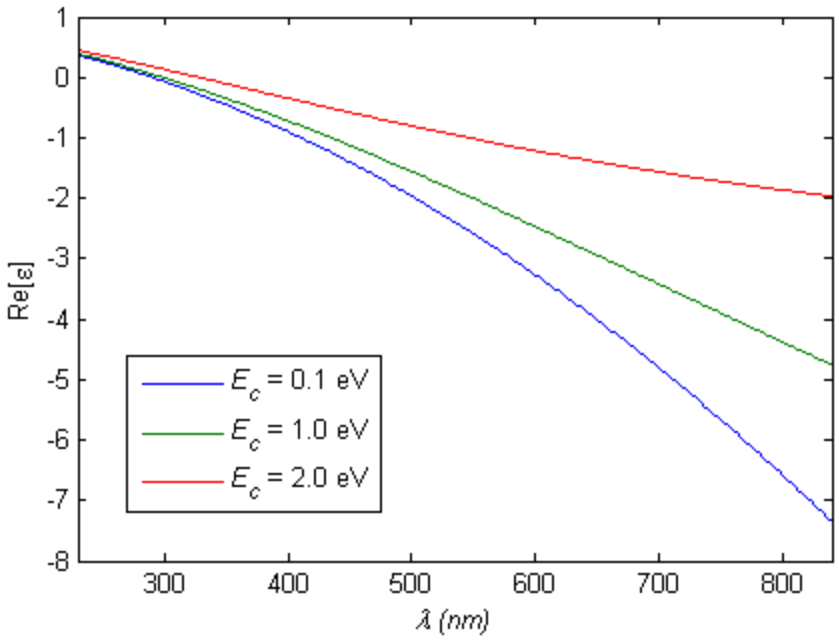

Figure 3.7: The real part of the relative permittivity of a hypothetical Drude metal that has a plasma wavelength $\lambda_P = 290$ nm and collision energy E_C values 0.1 eV (blue), 1.0 eV (green) and 2.0 eV (red). An increase in E_C leads to an increase in the magnitude of $\mathrm{Re}[\varepsilon]$. The curve approaches $\mathrm{Re}[\varepsilon] = 1$ as $E_C \to \infty$.

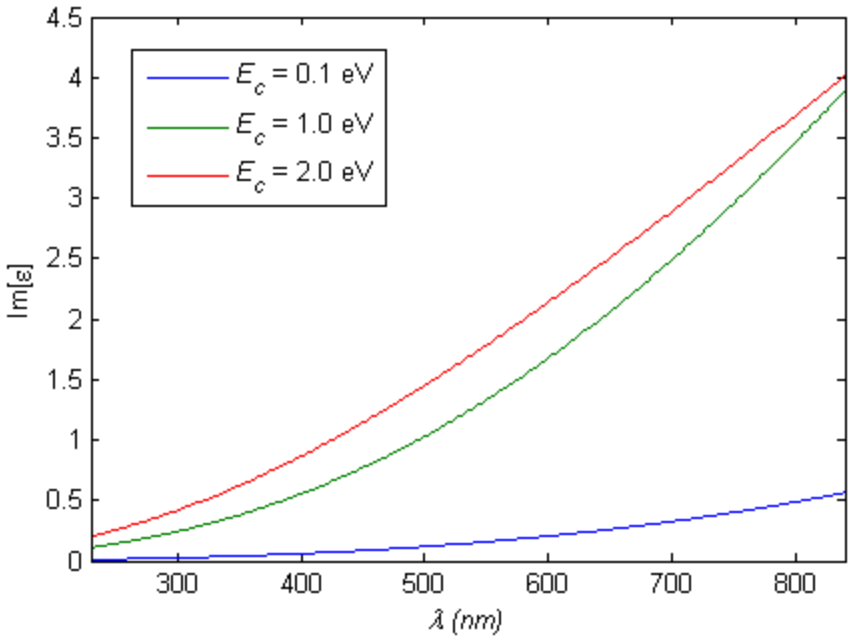

Figure 3.8: The real part of the relative permittivity of a hypothetical Drude metal that has a plasma wavelength $\lambda_p = 290$ nm and collision energy E_C values 0.1 eV (blue), 1.0 eV (green) and 2.0 eV (red). An increase in E_C leads to an increase in the magnitude of $\mathrm{Im}[\varepsilon]$ for the current values of E_C.

4 METAL NANOPARTICLE NEAR A DIELECTRIC SLAB

4.1 INTRODUCTION

The electromagnetic interactions among several metal nanospheres are known to result in several interesting phenomena, physics and effects that are a part of the broad field of study that is known as plasmonics—a portmanteau similar to electronics for the quantized package of energy in oscillating electron plasma of metals [30]. Several researchers have hailed plasmonics as an important frontier in nanoscale optical science research [31]. One of the most significant applications is in the field of efficient energy harvesting in the context thin film photovoltaics; wherein the presence of such metal nanoparticles on the surface of a planar device can significantly improve the electronic current for a given amount of incident light fluence [6, 7]. Several researchers, who are primarily interested in the field of highly efficient light devices, have explored several geometries and designs that optimize the efficiency of the devices with the aid of plasmonic nanoparticles that are incorporated at various locations. The number of articles in the field is astronomical—it seems sufficient to just cite a popular review paper here. An interested reader can explore the internet for the articles cited in or those citing Ref. [6]. The goal of the present work is to study this class of problems by abstracting the nanoparticle and the device so that the fundamentals aspects of their interactions can be analyzed and new physical insights can be arrived upon. So, rather than worrying about several design related aspects of a device or the nanoparticle or its location with respect to the device, here, it is just assumed, for now, that the device is a semi-infinite slab made of a material that may be chosen to have the same properties as typical device materials such as semiconductors and the nanoparticle is

assumed to be spherical. The nanoparticles are thought to not exhibit any quantum-confinement effects—they can be thought to behave like the bulk materials even when their size is small enough to be similar to length scales of its crystal lattice, electron transport related length scales such as mean free path and other coupled scales relating the electrons to the lattice. The dielectric slab, which represents the device, is analyzed in the context of how much light energy flux is entrained within it due to the presence of the nanospheres. A connection can be made to observed electron current enhancements by arguing that the current, essentially, depends on the photon fluence rate in to the slab—disregarding possible interaction between the nanospheres and the substrate that could augment the substrate's material character or any non-linear field couplings. Hence, in this "naïve" inquiry, improving the device is equivalent to increasing the light fluence rate into the slab—which, from now, will be called the Trapped Flux *F*. It will turn out that *F* is a function of several system parameters p_i. The goal for this work is to study $F(p_i)$ using the methods of analyses and calculation of linear electromagnetic coupling discussed in Chap. 2; and to develop an insight in to the underlying numerical and physical artifacts of such coupling as well as tie them to useful concepts that will be important for the development of devices that use linear electromagnetic field coupling. Further, the full wave nature will be disregarded for the current problem so that the problem can be analyzed for nanospheres that only have strong near-field interactions. Such an assumption can be justified based on the observation that several experimental research groups have used very tiny particles for their devices, but, here, it is preferable because it makes most sense from the perspective of a rigorous mathematical analysis of problem. It may very well be possible that, under certain circumstances, large spheres or other relatively hard to analyze designs may be more efficient but this work is

focused on the numerical and theoretical analysis of the problem from the most elementary starting point to which complexities can be added eventually.

4.1.1 Incident field's interaction with the semi-infinite slab

The electric and magnetic fields can be generated from scalar fields using the decomposition discussed in Chap. 2; even when the fields are described in the Cartesian coordinate system. Eqs. 2.40 and 2.41 can be modified by just replacing the position vector with a unit vector p_i such that $p_i k_i = 0$, where k_i is the wavevector. Since, the vector Helmholtz equation is a set of three equations, one would expect three scalar fields to completely represent them, but the perpendicularity condition, that is necessary for the solution to become a travelling wave, reduces the requirement to only two scalars. Further, a unique k_i is required to deem the solution a travelling wave. Eventually, only one unit vector need be multiplied to one solution of scalar wave equation to generate one solution for the vector equation. So, in some vague sense, studying only the scalar solution for the case of Cartesian Helmholtz equation is apriori to analyzing its effects on the vector solutions. The main argument here is that given any time harmonic function, a spatial Fourier transform can be performed on it to evaluate its constituent travelling wave modes making it possible to do something similar to the solution of the vector equations. In such a situation, the effects of the plane waves made of various k_i are the ones that are only required to analyze the problem since any other beam form can be reconstructed out of such solutions. Of course, one may inquire about complex k_i that are required in case of an

absorbing medium—unless a medium is not entirely absorbing it may be possible to account for imaginary part of k_i s by keeping them as a part of the Fourier coefficients of the beam.

The incident light will be considered to be a plane wave that is incident at various angles and polarizations upon the slab and given by $\mathbf{E}^i = (E^{i0T}\hat{\mathbf{p}}^{iT} + E^{i0P}\hat{\mathbf{p}}^{iP})\exp(i\mathbf{k}^i \cdot \mathbf{r})$, as discussed in Chap. 2. The unit vectors and the superscripts carry the same meaning as in Chap. 2: *i* denotes incidence, *T* denotes transverse polarization with respect to the plane of incidence, *P* denotes polarization in the plane of incidence, 0 denotes the amplitude and **p** represents a vector in the direction of the polarization. The other symbols have their usual meanings. Similarly, the transmitted and reflected fields are given by $\mathbf{E}^t = (T^T E^{i0T}\hat{\mathbf{p}}^{tT} + T^P E^{i0P}\hat{\mathbf{p}}^{tP})\exp(i\mathbf{k}^t \cdot \mathbf{r}).$ and $\mathbf{E}^r = (R^T E^{i0T}\hat{\mathbf{p}}^{rT} + R^P E^{i0P}\hat{\mathbf{p}}^{rP})\exp(i\mathbf{k}^r \cdot \mathbf{r})$. The wavevectors can have a complex magnitude in case the medium they are travelling in is dissipative. Referring to figure 2.1 in Chap. 2, the relative orientations of $\mathbf{k}^\mu$ with respect to the interface are such that the wavevectors can be treated as vectors that can have a complex amplitude but a real unit vector corresponding to them—a situation that is true only when medium that the wave transmits into has real permittivity, in which case, the amplitude is not complex anyway. In the presence of a dissipative medium, both, the amplitude and the unit vector components need to assume complex values so that the Snell's law given in Eq. 2.18 of Chap. 2 can be satisfied while allowing $k^t \equiv \sqrt{\varepsilon^S}\,\omega\sqrt{\mu_0\varepsilon_0} = \sqrt{\varepsilon^S}k^i$ to remain complex valued since the substrate's relative permittivity ε^S is complex valued. The normal component k_1^t is given by $k_1^{t\,2} = \varepsilon^S k^{i\,2} - k_2^{i\,2} - k_3^{i\,2} = (\varepsilon^S - 1)k^{i\,2} + k_1^{i\,2}$. At any given point **r**, the total electric and magnetic fields can be represented as an expansion in χr dependent terms, where $\chi \equiv k^\mu a, \mu = i, r, t$ and

a is some relevant length scale. The expansion can be further represented in terms of the amplitudes of some relevant harmonics that correspond to, say, the numerical method used for the solution of the problem.

4.1.2 Calculation method for fields around spheres present in the vicinity of a semi-infinite plane slab

The problem of field calculation for spheres present in the vicinity of semi-infinite slab is best analyzed, at least in the beginning, in the asymptotic limit as certain linear features within the system are small enough to neglect the wave effects corresponding to them—such a method of analysis allows one to build the problem from ground-up, addition of algebraic and numerical complexities is made in a systematic manner so that one can keep a track of the intricacies. At present, the analysis and calculations that lead up to the solution of the full problem are intended for discussion here.

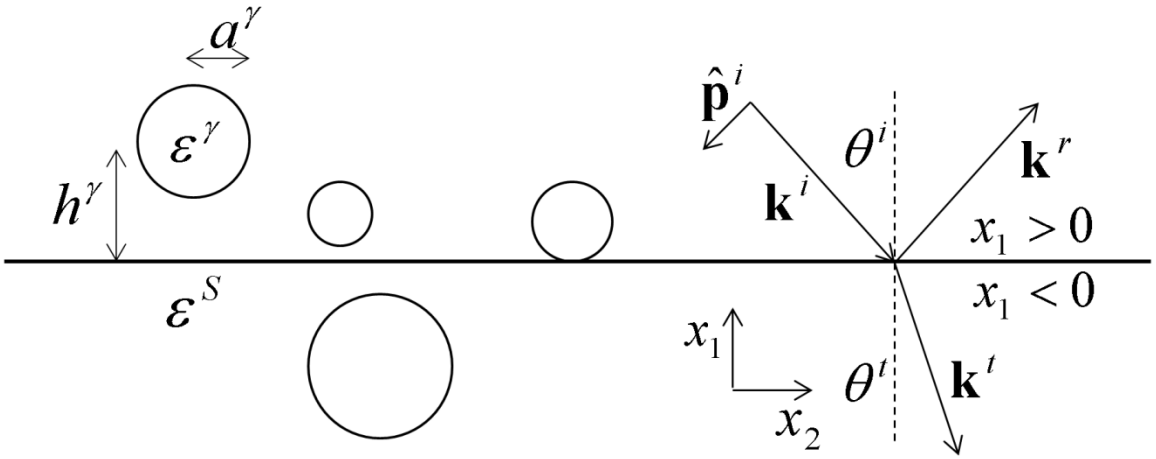

Figure 4.1: The figure depicts the incident plane wave field and the relevant form of distribution of the spheres in the vicinity of the dielectric interface. The lower half space have an electric permittivity ε^S relative to the upper space. The spheres are allowed to approach and almost touch the interface, but not be present in both media across the interface. The superscript γ denotes the sphere count. Orientations of the incident (*i*), reflected (*r*) and transmitted (*t*) wavevectors with respect to the axes, the interface with the dielectric half-plane and its normal along with the corresponding angles are also included. Only one polarization vector is shown since all other orientations can be found from its and the wavevector's orientations.

Fig. 4.1 depicts the problem geometry of interest. The spheres are allowed to touch the interface from either side, but not cut across it since under such a circumstance, it would not be possible to solve using the multipole method discussed in Chap. 2. It would require the use of a method that allows piecewise or discontinuous boundary conditions to accommodate the change in the media. One may think of applying the conditions in a point-wise sense by discretizing the boundary, but even then, the discontinuity as a function of θ would require the use of several harmonics that, eventually, amount to putting several points near the interface using some collocation scheme.

The multipole method requires that the applied field is represented in terms of Laplace harmonics with origins that coincide with the center of each sphere. For a sphere located at $\mathbf{r}^\gamma$

such that $x_1^\gamma > 0$, the driving electric field experienced by the sphere is the sum of the incident and reflected fields that is given by

$$\mathbf{E}^d(\mathbf{r}^\gamma) = (E^{i0T}\hat{\mathbf{p}}^{iT} + E^{i0P}\hat{\mathbf{p}}^{iP})\exp(i\mathbf{k}^i \cdot \mathbf{r}^\gamma) + (R^T E^{i0T}\hat{\mathbf{p}}^{rT} + R^P E^{i0P}\hat{\mathbf{p}}^{rP})\exp(i\mathbf{k}^r \cdot \mathbf{r}^\gamma) \quad (4.1)$$

as discussed in Chap. 2. Noticing that $k_1^r = -k_1^i$, $\hat{\mathbf{p}}^{iT} = \hat{\mathbf{p}}^{rT} = \hat{\mathbf{x}}_3$, $\hat{\mathbf{p}}^{iP} = -\sin\theta^i\hat{\mathbf{x}}_1 - \cos\theta^i\hat{\mathbf{x}}_2$ and $\hat{\mathbf{p}}^{rP} = -\sin\theta^r\hat{\mathbf{x}}_1 + \cos\theta^r\hat{\mathbf{x}}_2$: all from Chap. 2, one can simplify Eq. 4.1 to give the following set of equations for the driving electric field for the upper half-space:

$$\begin{aligned} E_1^d(\mathbf{r}^\gamma) &= -E^{i0P}\sin\theta^i \exp(i\mathbf{k}^i \cdot \mathbf{r}^\gamma)(1 - R^P), \\ E_2^d(\mathbf{r}^\gamma) &= -E^{i0P}\cos\theta^i \exp(i\mathbf{k}^i \cdot \mathbf{r}^\gamma)(1 + R^P), \\ E_3^d(\mathbf{r}^\gamma) &= E^{i0T}\exp(i\mathbf{k}^i \cdot \mathbf{r}^\gamma)(1 - R^T). \end{aligned} \quad (4.2)$$

The driving magnetic field can also be calculated in a similar manner, albeit it would not eventually contribute significantly to calculated harmonic amplitudes since, as discussed in Chap. 2, the induced magnetic field is insignificant to the leading order in χ^n for field coupling among small non-magnetic spheres. A similar expression can be found for the driving field for the case when $x_1^\gamma < 0$.

$$\begin{aligned} E_1^d(\mathbf{r}^\gamma) &= -E^{i0P}\sin\theta^t \exp(i\mathbf{k}^t \cdot \mathbf{r}^\gamma)T^P, \\ E_2^d(\mathbf{r}^\gamma) &= -E^{i0P}\cos\theta^t \exp(i\mathbf{k}^t \cdot \mathbf{r}^\gamma)T^P, \\ E_3^d(\mathbf{r}^\gamma) &= E^{i0T}\exp(i\mathbf{k}^t \cdot \mathbf{r}^\gamma)T^T. \end{aligned} \quad (4.3)$$

$\mathbf{E}^d(\mathbf{r}^\gamma)$ can be represented in terms of regular Laplace harmonics by using the second equation in Eqs. 2.66 in Chap. 2—$\mathbf{E}^d = \sum_n \sum_{m=-n}^{n} (n+1)\nabla\Phi_{nm}^{\gamma R}$.

Clearly, the exponential terms need to be taken care of. Here, the same argument, as always, would be used; it will be assumed that the distances r^γ are such that $\exp(i\mathbf{k}^\mu \cdot \mathbf{r}^\gamma)$, $\mu = i,t$ approaches one. Vector $\mathbf{r}^\gamma$ can be represented as $(x_1^\gamma, \bar{\rho}^\gamma)$, where $\bar{\rho}^\gamma \equiv (x_2^\gamma, x_3^\gamma)$ so that the exponential is $\exp(ik_1^\gamma x_1^\gamma)\exp(i\mathbf{k}_\rho^\gamma \cdot \bar{\rho}^\gamma)$. The first term can approach one if the distance of the sphere from the interface is small enough: $k_1^\gamma h^\gamma \to 0$. The second term, however, needs to be looked at as $\exp(i\mathbf{k}_\rho^\gamma \cdot \bar{\rho}_0^\gamma)\exp(i\mathbf{k}_\rho^\gamma \cdot \Delta\bar{\rho}^\gamma)$, where the prefix Δ symbolizes a small change. Essentially, given any location on the interface, as long as region of interest represented by the span $\Delta\bar{\rho}^\gamma$ is such that $k_\rho^\gamma \Delta\rho^\gamma$ is a small compared to one. The exponential multiplying the Δ term is just a constant that can be absorbed into the amplitude of the field. Several such regions can be considered as long as they form a set of islands that satisfy the condition within them and the distance between them is such that the condition is violated, i.e., $k_\rho^\gamma \Delta\rho^\gamma$ is at least *O*(1).

Representation in terms of the Laplace harmonics reduces to the representation of constant vector $\mathbf{E}^d(\mathbf{r}^\gamma)$. The vectors in the basis $\hat{\mathbf{x}}_i$ can be generated from regular harmonics through gradient operation in the following way:

$$
\begin{aligned}
-\zeta_1 E^{i0P} \sin\theta^t \hat{\mathbf{x}}_1 &= 2\partial_i \Phi_{10}^{\gamma R}, \\
-\zeta_2 E^{i0P} \cos\theta^t \hat{\mathbf{x}}_2 &= 2\partial_i [\Phi_{1,-1}^{\gamma R} - \frac{1}{2}\Phi_{11}^{\gamma R}], \\
\zeta_3 E^{i0P} \hat{\mathbf{x}}_3 &= 2i\partial_i [\Phi_{1,-1}^{\gamma R} + \frac{1}{2}\Phi_{11}^{\gamma R}].
\end{aligned}
\tag{4.4}
$$

The constants ζ_i represent the reflection and transmission coefficient related factors that appear in Eqs. 4.2 and 4.3 respectively. The choice of their values depend on $\mathrm{sgn}(h^\gamma)$. The amplitudes of the Laplace harmonics F_{1m}^{γ} can be evaluated from Eq. 4.4.

$$
\begin{aligned}
F_{10}^{\gamma} &= -\frac{1}{2}\zeta_1 E^{i0P} \sin\theta^t, \\
F_{1,-1}^{\gamma} &= -\frac{1}{4}[\zeta_2 E^{i0P} \cos\theta^t + i\zeta_3 E^{i0P}], \\
F_{11}^{\gamma} &= \frac{1}{2}[\zeta_2 E^{i0P} \cos\theta^t - i\zeta_3 E^{i0P}].
\end{aligned}
\tag{4.5}
$$

Everything that is necessary for the evaluation of the scalar fields is in place except the incorporation of the effect of the semi-infinite slab. The method of images will be used here to take the effect into account. The main idea is to have the effect of an interface on a source be accounted for by another source. A source is a singularity that decays in the far-field. The field in the $x_1 < 0$ region also needs to be represented using singularities such that, at the interface, the boundary conditions on **E** and **H** are satisfied. Given a $\mathbf{\Phi}_{nm}^{S\gamma}$ at $\mathbf{r}^\gamma$ such that $x_1^\gamma > 0$, a singularity $\mathbf{\Phi}_{nm}^{S\gamma im}$ in the $x_1 < 0$ region is required to generate the reflection of $\mathbf{\Phi}_{nm}^{S\gamma}$ due to the interface. However, $\mathbf{\Phi}_{nm}^{S\gamma im}$ is only meant as a source for the $x_1 > 0$ region. For the lower half-space, a "ghost" or "virtual" source in the upper region given by $\mathbf{\Phi}_{nm}^{S\gamma g}$ is used to generate the fields. Clearly, full-wave solutions cannot be dealt with using such a method since a change in a

medium would cause a phase mismatch at the interface. The only way would be to resort to the Fourier representation of the source in the upper region followed by simple application of the Fresnel relations for a given value of the wavevector to obtain the reflected and transmitted Fourier components. In the context of the current problem, it would require that the unknown multipole polarizabilities of each sphere be re-represented so that their interaction with the interface can be incorporated in the solution procedure. The reflected fields' would need to be inverse transformed back into the multipole amplitudes followed by their coupling to the other spheres etc. The general scheme would be the following:

1. Represent the scalar functions on each sphere using the Laplace approximation as far as the coupling among spheres is concerned based on the small argument arguments discussed before and in Chap. 2.
2. Represent the plane wave using scalar wave functions using Eqs. 2.40 and 2.41 with the unit vector replaced with $\hat{\mathbf{x}}_1$. The Fourier amplitudes of such a representation can be found in the literature [32]. The boundary conditions in terms of such functions can also be evaluated and their application would result in the Fresnel coefficients that relate the scalar incident, reflected and transmitted fields [32]. These fields need to be used as the driving fields for the spheres located near the interface as discussed in Fig. 4.1. Due to the Laplace approximation, the fields need only to be evaluated at the centers of the spheres—which, essentially, amounts exactly to what is discussed in the section previous to this one. The incident field vector can be populated thusly.
3. Incorporating the interaction of the various multipoles located at the centers of the spheres with the interface would require the representation of the amplitudes as those of the Helmholtz equation as discussed in Chap. 2 followed by representation of outward

travelling wave solutions in terms of their Fourier amplitudes. For this, only the representation of the Green's function would be necessary—other multipoles can be generated from it using certain derivative operations in a manner similar to those of Laplace harmonics [21]. For the scalar Green's function given by $g(\mathbf{r}) = \frac{\exp(ikr)}{4\pi r}$ for a given medium with wavevector magnitude *k*, $g(\mathbf{r}) = \int_{-\infty}^{\infty}\int g(k_2,k_3)\exp(i\mathbf{k}\cdot\mathbf{r})dk_2dk_3$ with **k** changing its value as one crosses the interface—the details are immaterial here [32]. Let a differential operation $\Omega_{nm}(\hat{\partial}_i)$ be such that $\Omega_{nm}g = \Psi_{nm}^H$, where Ψ_{nm}^H is an outward propagating Helmholtz harmonic given by $\Psi_{nm}^H = c_{nm}h_n^{(1)}(kr)P_{nm}(\cos\theta)e^{im\phi}$ with c_{nm} as simple constants. So, the harmonics are:

$c_{nm}{}^{-1}\Psi_{nm}^H = \int_{-\infty}^{\infty}\int g(k_2,k_3)[\Omega_{nm}\exp(i\mathbf{k}\cdot\mathbf{r})]dk_2dk_3$ and the term in the square brackets would lead to an additional multiplier that is a linear combination of k_i, k_ik_j and $k_ik_jk_l$ where the indices indicate different components that arise from the operation depending on the value of *n* and *m*. Eventually, the all "plane waves" can be added together by converting the Fourier transformed harmonics into equivalent plane wave amplitudes [32] that are allowed to reflect followed by addition of the reflected field to the incident multipole field such that it affects all spheres. The translation, in such a case, would just lead to a phase factor as would be the case in case of plane waves. Thereafter, the Fourier amplitudes need to be integrated at the centre of each sphere followed by the evaluation of the corresponding Laplace harmonic amplitudes by using their orthogonality and that near a sphere, $kr \to 0$. It is not clear at the moment if the required integrals permit an analytical evaluation.

4. The resulting system of linear equations would have to be solved using numerical computations.

In the integral representation picture, such as the one discussed by Lukosz and Kunz [32], the interaction occurs through the reflection of the component plane waves—something that is arrived upon by the application of the boundary conditions to the component scalar plane waves. For calculations involving several spheres, it seems more sensible to avoid the steps involving the evaluation of the integrals in order to populate the coefficient matrix—not just for computational efficiency, but also for analytic ease. Moreover, the integrals required for the evaluation of the fields don't seem strictly analytic. As an example, one can consider the integrals in Eq. 2.37 and 2.39 of Ref. [32]. Here, instead, we incorporate the interfacial coupling effects in the relevant coupling region given by $kr \to 0$ using a self-consistent method that does not violate any boundary conditions required by the problem but just solves the problem in the limit. After the calculations are performed, one can use the calculated dipole moment as a source to evaluate the wave effects in the near and far-field using an integral representation similar to the one discussed above.

Proceeding with the method of images for the current problem, let a scalar electric singularity $\Phi_{nm}^{S\gamma}$ be located at $\mathbf{r}^{\gamma}$ such that $x_1^{\gamma} > 0$. Let its image $\Phi_{nm}^{S\gamma im}$ be located at $\mathbf{r}^{\gamma im}$ such that $x_1^{\gamma im} = -x_1^{\gamma}$ and $x_j^{\gamma im} = -x_j^{\gamma}$, $j = 2,3$. Further, let its virtual image $\Phi_{nm}^{S\gamma g}$ be located at $\mathbf{r}^{\gamma}$. At the interface given by $x_1 = 0,$ we want the corresponding E_2, E_3, H_2 and H_3 to be continuous across the interface. To the leading order in χ, $\mathbf{E}_{nm} = -n\nabla\Phi_{nm}^{S}$, so, the parallel components require continuity of $\nabla_{\rho}\Phi_{nm}^{S}$, where ρ denotes surface operations. However, the leading order

contribution to **H** is $O(\chi)$, given by $\mathbf{H}_{nm} = \frac{-i\chi}{\eta}\nabla\times(\mathbf{r}\,\Phi^{S}_{nm}),$ so its contribution needs to be considered. Again, its surface effects require the continuity of $\frac{\chi}{\eta}[\mathbf{r}\times(\nabla\Phi^{S}_{nm})]_{\rho}.$ The term in the square brackets can be simplified further:

$[\mathbf{r}\times(\nabla\Phi^{S}_{nm})]_{\rho} = [(\mathbf{x}_1+\bar{\rho})\times(\partial_1\Phi^{S}_{nm}+\nabla_{\rho}\Phi^{S}_{nm})]_{\rho} = [\mathbf{x}_1\times\nabla_{\rho}\Phi^{S}_{nm}]+[\bar{\rho}\times\partial_1\Phi^{S}_{nm}].$ The quantities *r* and ϕ do not change sign upon moving from $\Phi^{S\gamma}_{nm}$ to $\Phi^{S\gamma\,im}_{nm}$ while maintaining $x_1 = 0.$ Only, the quantity μ does and consequently $P_{nm}(\mu)$ changes by $(-1)^{n-m}$. The resulting equation connecting the image and virtual image amplitudes Λ^{im}_{nm} and Λ^{g}_{nm} is the following:

$$1+(-1)^{n-m}\Lambda^{im}_{nm} = \Lambda^{g}_{nm}. \tag{4.6}$$

The second equation needs to be derived from the **H** boundary condition. The presence of 1-components leads to a change of sign in both terms and consequently, the following equation is arrived upon:

$$1-(-1)^{n-m}\Lambda^{im}_{nm} = \varepsilon_S\Lambda^{g}_{nm}. \tag{4.7}$$

Here, ε_S is the permittivity of the substrate—the ratio between the pre-multiplier $\frac{\chi}{\eta}$'s value upon moving from the substrate to the medium above it. Solving Eq. 4.6 and 4.7, the following equations can be found:

$$\Lambda_{nm}^{im} = (-1)^{n-m+1}\frac{\varepsilon_S - 1}{\varepsilon_S + 1},$$
$$\Lambda_{nm}^{g} = \frac{2}{\varepsilon_S + 1}. \tag{4.8}$$

When making such an image system for a sphere embedded in the substrate, some simple changes need to be made along with the fact that the driving field is the transmitted field etc. The conditions given in Eq. 4.8 are identical to those that would be necessary for an equivalent thermal problem with continuity of temperature and heat flux boundary conditions. Essentially, then, one can just solve an equivalent thermal problem followed by an application of transformation constants discussed at the end of Chap. 2 to, effectively, solve the current problem.

4.2 ONE SPHERE ON SEMI-INFINITE SUBSTRATE

Given an incident field E_i^i characterized by the polarization, amplitude and angle of incidence, here, the induced multipoles and, more specifically, the induced electric dipole moment p_i are the quantities of interest. Of course they are coupled linearly to one another. In the equivalent thermal problem, the applied thermal gradient G_i is coupled to E_i^i through $G_i = F_{ij}E_j^i$. And, eventually, $p_i = D_{ij}G_j = D_{ij}F_{jk}E_k^i$. We wish to evaluate the coupling matrix D_{ij} here for several systems involving different metallic nanospheres coupled with various relevant substrates—all of whose optical constants are discussed in Chap. 3.

Currently, we will assume the sphere to be present above the substrate since it seems more relevant from a practical stand point. The driving field, in such a case, is the sum of the incident field with the reflected field and is given by Eq. 4.2. In it, $E_i^i = \begin{bmatrix} -E^{i0P}\sin\theta^i \\ -E^{i0P}\cos\theta^i \\ E^{i0T} \end{bmatrix}$ and $E_i^r = R_{ij}E_j^i$, where $\underline{\mathbf{R}} \equiv \begin{bmatrix} -R^P & 0 & 0 \\ 0 & R^P & 0 \\ 0 & 0 & -R^T \end{bmatrix}$ is the matrix of reflection coefficients. The driving field is, therefore, given by $E_i^d = (\delta_{ij} + R_{ij})E_j^i$. The corresponding G_i need to be evaluated through on observation of their relation to the regular multipoles F_{1m}^γ for a γ^{th} sphere. Unlike E_i^d given by $E_i^d = 2\partial_i \sum_{m=-1}^{1} \Phi_{1m}^{\gamma R}$, for G_i, one has $G_i = \partial_i \sum_{m=-1}^{1} \Phi_{1m}^{\gamma R}$—the difference is, essentially, a factor of 2. So, $G_i = \frac{1}{2}E_i^d$ and the matrix F_{ij} is, hence, given by $F_{ij} = \frac{1}{2}(\delta_{ij} + R_{ij})$. As discussed in the previous section of this chapter, care must be taken to factor in the phase factor that

depends on the location of the γ^{th} sphere on the interface in to E_i^i from the beginning so that the exponential terms in Eq. 4.2 can be fully neglected. Within G_i, one cannot really distinguish between G_2 and G_3 unless the coordinate system is fixed. One only needs to solve two problems: (1) The G_1 problem that solve the problem for a $G_1 = 1$ and (2) The G_2 problem for which $G_2 = 1$. The $i = 2,3$-redundancy can be resolved by modifying the solution of the G_2 problem to fit the fictitious G_3 problem followed by a multiplication of the amplitudes of G_i that are obtained from the incident field parameters.

A time-harmonic electric dipole p_i that is assumed to have a direction $\hat{\mathbf{p}}$ will be considered here. The dipole moment of a charge density distribution $\rho(\mathbf{r})$ is given by $p_i(\mathbf{r}) \equiv \int_\Omega \rho(\mathbf{r}')(x_i' - x_i) dV_{\mathbf{r}'}$ for a region of space denoted by Ω. In a region of 3-dimensional space, if a charge density reduces at some point, then, it must increase at some other point so that the total charge is conserved. In addition, the charge needs to flow through that space from the point where its density is reduced to the point where its density increases; unless, of course only a lower dimensional space is being considered wherein the flow may occur in some other dimension. Essentially, it needs to satisfy continuity equation given by $\partial_t \rho + \partial_i J_i = 0$ or $\rho = \frac{1}{i\omega} \partial_i J_i$ for the entire space. As a result, $p_i(\mathbf{r}) \equiv \int_\Omega \rho(\mathbf{r}')(x_i' - x_i) dV'$. Since a point dipole is located at a given point, one can do away with $\mathbf{r}$ by considering it to coincide with the origin. Further, the distribution $\rho(\mathbf{r})$ is such that $\lim_{V_\Omega \to 0} \int_\Omega \rho(\mathbf{r}) dV = 0$, where V_Ω denotes the volume of the region Ω. The limit is such that the region is made to shrink to a point. Without loss of

generality, let us assume that $\hat{\mathbf{p}}$ is oriented along $\hat{\mathbf{x}}_1$. As a result, $p = \lim_{V_\Omega \to 0} \int_\Omega \rho(\mathbf{r}) x_1 dV$. Clearly, the only function that can satisfy such conditions is $\rho(\mathbf{r}) \equiv -p\partial_1 \delta(\mathbf{r})$. More generally, $\rho(\mathbf{r}) = -p_i \partial_i \delta(\mathbf{r} - \mathbf{r}')$ for a point dipole p_i located at $\mathbf{r}'$. In order to find the corresponding current density, we require $\partial_i J_i = -i\omega p_i \partial_i \delta(\mathbf{r})$. Integrating both sides with respect to $x_j dV$, one can see that $\hat{\mathbf{j}} = \hat{\mathbf{p}}$ and consequently, $J_i = -i\omega p_i \delta(\mathbf{r})$ for a point dipole located at the origin. Re-representation of a dipole in terms of a current, in some sense, simplifies the field evaluation since the current is a source in the Maxwell curl equations and, as a result, ties in smoothly with the rest of the current theoretical framework.

The magnetic field of current $J_i(\mathbf{r})$ can be evaluated with the following procedure [17]: The magnetic vector potential **A** can be evaluated from the given current since $\mathbf{A}(\mathbf{r}) = -\int_\Omega g(\mathbf{r}, \mathbf{r}') \mathbf{J}(\mathbf{r}') dV'$. Here, the scalar Green's function *g* is given by $g(\mathbf{r}, \mathbf{r}') \equiv -\frac{\exp(ik|\mathbf{r} - \mathbf{r}'|)}{4\pi|\mathbf{r} - \mathbf{r}'|}$. Thereafter, **H** and **E** can be evaluated in the following way:

$$\mathbf{H} = \nabla \times \mathbf{A} \tag{4.9a}$$

and

$$\mathbf{E} = i\omega\mu_0 \mathbf{A} - \frac{1}{i\omega\varepsilon} \nabla(\nabla \cdot \mathbf{A}). \tag{4.9b}$$

Here, **A** is the solution of the Helmholtz equation given by $(\nabla^2 + k^2)\mathbf{A} = -\mathbf{J}$ [17]. For $J_i = -i\omega p_i \delta(\mathbf{r})$, the integral for **A** results in $A_i = i\omega p_i g(\mathbf{r},\mathbf{0}) = -i\omega p_i \frac{\exp(ikr)}{4\pi r}$. The magnetic field generated by it is given by $\mathbf{H} = \frac{-ik\omega}{4\pi}\nabla\times[\mathbf{p}h_0^{(2)}(kr)] = \frac{ik\omega}{4\pi}\mathbf{p}\times\nabla h_0^{(2)}(kr)$. Since, there is only *r* dependence,

$\mathbf{H} = \frac{ik\omega}{4\pi}\mathbf{p}\times\hat{\mathbf{r}}[k\partial_{(kr)}h_0^{(2)}(kr)] = \frac{ik\omega}{4\pi}\mathbf{p}\times\hat{\mathbf{r}}[k\partial_{(kr)}h_0^{(2)}(kr)] = \frac{-ik^2\omega}{4\pi}(\mathbf{p}\times\hat{\mathbf{r}})h_1^{(2)}(kr)$. The magnetic field generated by outward radiative Helmholtz harmonics $\Phi_{1m}^s = a_{1m}h_1^{(2)}(kr)P_{1m}(\mu)e^{im\phi}$ is

$$\mathbf{H}_m = \frac{-ik}{\eta}\nabla\times(\mathbf{r}\Phi_{1m}^s) = \frac{i}{\eta}\hat{\mathbf{r}}\times\nabla[(kr)\Phi_{1m}^s] = \frac{i}{\eta}\hat{\mathbf{r}}\times[\hat{\mathbf{r}}k\{h_1^{(2)}(kr)[ikr-1]+ih_0^{(2)}(kr)\}a_{1m}P_{1m}(\mu)e^{im\phi}$$
$$+\hat{\theta}ka_{1m}h_1^{(2)}(kr)e^{im\phi}\partial_\theta P_{1m}(\mu)+\hat{\phi}imka_{1m}\frac{1}{\sin\theta}h_1^{(2)}(kr)P_{1m}(\mu)e^{im\phi}]$$
$$=\frac{i}{\eta}[\hat{\phi}ka_{1m}h_1^{(2)}(kr)e^{im\phi}\partial_\theta P_{1m}(\mu)-\hat{\theta}imka_{1m}\frac{1}{\sin\theta}h_1^{(2)}(kr)P_{1m}(\mu)e^{im\phi}].$$

One finds that

$$\frac{\eta k\omega}{4\pi}\begin{bmatrix}0\\ p_2\sin\phi - p_3\cos\phi\\ p_2\cos\theta\cos\phi + p_3\cos\theta\sin\phi - p_1\sin\theta\end{bmatrix} = \sum_{m=-1}^{1}\begin{bmatrix}0\\ -ima_{1m}\frac{1}{\sin\theta}P_{1m}(\mu)e^{im\phi}\\ a_{1m}e^{im\phi}\partial_\theta P_{1m}(\mu)\end{bmatrix}$$
$$=\begin{bmatrix}0\\ ia_{1,-1}\frac{1}{2}e^{-i\phi}+ia_{11}e^{i\phi}\\ a_{1,-1}e^{-i\phi}\frac{1}{2}\cos\theta - a_{11}e^{i\phi}\cos\theta - a_{10}\sin\theta\end{bmatrix}.$$

And eventually, $p_i = \frac{4\pi}{\eta k\omega}(a_{10}, \frac{1}{2}a_{1,-1}-a_{11}, -\frac{i}{2}a_{1,-1}-ia_{11})$. The coefficients a_{1m} correspond to the representation in the Helmholtz harmonics—which, in the small argument limit converge to

the Laplace singular harmonics with a scaling factor of $i\chi^{-2}$ (based on the analysis for $ka \to 0$ situation discussed in Chap. 2). So, the singular Laplace coefficients are $S_{1m} = {ia_{1m}}/{(ka)^2}$ and as a result, $p_i = \frac{4\pi ka^2}{i\eta\omega}(S_{10}, \frac{1}{2}S_{1,-1} - S_{11}, -\frac{i}{2}S_{1,-1} - iS_{11})$.

Since the thermal dipole amplitudes are evaluated later on, one needs to relate p_i to the thermal dipole amplitudes S_{1m}^{th}. The relation comes about because of the relationship between S_{1m} and S_{1m}^{th} discussed at the end of Chap. 2— $S_{1m} = -2S_{1m}^{th}$. Hence,

$$p_i = 8\pi i a^2 \varepsilon_0 \begin{bmatrix} S_{10}^{th} \\ \frac{1}{2}S_{1,-1}^{th} - S_{11}^{th} \\ -\frac{i}{2}S_{1,-1}^{th} - iS_{11}^{th} \end{bmatrix} \tag{4.10}$$

for a dipole present in vacuum. In case of a medium with relative permittivity ε_m, the prefactor in Eq. 4.10 can be changed to $8\pi i a^2 \varepsilon_0 \varepsilon_m$.

Going back to the previous topic of discussion—the relationship between p_i and G_i— the coefficients matrix D_{ij} should have the following form due to the orientation dependence: $D_{ij} = L_1\delta_{ij} + L_2 m_i m_j$, where m_i is the unit normal corresponding to the interface. One finds that, for $m_i = \hat{\mathbf{x}}_1$, $p_1 = (L_1 + L_2)G_1$ and $p_2 = L_1 G_2$. Calling p_i obtained for $G_1 = 1$ and $G_2 = 1$ as p_1^0 and p_2^0 respectively, one obtains $L_1 = p_2^0$ and $L_2 = p_1^0 - p_2^0$. As a result,

$$\underline{\mathbf{D}} = \begin{bmatrix} p_1^0 & 0 & 0 \\ 0 & p_2^0 & 0 \\ 0 & 0 & p_2^0 \end{bmatrix}. \tag{4.11}$$

4.2.1 The G_1 problem

One sphere of radius *a* and relative permittivity ε^p is considered to be present in the upper half-space of an interface located at $x_1 = 0$, similar to the spheres in Fig. 4.1. The slab in the lower half-space, $x_1 < 0$, is assumed to be occupied by a medium of permittivity ε^S. It will be assume that the permittivities ε^ν can be interchangeably replaced with thermal conductivities α^ν, where $\nu = p, S$. A constant thermal gradient $G_1 = 1$ is applied in the upper half-space. As discussed before, the lengths are rescaled with respect to the sphere radius *a*. The temperature $\Phi(\mathbf{r})$ is assumed to be dimensionless. The induced multipoles at the center of the sphere $S_n(h, \alpha^\nu)$ are a function of the height *h* of the center of the sphere above the interface and the thermal conductivities. The multipole order *m* is zero for the axisymmetric problem. In the limit as $h \to \infty$, S_n are those corresponding to a sphere embedded in a medium without an interface. Further, only the *n* = 1 mode is present and consequently $S_1^{th} = -\dfrac{\alpha^p - 1}{\alpha^p + 2}$ as can be derived from Eq. 2.77. The corresponding electromagnetic dipole amplitude is $S_1 = 2\dfrac{\varepsilon^p - 1}{\varepsilon^p + 2}$. In the limit as $\varepsilon^p \to 0$, $S_1 \to -1$ and in the limit as $\varepsilon^p \to \pm\infty$, $S_1 \to 2$. In the context of plasmon resonance, the points at which $S_1(\varepsilon^p)$ is singular are of more interest than its asymptotic behavior since it is rather physically difficult to have a material with either a zero or infinitely large real relative permittivity. It is reasonable, however, to ask at what points the induced dipole attains a large

value. Denoting $\varepsilon^p + 2$ with *e*, and the fraction $\frac{\varepsilon^p - 1}{\varepsilon^p + 2}$ with β, one finds that $\beta = 1 - \frac{3}{e}$. Further, allowing ε^p to be a complex number with a positive imaginary part, as would be the case for metals discussed in Chap. 3, $\mathrm{Im}[\varepsilon^p] = \mathrm{Im}[e]$. Denoting the imaginary part with *g* and the real part with *f*, the real and imaginary parts of β can be evaluated to be $\mathrm{Re}[\beta] = 1 - \frac{3f}{f^2 + g^2}$ and $\mathrm{Im}[\beta] = \frac{3g}{f^2 + g^2}$. Assuming e is a function of some parameter, say frequency ω, unless the functional forms of *g* and *f* are known, their values that optimize either $\mathrm{Re}[\beta]$ or $\mathrm{Im}[\beta]$ cannot be determined. However, if it is assumed that *g* and $g'(\omega)$ are relatively small compared to *f* and $f'(\omega)$—as would be the case for most high optical conductivity metals suitable for plasmonics applications that were discussed in Chap. 2—then it can be found that $|\mathrm{Re}[\beta]|$ is maximized when $f \to 0$ and $\mathrm{Im}[\beta]$, when $g \to 0$. $\mathrm{Re}[\beta] = -\frac{3}{f}$ near $g = 0$ and $\mathrm{Im}[\beta] = \frac{3}{g}$ near $f = 0$. Since g can never really be equal to zero, it is assumed that resonance occurs when $f = 0$ for materials with a relatively small values of $\frac{g}{f}$ and $\frac{g'(\omega)}{f'(\omega)}$, in which case, $\mathrm{Re}[\beta] = 1$. The location of the resonance in such materials can help develop several physical insights into their interaction with their surroundings. An obvious potential application could be in the area of detection through the observation of clear shifts or changes to resonance peaks. Consider that the sphere is embedded in a medium with a relatively constant relative permittivity ε^m. The resulting change in the location of the resonance in $S_1(\varepsilon^p)$ can be found using the procedure discussed above. It will occur when $f = 0$. However, since ε^p is normalized with respect to ε^m, $f = 0$ is equivalent to $\mathrm{Re}[\varepsilon^p] = -2\varepsilon^m$ and at resonance,

$\mathrm{Im}[\beta] = \varepsilon^m \frac{3}{g}$ and $\mathrm{Re}[\beta] = 1$. The effect of an optically dense medium is to not only shift the resonance peak toward larger negative values of $\mathrm{Re}[\varepsilon^p]$, but also to scale up the peak magnitude by a factor of ε^m.

Later in this section, the focus of interest is in studying the effects of the presence of a dielectric slab near a sphere. In the G_1 problem, this was studied by tracing of the location of $S_1(\varepsilon^p)$ peaks for $\varepsilon^p \equiv \mathrm{Re}[\varepsilon^p] + i\delta$. The parameter δ was chosen to be sufficiently small so that the resulting peak broadening was not significant enough to envelope the neighboring peaks. The substrate permittivity was chosen to be ε_S. The resulting problem can be analyzed analytically, especially in the G_1 condition since the multipole orders *m* equal zero. The following variables are defined for the ease of algebraic adjustments to Eq. 2.77: $\sigma_n \equiv -\frac{S_n^{th}}{\beta_n}$,

$t_{np} \equiv (-1)^{n+p} \frac{(n+p)!}{n!\,p!} d^{-(n+p+1)} \beta_S \beta_n$, $\beta_n \equiv \frac{n(\varepsilon_p - 1)}{n\varepsilon_p + n + 1}$ and $\beta_S \equiv \frac{\varepsilon_S - 1}{\varepsilon_S + 1}$. The multipole amplitudes of the thermal problem are given by:

$$\sigma_n = [\delta_{n1} + \sum_{p=1}^{\infty} t_{np}\sigma_p] \tag{4.12}$$

Upon noticing that the coefficients t_{np} have a $d^{-(n+p+1)}$ dependence, where $d \equiv 2h$ and h is the distance of the center of the sphere from the interface, it may make sense to expand σ_n in powers of d^{-1}. It can be shown that

$$\sigma_1 = 1 + t_{11} + t_{11}^2 + t_{12}t_{21} + t_{11}^3 + t_{13}t_{31} + O[d^{-11}]. \tag{4.13}$$

Similar expressions for σ_2, σ_3 etc. can be found. However, the current interest is focused toward evaluating the resonance conditions that require σ_n to be singular. Clearly, then, it can't be evaluated from a sum that contains several large positive and negative numbers that eventually add up to a large number. In order to evaluate the condition, say accurate upto $O[d^{-3}]$, one can write Eq. 4.12 as $(1-t_{11})\sigma_1 = t_{12}\sigma_2 + \ldots$ The last term is an $O[d^{-8}]$ term. It will be assumed to remain relatively small even when the coefficient t_{12} is relatively large. As a result, σ_1 can be allowed to be singular only as $(1-t_{11}) \to 0$. The condition can be put in a different form with more relevant quantities as follows:

$$\beta_1 = \frac{4h^3}{\beta_S}. \tag{4.14}$$

The condition can be further refined to include higher order terms by consequently subtracting out other σ_1 terms. So, $(1-t_{11}-t_{12}t_{21})\sigma_1 = O[d^{-9}]$ etc. would result in the condition given by $(1-t_{11}-t_{12}t_{21}) \to 0$ and in more relevant terms,

$$\beta_1 = \frac{4h^3}{\beta_S}\left(1+\frac{9}{64h^5}\beta_2\beta_S\right)^{-1} \tag{4.15}$$

and so on. For large enough values of h, the condition $\beta_1 \to \infty$ can be recovered. The series expansions for σ_n, especially for the G_1 problem, suffers from slow convergence as $h \to 1^+$ since all terms in the series become potentially important when $\beta_S \to 1$ or, alternatively, $\varepsilon_S \to \pm\infty$. Consider a case when $\varepsilon_p = \varepsilon_S = 10^6$. Converged answer accurate upto 4 decimal places requires

the use of increasingly larger number of harmonics as the gap $g \equiv h-1$ is made to approach zero. Fig. 4.2 shows the behavior of the minimum required multipole harmonics N_4 for a four decimal place accuracy as the function of increasing $-\log_{10} g$. The convergence of S_1 with respect to the number of harmonics N for a given *g* was, almost always, monotonically reducing function that asymptotically converged to a constant S_1 value. Reducing *g* sifted the point of convergence, within a defined neighborhood, to larger and larger values of N_4. The maximum value of $-\log_{10} g$ in Fig. 4.2 corresponds to $-\log_{10} g \approx 2.4$ or $h = 1.002,$ after which, the values of N_4 exceed 85. After $N = 85$, the matrix condition number of the coefficient matrix reduces to a value lower than the machine precision for MATLAB, which is approximately 10^{-16}.

In order to circumvent the difficulty with the convergence, a nonlinear sequence acceleration transform, called the Shanks transformation, was used. For a sequence of S_1 values corresponding to a given N denoted $S_{1,N}$, one iteration of Shanks transform is equivalent to the following operation on S_{1N}:

$$Sh(S_{1,N}) = \frac{S_{1,N+1}S_{1,N-1} - S_{1,N}^2}{S_{1,N+1} - 2S_{1,N1} + S_{,1N-1}}, \tag{4.15}$$

where *Sh* denotes the transformation operator. The resulting sequence has $\frac{1}{2}(N_m + 1)$ terms if N_m denotes the maximum value of the count N which is assume to be an odd number. The

expected converged answer is found to be given by $Sh^{\nu_m}(S_{1N})$ with $\nu_m \equiv \frac{1}{2}(N_m - 1)$. Further, the iterations can be represented by the count $\nu \equiv \frac{1}{2}(N - 1)$.

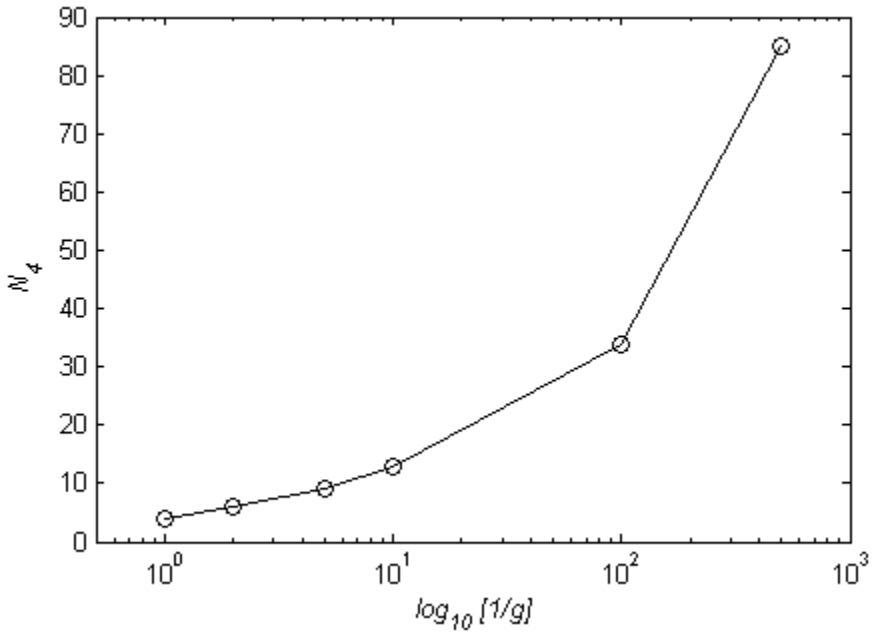

Figure 4.2: Minimum number of Laplace multipoles required to achieve a 4 decimal point convergence in the calculated value of the dipole amplitude. Maximum number of multipoles after which calculations cannot be performed was found to be 85. The largest value on the x-axis corresponds to a height h = 1.001, the required number of multipoles for which exceed 85.

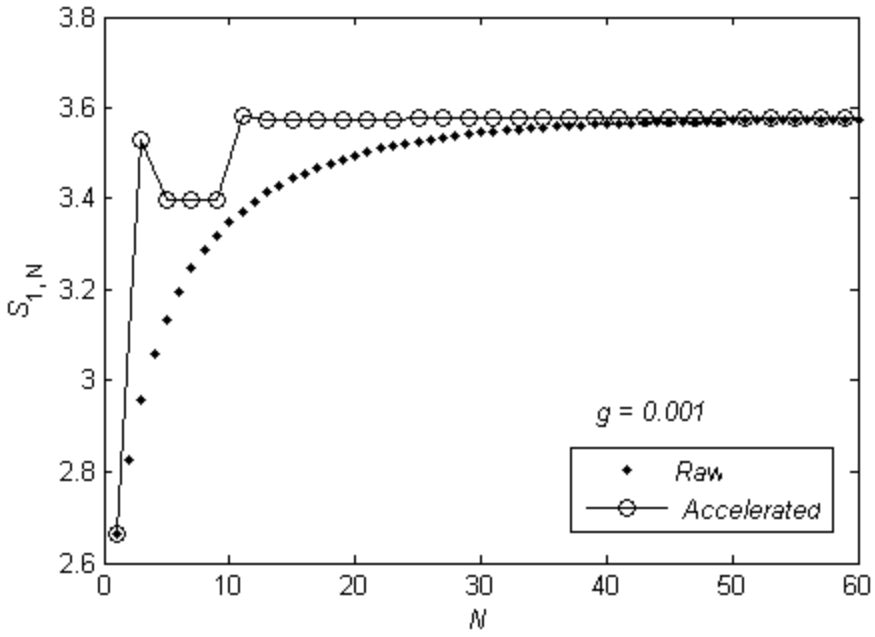

Figure 4.3: A comparison between the sequences of dipole amplitudes obtained with (circles) and without (dots) the application of Shanks transformations for $h = 1.001$. The N_4 point (defined in the preceding text) for the raw data is larger than 85 but the transformed values have $N_4 = 39$—a reduction by at least a factor of 2.

Fig. 4.3 shows the improvement in convergence that can be achieved by the application of Shanks transformation for a situation when $h = 1.001$. Shanks transform converged values of the induced dipole moment can be evaluated for upto 4 decimal places for only upto $h = 1.001$ to give a value of 3.5765. For values of h that are even smaller, $S_{1,N}$ does not seem to converge even after $N = 85$. The values, however, seem to increase and remain finite. As $g \to 0$, one finds that the last iteration exceed a value of 4.00 when g is reduced below a value of 0.0001. If β_1 and β_S are set to equal one, $S_{1,N}$ is, perhaps, expected to converge very slowly as $g \to 0$. The exact details of convergence are not of interest with respect to the current work.

Fig. 4.4 shows the calculated critical values of $\mathrm{Re}[\varepsilon_p]$, $\mathrm{Re}[\varepsilon_{pc}]$ for which a dipole, quadruple and octupole resonance occurs in S_1 for $\beta_S = 1$. The locations of $\mathrm{Re}[\varepsilon_{pc}]$ were calculated by tracing the peaks in $\mathrm{Im}[S_1]$ vs. $\mathrm{Re}[\varepsilon_p]$ curves for increasingly smaller values of g. The imaginary part of ε_p was chosen to be 0.001 for all calculations, except for some parts of quadrupole and octupole calculations for which, the values were increased to 0.01 followed by 0.1 to suppress numerical oscillations without changing the peak location. The assumption is valid from the point of view of a preceding discussion, in which, it was showed that as long as $\frac{d\,\mathrm{Im}[\varepsilon_p]}{d\,\mathrm{Re}[\varepsilon_p]} = 0$ and $\frac{\mathrm{Im}[\varepsilon_p]}{\mathrm{Re}[\varepsilon_p]} \to 0$, the overall effect on the calculated $\mathrm{Im}[S_1]$ values is to only broaden the peak and reduce its amplitude while maintaining the peak location. A similar calculation can be performed for higher order multipole amplitudes S_n with $n > 1$ to give the correspongding multipolar coupling effects. The induced dipole mode amplitude S_1 is the most relevant since it is the only mode that that is radiative—eventhough it can be argued that the near field coupling, that is significant at relatively small values of *g*, has several coupled resonances that may dictate how strongly the near-field couples to the substrate. It is observed that multipole peaks for all S_n are located at the same value of $\mathrm{Re}[\varepsilon_{pc}]$. The observation can be explained by looking at the fact that $S_n = -\beta_n \delta_{n1} + \sum_{m=1}^{\infty} T_{nm} S_m$, because of which, all S_n need to be singular simultaneously—making it only necessary of study one type of S_n for the purpose of locating critical values $\mathrm{Re}[\varepsilon_{pc}]$.

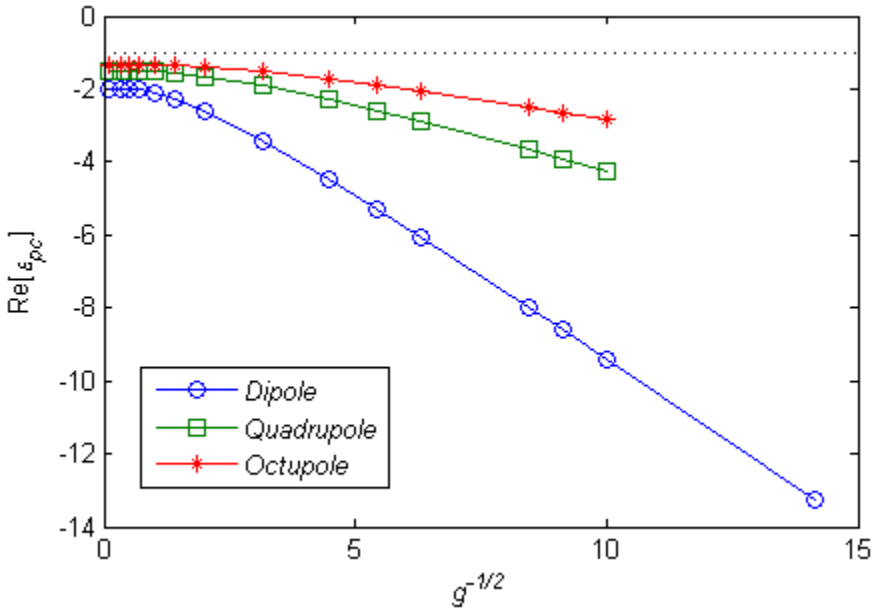

Figure 4.4: The critical values of the sphere's permittivity for which the first three peaks were observed in the value of –Im[S_1]. The peaks correspond to the dipolar, quardupolar and octupolar coupling with the substrate which is chose to have a $\varepsilon_S = 10^6$. The locations were found to asymptotically depend on $g^{-1/2}$. The x-axis is, hence, chosen to represent $g^{-1/2}$. For relatively large values of g, dipolar resonance occurs at –2, quadrupolar at –3/2 and octupolar at –4/3. As $g \to 0$, the peak locations shift to large negative values. The dotted line represents the n^{th} multipolar peak location for $n \to \infty$—the upper bound Re[ε_{pc}] = –1. The relative separation between locations is larger for a lower value of n. The dipolar resonance is the most shifted under stronger coupling.

An example of the various peaks present in the $\mathrm{Im}[S_1]$ vs. $\mathrm{Re}[\varepsilon_p]$ curve is shown in Fig. 4.5. In order to capture the octupolar resonance peak, it was necessary to use a relatively larger value of $\mathrm{Im}[\varepsilon_p]$, 0.1, for Fig. 4.5. The corresponding $\mathrm{Re}[S_1]$ values are shown in Fig. 4.6. The inflection points correspond to the peaks in the imaginary part. The dipolar peak can is located at the farthest negative value and is most prominent. In a Drude permittivity material, as discussed in Chap. 3, a larger negative value corresponds to a relatively large wavelength that lies in the red- region of the spectrum. The quadrupolar and octupolar resonances occur at relatively smaller negative values and are relatively diminished.

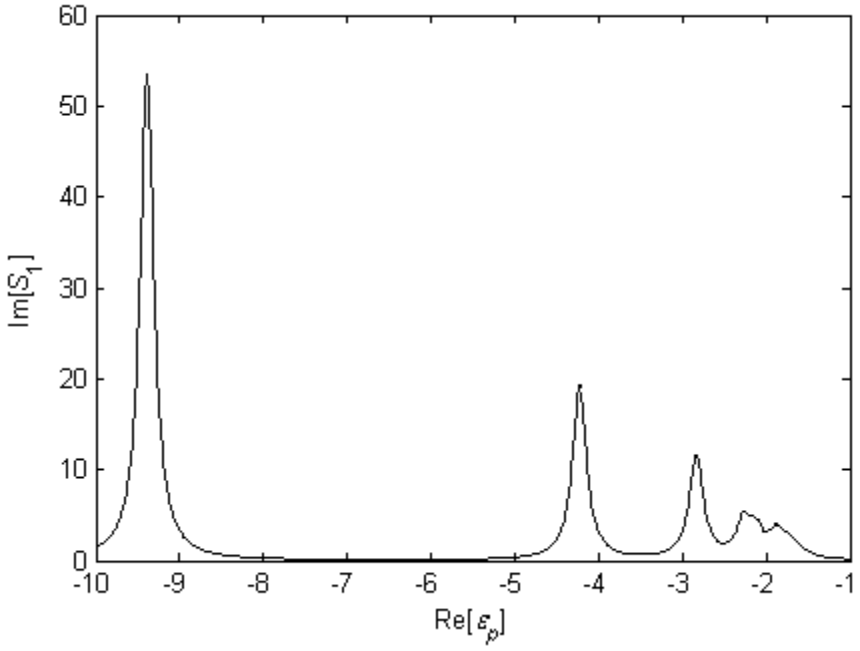

Figure 4.5: Dipolar, Quadrupolar and Octupolar resonance peaks in the imaginary part of the induced dipolar amplitude. The gap has a value of $g = 0.01$. The dipolar coupling results in the most prominent peak that is left-most. It is followed by higher mulipolar peaks. The right-most peaks are a mix of several higher order multipolar peaks that are packed in a narrow region.

The gap g has an effect of shifting the peaks. In the limit as $g \to \infty$, the dipolar peak moves back to -2 and the other peaks become subdued and, eventually, disappear. In the opposite situation, when $g \to 0$, leads to the emergence of the peaks from near -1 followed by a shift towards the right—all the way upto -∞. In terms of the wavelength, there is an infinite red-shift in the location before disappearance. The peaks, however, become sharper as they shift away—requiring relatively large values of $\mathrm{Im}[\varepsilon_p]$ for, both, peak resolution and the convergence of the calculation. The real part corresponding to the curve in Fig. 4.5 is given in Fig. 4.6. It also shows features that are inflection points rather than peaks, at the locations where there are peaks in the imaginary part. $|S_1|$ undergoes a resonance, just like $\mathrm{Im}[S_1]$, but at the inflection point, the phase angle changes by an amount given by π. Overall, the induced dipole is at maximum at resonance.

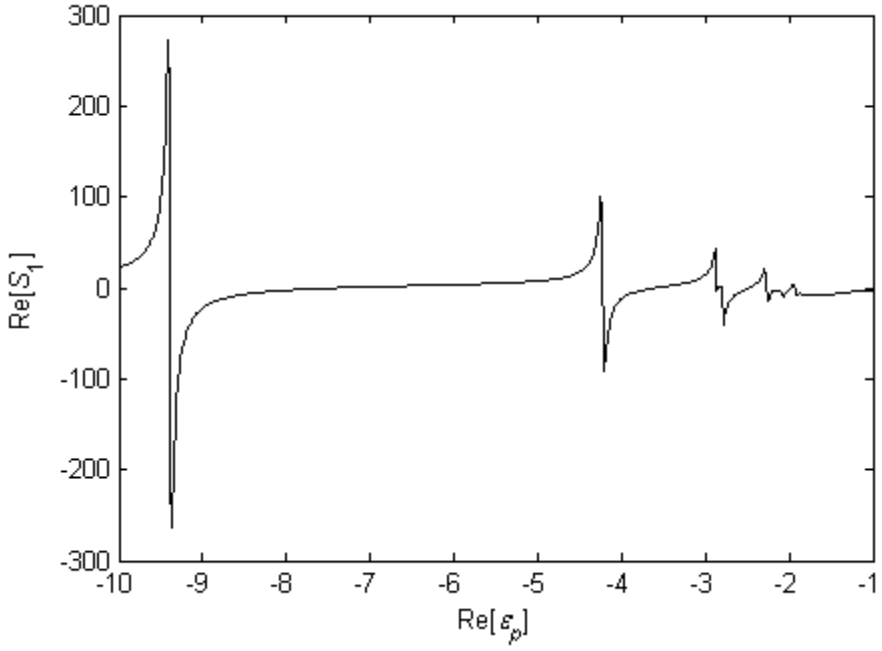

Figure 4.6: The real part of the induced dipole for $g = 0.01$ and $\mathrm{Im}[\varepsilon_p] = 0.1$. Inflection points mark the location of the resonance. $|S_1|$ undergoes a resonance, just like $\mathrm{Im}[S_1]$, but at the peak point, the phase angle changes by an amount given by π.

For infinitesimally small values of *g*, when all discernible peaks have shifted far away to large negative values, a continuum seems to appear near $\mathrm{Re}[\varepsilon_p] = 0$. As shown in Fig. 4.7, the peaks are missing even for a relatively large range of $\mathrm{Re}[\varepsilon_p]$. A relatively large value of $\mathrm{Im}[\varepsilon_p] = 2$ was required so that converged results could be obtained, however, the trend seemed to be consistent with that observed for a case when $\mathrm{Im}[\varepsilon_p]$ was chosen to be much smaller. As $\mathrm{Im}[\varepsilon_p] \to 0$, the peak location seemed to shift toward −2 and the value seemed to increase asymptotically to ~10. In a similar manner, the $\mathrm{Re}[S_1]$ curve seemed to show a relatively large magnitude negative peak that was located at ~−1.6 and had a magnitude that approached ~−10.

However, unlike $\mathrm{Im}[S_1]$, the peak value approached its asymptotic value after going through a maximum in the magnitude.

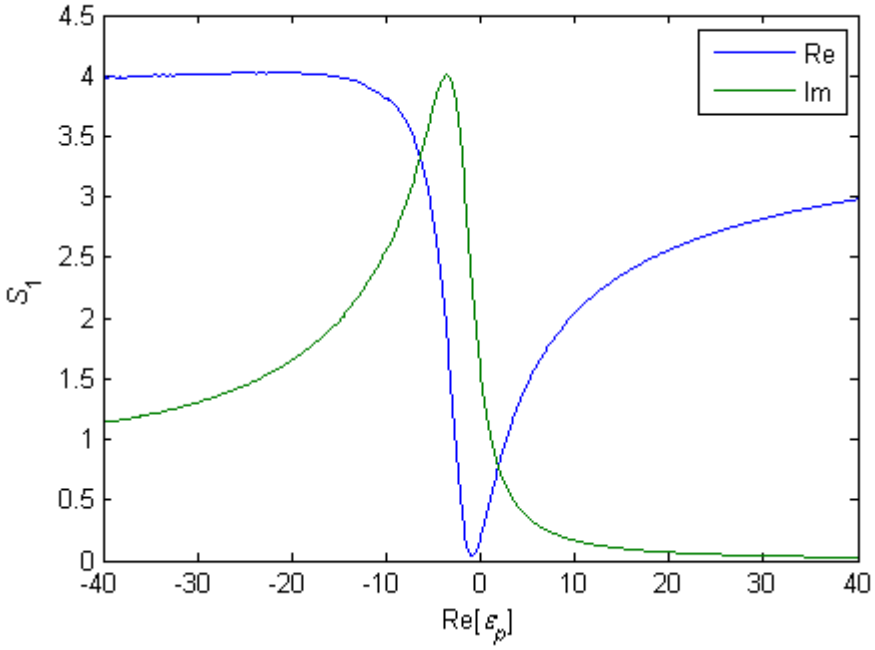

Figure 4.7: The real and imaginary parts of the induced dipole for a sphere that is touching ($g = 0$) an interface that has a permittivity given by $\varepsilon_S = 10^6$. Instead of several peaks, a continuum that is asymmetric with respect to a peak at ~−3.5 is observed for $\mathrm{Im}[S_1]$. A more subdued inflection that resembles a peak at ~ −0.9 is observed for $\mathrm{Re}[S_1]$. In order to get converged results, it was necessary to use a relatively large value of $\mathrm{Im}[\varepsilon_p] = 2$.

The trend of "peak disappearance" seems to remain valid even for materials with an ideal Drude permittivity that were discussed in Chap. 3, Figs. 3.7 and 3.8. The Drude permittivity as a function of wavelength is a monotonous map, although a nonlinear one. Hence, all shape features that appear for a linear map of the real part and a fixed imaginary part are present in the case of a Drude permittivity metal.

Substrate permittivity ε_S dependent β_S value affects the dipole resonance locations by shifting the locations not only toward negative values of $\mathrm{Re}[\varepsilon_{pc}]$, but also positive values. As shown in Fig. 4.8, there seems to be a resonance in the resonant values as a function of β_S with the critical value $\beta_{Sc} \approx 1.284$ for a given value of g = 0.1. Near the singular point, the critical values $\mathrm{Re}[\varepsilon_{pc}]$ reach large positive and negative values followed by an asymptotic behavior toward finite values. As β_S is allowed to increase from 0, the dipolar peak tends to moves toward negative infinity from a finite negative value. After passing the critical value β_{Sc}, the peak reappears from positive infinity followed by a shift asymptotically toward a finite positive value. The asymptotic value and the value of β_{Sc} are g dependent—they would change as g is allowed to assume different values. In general, β_S is a complex number, which would require studying its behavior over not just positive real values, but also, negative real and positive and negative imaginary values. It seems sufficient to only analyze real positive values since real substrate materials have a permittivity ε_S that can assume any real value but only a small positive imaginary value. Away from a singular point in $\beta_S(\varepsilon_S)$ and $-1 < \mathrm{Re}[\varepsilon_S] < 1$, it can be seen that $\mathrm{Re}[\beta_S] > 0$ and that $\mathrm{Im}[\beta_S]$ remains relatively small. The conditions are satisfied by most materials except certain metals that have a permittivity that satisfies $-1 < \mathrm{Re}[\varepsilon_S] < 1$ for the wavelength range of interest. The presence of a relatively small $\mathrm{Im}[\beta_S]$ is expected to shift the locations of β_{Sc} and the asymptotic value for $\mathrm{Re}[\beta_S] \to \infty$. The singularity in β_S corresponds to a substrate permittivity $\varepsilon_S \approx -8.042$—a value that can be realistically achieved by high optical conductivity metals such as Ag and Au in the visible range of wavelengths. Essentially, metal nanoparticles in the vicinity of metallic substrates can have dipole resonances that can be

significantly shifted in not only the large wavelength direction, but also toward relatively smaller wavelengths.

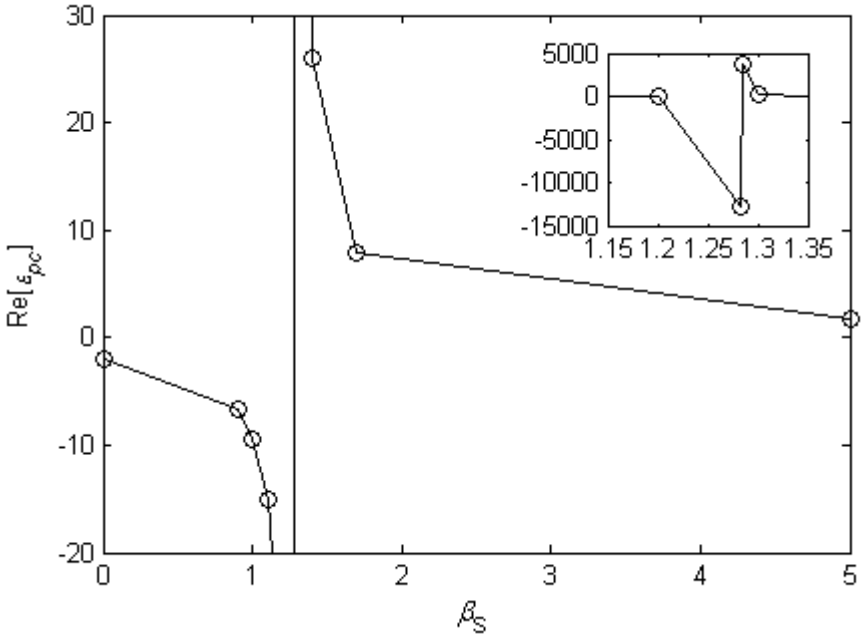

Figure 4.8: The behavior of peak locations for dipolar resonance in S_1 as a function of the substrate parameter β_S for a gap given by g = 0.01. The imaginary part Im[ε_p] as set to equal 0.001. A singularity is observed for $\beta_S \approx 1.284$. The peak locations span large positive and imaginary values followed by an asymptotic behavior toward a finite positive Re[ε_{pc}] that is close to 1.

Metals such as Ag, Au and Cu have a small enough imaginary part of permittivity that allows them to exhibit a peak value in the induced dipole moment. Out of them, Ag has the least value of $\mathrm{Im}[\varepsilon]$ that allows it to show a relatively large peak value as well as a narrower peak width. The peak location, as discussed in this section, is dependent on the gap distance g. The resulting shift in the peaks is in the direction of increasing λ. Figs. 4.9 and 4.10 show the effect of g on S_1 for a sphere made of a Drude metal that has a plasma wavelength $\lambda_p = 290$ nm and

collision energy $E_C = 0.1$ eV. The value of λ_p is such that the plasmon resonance for an isolated sphere occurs at $\lambda_R \approx 500$ nm. The collision energy is chosen so that the imaginary part $\mathrm{Im}[\varepsilon_p]$ remains *O*[0.1] resulting in a significantly sharp peak. As the sphere is made to approach the interface, several artifacts that result from the coupling effects are observed.

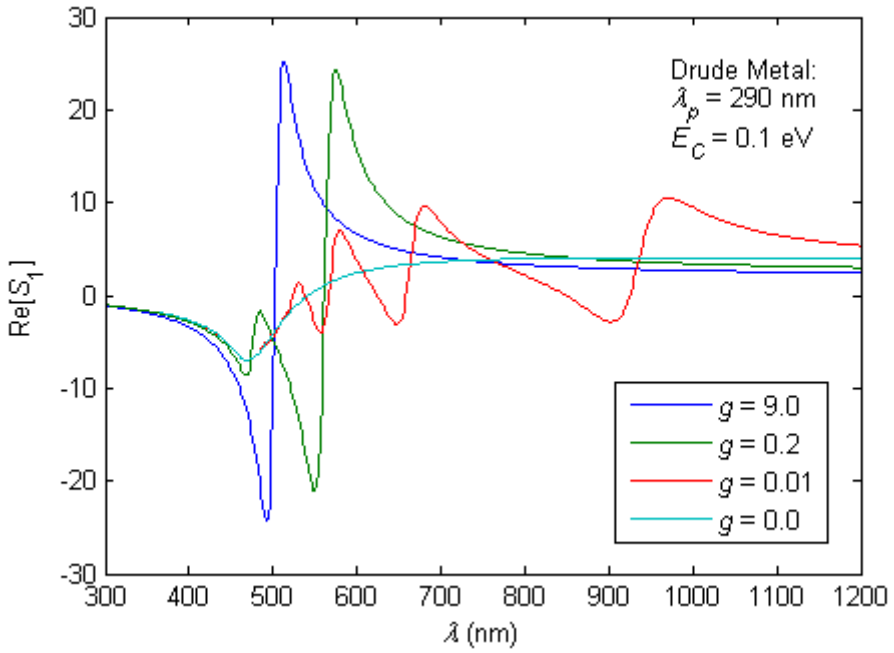

Figure 4.9:.Re[S_1] for g values including g = 0. The sphere is assumed to be made of a metal that has a Drude permittivity with a characteristic plasma wavelength λ_p = 290 nm and a collision energy E_C = 0.1 eV. The substrate has a β_S = 1.

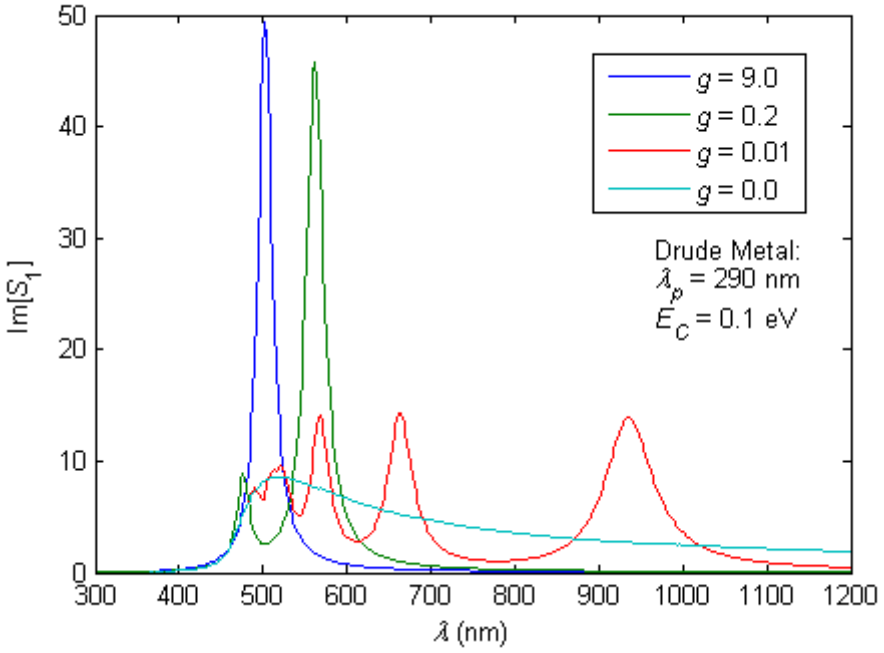

Figure 4.10: Im[S_1] for g values including $g = 0$. The sphere is assumed to be made of a metal that has a Drude permittivity with a characteristic plasma wavelength $\lambda_p = 290$ nm and a collision energy $E_C = 0.1$ eV. The substrate has a $\beta_S = 1$.

The peak features in $\mathrm{Im}[S_1]$ are easier to describe in comparison to the inflection features in $\mathrm{Re}[S_1]$. In Fig. 4.10, one can see the following events as g is made to approach zero: (i) peak shift, (ii) peak birth and (iii) peak disappearance. The corresponding artifacts in fig. 4.9 are with regard to the location, the relative intensity and the relative width of the inflection features. The general form of the peak and the corresponding real part are a characteristic of an isolated sphere made of a Drude metal that corresponds to a Lorentzian response [2]. The presence of coupling seems to want to distort the response [2]. For g values of $O[0.01]$, several peaks are observed, up to $n = 4$ coupling peaks are seen in Fig. 4.10. As the g value is reduced further, the peaks seem to want to disappear and give rise to a continuum as discussed previously in this section. The most interesting feature of the continuum is the complete absence of peaks.

In more relevant systems that consist of either Ag, Au or Cu nanospheres distributed on a substrate made of silicon or materials that have a similar dielectric function as silicon, the calculation of the G_1 dipole can be performed in a similar manner to those discussed previously. Since Ag, Au and Cu significantly resemble Drudian permittivity (see Figs. 3.1, 3.2 and 3.3), their interaction with a relatively high permittivity substrate such as Si can be expected to show trends that are similar to those seen Figs. 4.9 and 4.10—all features including peak shift, birth and disappearance, and the eventual peak-less continuum. However, as a result of the relatively larger collision energy E_C of Ag, Au and Cu, one can expect all the features to occur but with relatively smaller peak values, peaks shift and birth rates with respect to *g*. The peak features are expected to be most prominent for a situation in which $E_C \to 0$. Figs. 4.11- 4.16, show converged results for Ag, Au and Cu nanospheres on an infinitely thick Si substrate. The real and imaginary parts of the induced dipole moment S_1 for several values of the gap *g* are shown.

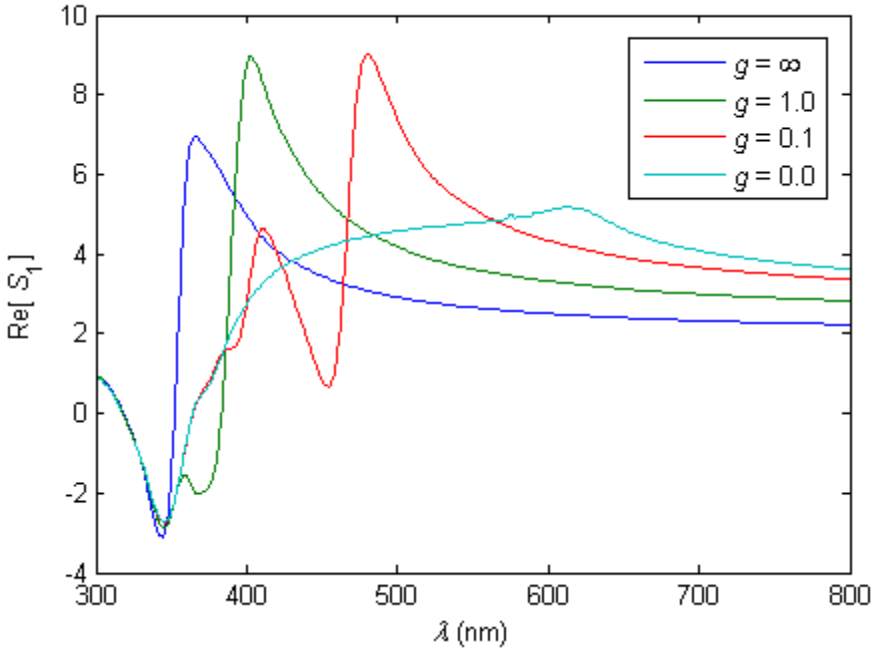

Figure 4.11: Re[S_1] for g values including $g = 0$ for an Ag sphere present near a semi-infinite Si substrate.

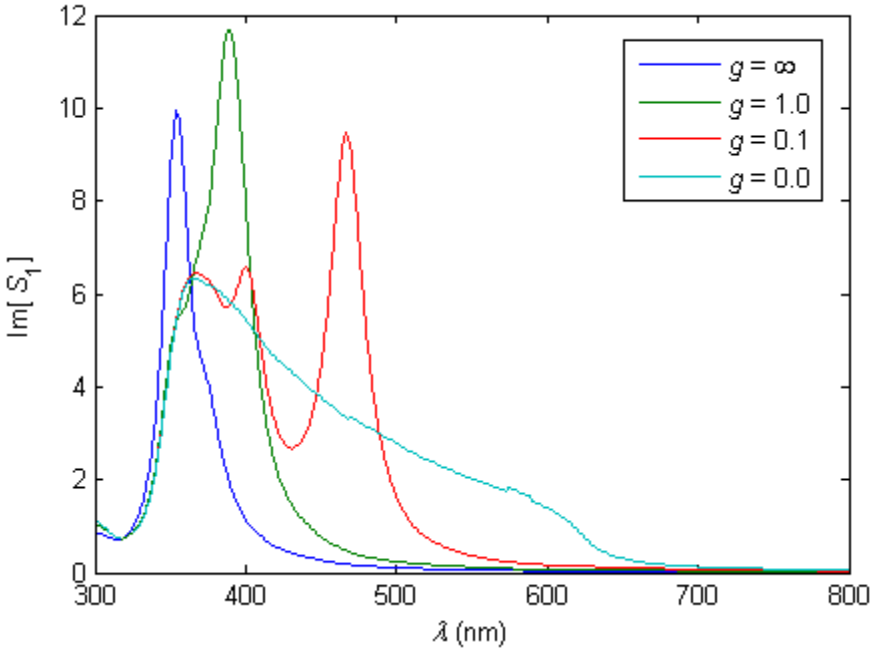

Figure 4.12: Im[S_1] for g values including $g = 0$ for an Ag sphere present near a semi-infinite Si substrate. The dipole corresponds to the G_1 problem. The peaks show (i) shift toward a larger λ, (ii) birth near ~350 nm and (iii) disappearance after a shift of ~300 nm.

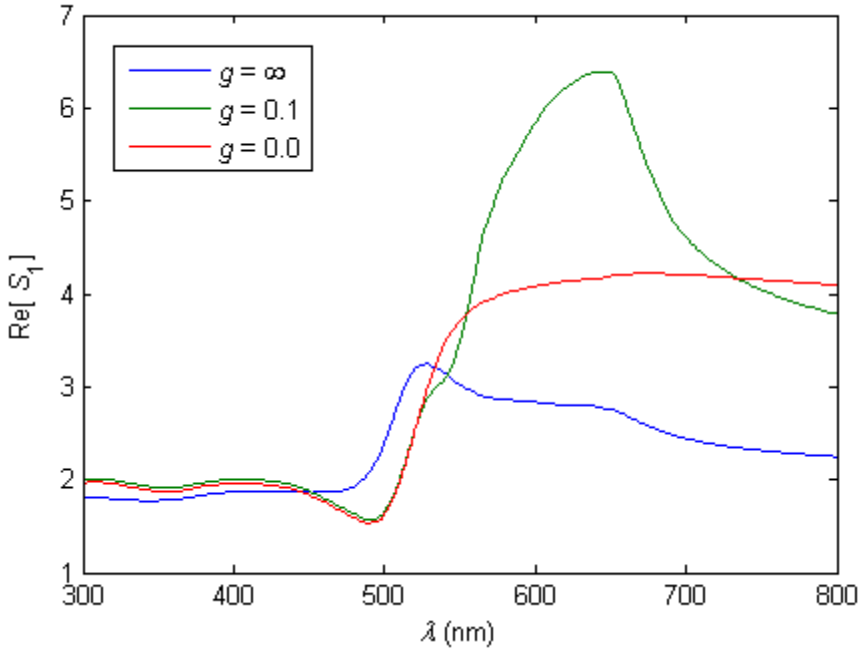

Figure 4.13: Re[S_1] for g values including g = 0 for an Au sphere present near a semi-infinite Si substrate.

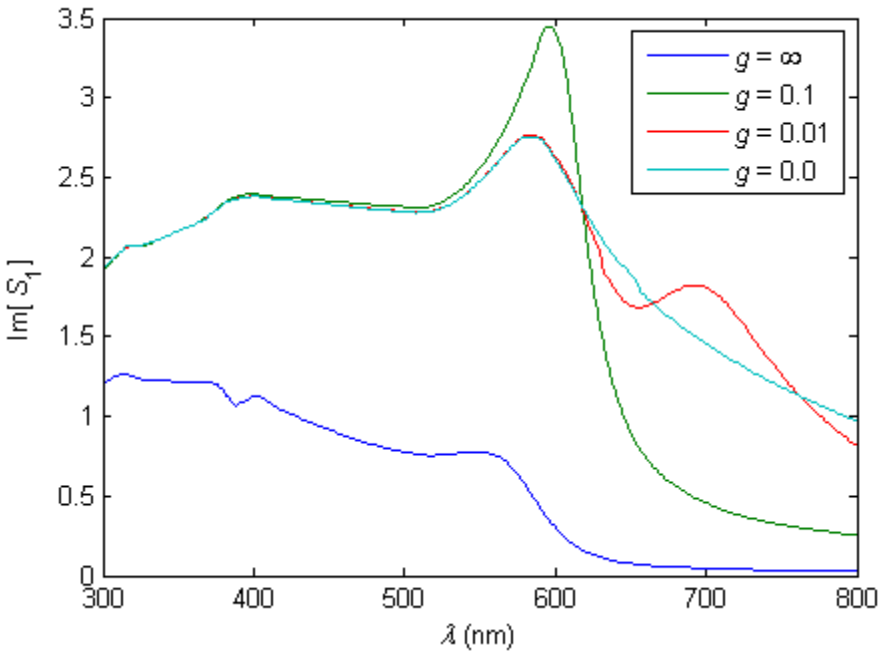

Figure 4.14: Im[S_1] for g values including g = 0 for an Au sphere present near a semi-infinite Si substrate. The peaks show (i) a relatively smaller shift toward a larger λ, (ii) birth near ~600 nm and (iii) disappearance after a λ value that is larger than 800 nm.

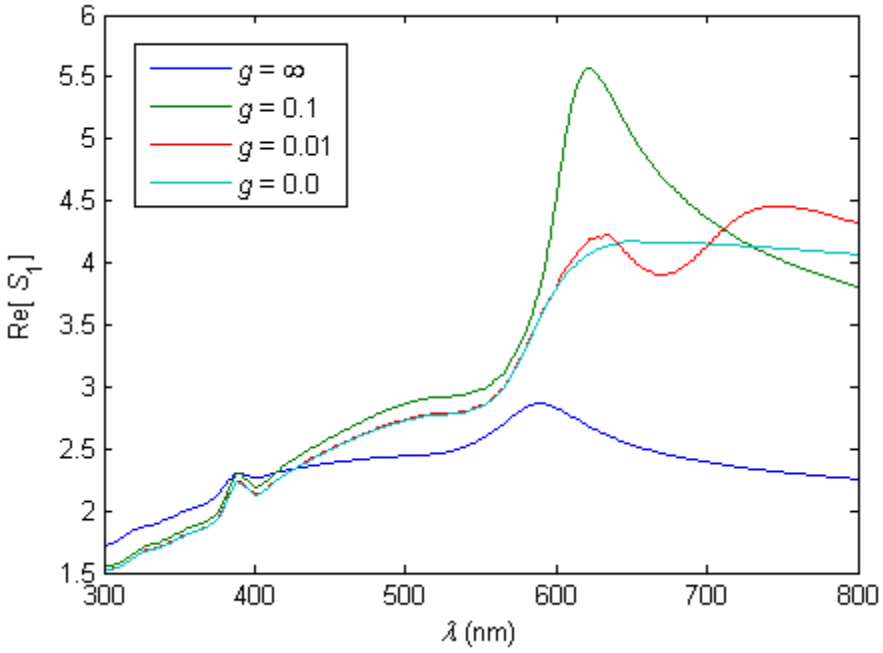

Figure 4.15: Re[S_1] for g values including g = 0 for a Cu sphere present near a semi-infinite Si substrate.

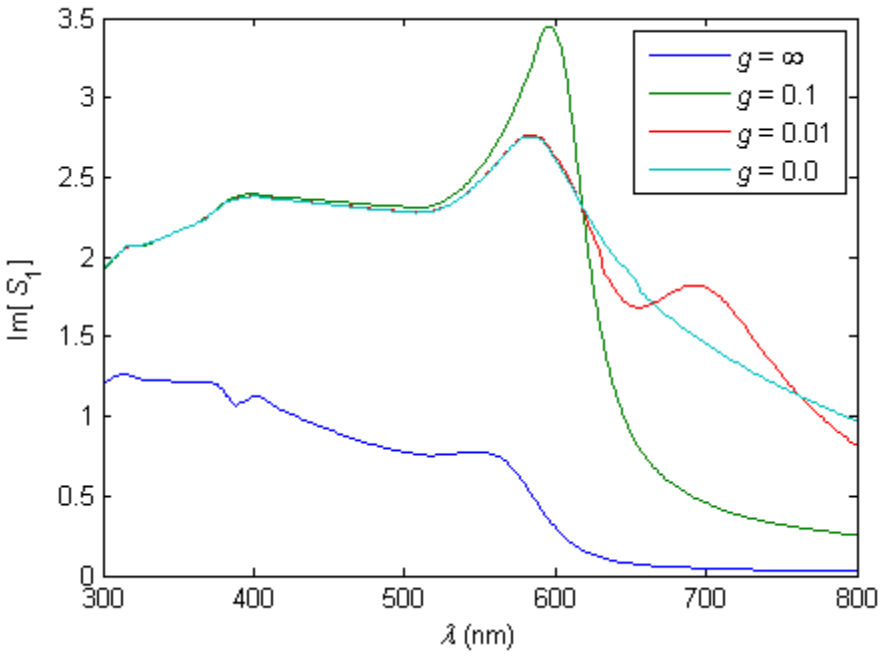

Figure 4.16: Im[S_1] for g values including g = 0 for an Cu sphere present near a semi-infinite Si substrate. The peaks show (i) a relatively smaller shift toward a larger λ, (ii) birth near ~600 nm and (iii) disappearance after a λ value that is larger than 800 nm.

An Ag nanosphere present near an Si substrate leads to an induced dipole behavior that resembles that obtained for a Drudian metal with a relatively low E_C present in the vicinity of substrate with a relatively large wavelength independent permittivity. Au and Cu deviate from the expected behavior due to their relatively large values of E_C and the fact they both require, at least, one Lorentz oscillator to model them accurately. The presence of the non-Drude-like features leads to a relatively indistinct peak shift and the presence of relatively broad peaks in Au and Cu systems. As a result, the overall value of the induced dipole increases in magnitude as an Au or Cu sphere approaches a Si substrate. The effect of peak shift is eclipsed by the relatively broad spectrum. Moreover, a g-resonance occurs for a fixed value of λ. Such a resonance occurs even for the Ag-Si system, but it can be interpreted to result from the shifts in the peak locations

and the change in their relative width rather than to arise from a non-monotonic increase in the overall value of the induced dipole. The overall resonant response of an Au or Cu sphere seems to enhanced by a factor that varies non-monotonically with *g*—assuming a maximum value of ~4 for Au and ~2.5 for Cu.

4.2.2 The G_2 problem

In the presence of a horizontally oriented thermal gradient G_2, one would expect the induced dipole and higher order multipoles to be oriented parallel to the applied field. The degree of the induced multipoles has to reflect the direction by allowing non-zero values of *m*, specifically, $m = \pm 1$ multipoles that correspond to the horizontal orientation. In a manner similar to that discussed in the preceding section, an analytical expression for the induced multipole moments can be derived in the form of an implicit series that can be represented as a matrix. One can use Eq. 2.77 for the two values of *m* in the following way. For $m = 1,$ the equation is given by $S_n^+ + \beta_n \sum_p T_{np}^+ S_p^+ = \beta_n \delta_{n1}$ and for $m = -1,$ it is $S_n^- + \beta_n \sum_p T_{np}^- S_p^- = -\frac{1}{2}\beta_n \delta_{n1}$. The singular coefficients S_{nm}^{th} are re-labeled with superscripts that correspond to the two different values of $\mathrm{sgn(m)}$. The coefficients $T_{np}^{\pm}$ are unrelated due to the fact that the associated Legendre polynomials $P_{n,\pm 2}(1)$ are equal to zero and as a result, all the degrees have to be equal in values—either $+1$ or -1. Further, the equations can be put in the same form as in the previous section—$\sigma_n^{\pm} = [\delta_{n1} + \sum_{p=1}^{\infty} t_{np}^{\pm} \sigma_p^{\pm}]$—with the substitution of the following variables: $\sigma_n^+ \equiv \frac{S_n^+}{\beta_n}$, $\sigma_n^- \equiv -2\frac{S_n^-}{\beta_n}$,

$\beta_n \equiv \dfrac{n(\varepsilon_p - 1)}{n\varepsilon_p + n + 1}$, $\beta_S \equiv \dfrac{\varepsilon_S - 1}{\varepsilon_S + 1}$ and $t_{np}^{\pm} \equiv (-1)^{n+p} \dfrac{(n+p)!}{(n \pm 1)!(p \mp 1)!} d^{-(n+p+1)} \beta_n \beta_S$. The singular coefficients can then be evaluated in the manner discussed in the previous section. Since the algebraic framework is made same as that for the G_1 problem, the series corresponding to σ_1 in the previous section (Eq. 4.13) can be used here with some adjustments.

$$\sigma_1^{\pm} = 1 + t_{11}^{\pm} + t_{11}^{2\pm} + t_{12}^{\pm} t_{21}^{\pm} + t_{11}^{3\pm} + t_{13}^{\pm} t_{31}^{\pm} + O[d^{-11}]. \tag{4.16}$$

The least value that the parameter *d* can take is 2, which represents the touching condition. The singular values of $\sigma_1^{\pm}$ for the case when $d \to \infty$ occurs when β_1 is singular. However, to a first approximation, the resonance condition gets modified when as *d* is made to approach 2 to $(1 - t_{11}^{\pm}) \to 0$ as in the case of the G_1 situation. This condition, in general, represents two separate conditions for the G_2 situation. However, since, the coefficients $t_{11}^{\pm}$ are identical and given by $t_{11}^{\pm} = d^{-3} \beta_n \beta_S$, the conditions become unique. Since $d = 2h$, the following condition can be derived for dipolar resonance in the G_2 situation:

$$\beta_1 = \frac{8h^3}{\beta_S}. \tag{4.17}$$

In comparison to the corresponding condition for the G_1 problem, the condition given in Eq. 4.17 has a right-hand-side that is twice in value. The resulting resonance can occur for smaller values of sphere permittivity ε_p for given values of *h* and β_S. In case of Drudian metals such as Ag, a consequence is resonance peaks that are relatively less red-shifted in comparison to the peaks in

the G_1 problem. Addition of a higher order term can lead to the following expression for the resonance condition given by

$$\beta_1 = \frac{8h^3}{\beta_S}\left[1+\frac{3\beta_2\beta_S}{32h^5}\right]^{-1} \tag{4.18}$$

which can be derived by setting equal the following condition which is similar to the one that was derived in the preceding section: $(1-t_{11}^{\pm}-t_{12}^{\pm}t_{21}^{\pm})\to 0.$ As seen before, the refined resonance condition also contains terms that lead to relatively smaller corrections to Eq. 4.16. Overall, the value of dipole polarizability β_1 remains relatively larger for the G_2 problem. The peak shifts are expected to be less prominent as a result.

The calculated values of the induced dipole as the gap distance $g \to 0$ do not suffer form any difficulties related to convergence unlike the G_1 problem. When the sphere's permittivity is set to equal 10^6 and substrate parameter $\beta_S = 1$, for a gap distance $g = 1.001$, one finds that the number of harmonics required to achieve a four decimal point convergence is $N_4 = 45$ multipoles—significantly lower in comparison to $N_4 > 85$ for the corresponding G_1 problem. Not surprisingly, any acceleration leads only to a much faster convergence.

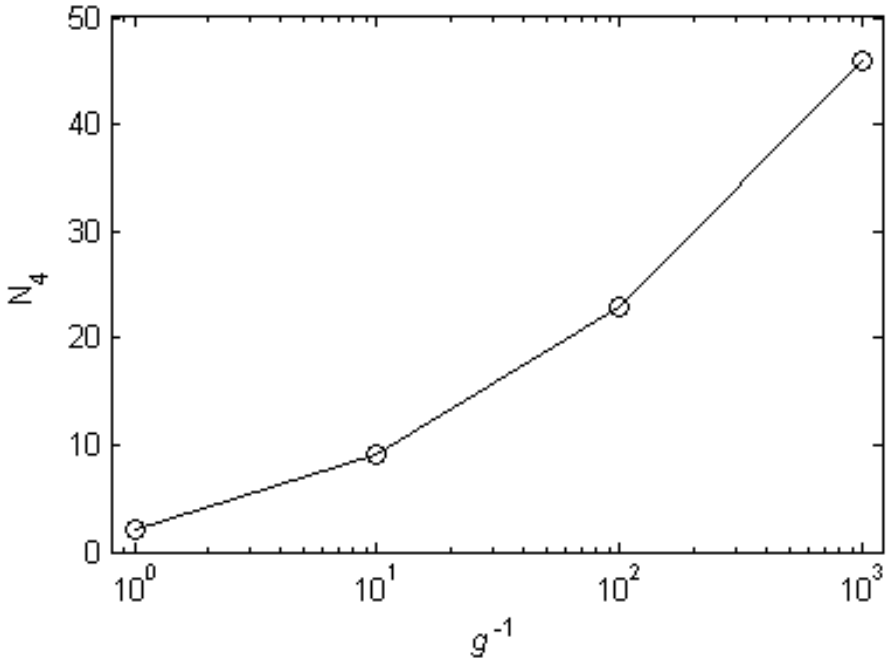

Figure 4.17: Number of iterations required to achieve a four decimal point convergence for the G_2 problem. The sphere permittivity is $\varepsilon_p = 10^6$ and substrate parameter is $\beta_S = 1$. Unlike the G_1 problem, the N_4 values are much smaller. For $g = 0.001$, $N_4 = 46$—a value that is less than the maximum number of multipoles $N_{max} = 85$ that can be used for the calculations.

The convergence rates only seem to reduce monotonically as $g \to 0$ for both problems. In addition, the inability to converge for $\varepsilon_p = 10^6$ and $\beta_S = 1$ was, in some sense, correlated to the convergence related difficulties for the resonance analysis when $\mathrm{Re}[\varepsilon_p] < 0.$ One would expect that in the current problem, there shouldn't be any convergence related difficulties when analyzing situations where the sphere's permittivity is allowed to take negative real and positive imaginary values. Convergence, however, is not achieved for all values of $\mathrm{Im}[\varepsilon_p]$ for $g \le 0.001$. Convergence can be forced just like in the G_1 problem by increasing the value of $\mathrm{Im}[\varepsilon_p]$ to a larger value.

The locations of the resonances peaks in $\mathrm{Im}[S_{11}]$ were evaluated in a manner similar to the one used previously. The shift in the location was found to be very small in comparison to G_1. Only dipole resonance peaks were traced since quadrupole and higher order peak locations were found to maintain their positional order under both kinds of excitations. The resonance shifts for the dipolar contributions to the induced dipole S_{11} for G_1 are given in Fig. 4.18.

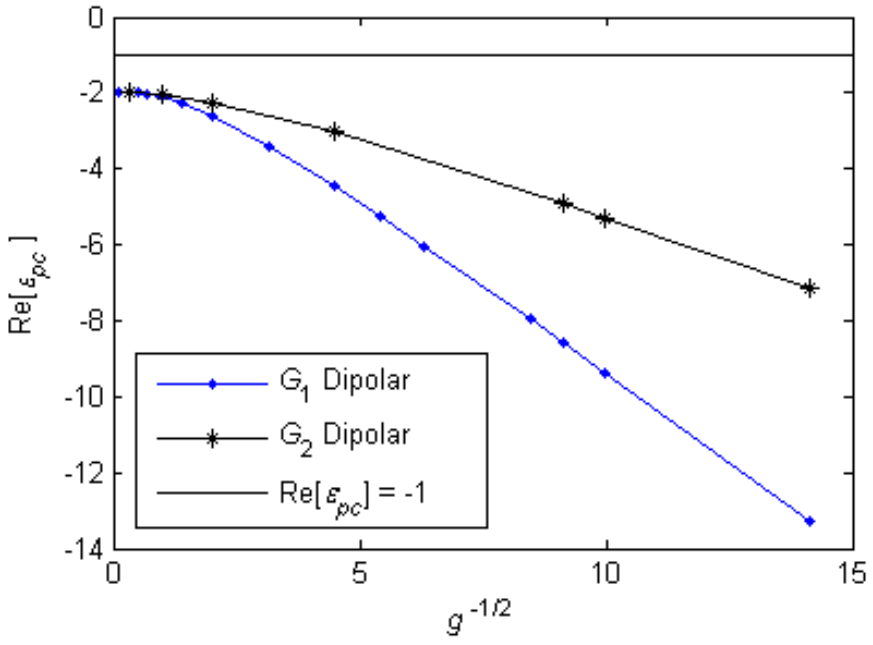

Figure 4.18: Locations of resonance peaks correspoinding to the dipolar contibutions to the induced dipoles for the G_1 and G_2 type excitations. The induced modes are S_{10} for the G_1 problem and S_{11} and $S_{1,-1}$ for the G_2 problem. Here, the values of S_{10} and $S_{1,-1}$ were used for locating the resonance peaks. The G_2 peaks shifts are approximately close to half of the G_1 shifts as the gap is made to approach smaller values. Contributions from higher order multipolar couplings are not discussed here since, they maintain their positional order as well as their asymptotic behaviors in the limit as $g \rightarrow 0$. They are expected to have relatively smaller shifts in comparison to their equivivalent G_1 multipoles.

The terms in Eq. 4.16 seem to be symmetric in their indices n and p for the two allowable values of m. As a result, one may hypothesize and check numerically or perhaps prove using

induction that $\sigma_n^+ = \sigma_n^-$ and consequently, $S_{11}^{th} = -2S_{1,-1}^{th}$. The induced electric dipole moment's 2-component p_2 depends on $\frac{1}{2}S_{1,-1}^{th} - S_{11}^{th}$ as given in Eq. 4.10 or, effectively, on just $S_{1,-1}^{th}$ because of their inter-relatedness. The induced equivalent electric dipole moment, hence, depends on the multipole amplitude of the equivalent electromagnetic problem $S_{1,-1}$, which is related to $S_{1,-1}^{th}$ by $S_{1,-1} = -2S_{1,-1}^{th}$. Hence, for the purpose of the G_2 problem, only $S_{1,-1}$ is the relevant induced dipole amplitude.

The overall shapes of the relevant S_{1m} vs. $\mathrm{Re}[\varepsilon_p]$ curves for the G_2 problem are similar to those for the G_1 problem. Of course, the peak locations and the magnitudes of S_{1m} do not coincide. The broad and asymmetric continuum that remains for the case when $g = 0$ is narrower for G_2 as shown in Figs. 4.19 and 4.20. The real part of the induced electric dipole given in Eq. 4.16 depends on $\mathrm{Im}[S_{1m}]$ and its imaginary part depends on $\mathrm{Re}[S_{1m}]$. As a result, features of the $\mathrm{Im}[S_{1m}]$ vs. $\mathrm{Re}[\varepsilon_p]$ curve determine the real amplitude of the induced dipole $\mathrm{Re}[\mathbf{p}]$. The broad continua as well as the amounts of peak shifts are determined by the type of coupling between the sphere and the substrate. Horizontal or G_2 coupling seems to be more wavelength specific since, eventually, ε_p can be mapped to wavelength or frequency with a permittivity model or data. Vertical coupling or G_1 coupling leads to significant shifts and a relatively long tail when the sphere is made to touch the substrate. The difference in the response can lead to a dependence on the angle of incidence θ^i.

Induced dipole moments for the case when the sphere was assumed to have a Drude model based permittivity and the substrate were assigned a relatively high permittivity such that

$\beta_S \to 1^-$ were not evaluated for the G_2 problem. It was found that the overall shapes of the curves showed the same kind of features such as peak births, peak shifts, the broad continuum etc. The features, however, were found to be less pronounced. The peak shifts, for example, were relatively smaller etc. The effects of β_S values on the peak locations of the induced dipole moments, although of interest, were not calculated for G_2. It was assumed that since the there is a singular dependence on several real parameters in both problems; one would expect to see a singular dependence on β_S even for the G_2 problem. The asymptotes and the location of the singularities, of course, are not known and could be evaluated in a way similar to that used for G_1. Instead, the dependence of S_{1m} for Ag, Au and Cu spheres present near a Si substrate on the wavelength of the incident light were evaluated to gain more insight into the G_2 interactions among real materials that are frequently used in light trapping applications.

The induced dipole amplitudes were calculated for several values of g for Ag, Au and Cu spheres present near a Si substrate. Figs. 4.21-4.26 show, respectively, the behaviors of $\mathrm{Re}[S_{1,-1}]$ and $\mathrm{Im}[S_{1,-1}]$ values as functions of λ. For the Ag-Si system, the dependence on g is similar to that in the case of G_1 excitation. It is, however, relatively less prominent. Specifically, the peak shift and broadening as $g \to 0$ is much less significant. The overall change in the spectral response as a function of g is relatively lower. For Au-Si and Cu-Si systems, there is an overall increase in the magnitude of the induced dipole amplitude that is of the order of 10 %. Again, this much smaller compared to the order 100 % increase in the magnitude that occurs during vertical excitation. Further, there are no obviously clear maxima in values of $|S_{1,-1}|$ as a function

of g for a given value of λ. It just seems to increase until the sphere is made to touch the substrate.

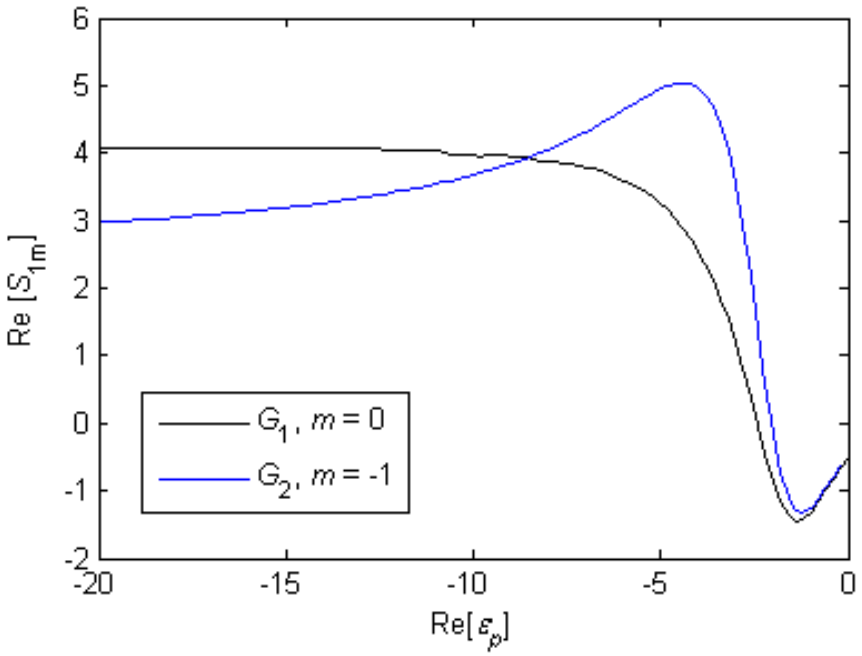

Figure 4.19: The real parts of the induced dipole amplitudes for the two problems when $g = 0$. The imaginary part Im[ε_p] was set to a relatively large value of 1 in order to obtain conveged values.

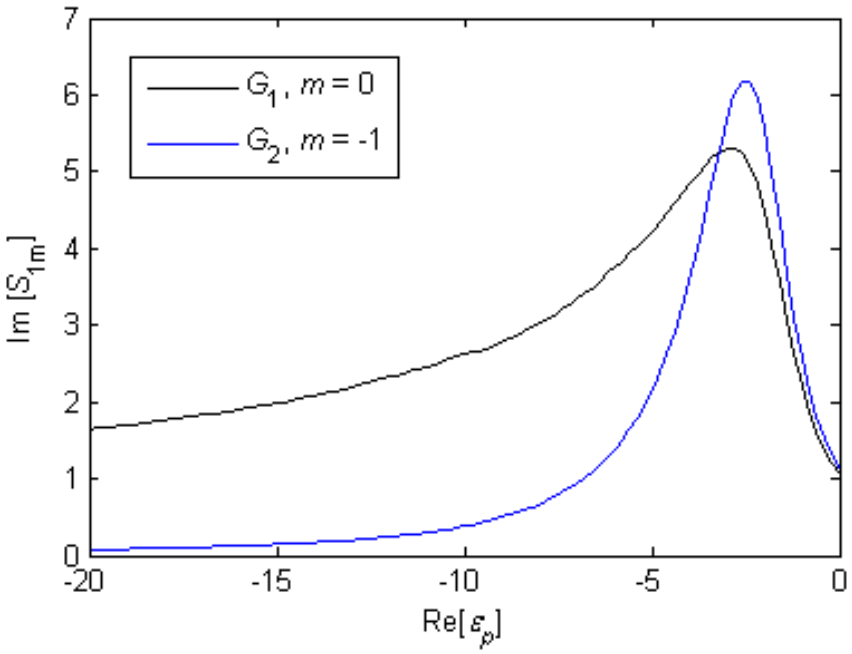

Figure 4.20: The imaginary parts of the induced dipole amplitudes for the two problems when g = 0. The imaginary part Im[ε_p] was set to a relatively large value of 1 in order to obtain conveged values.

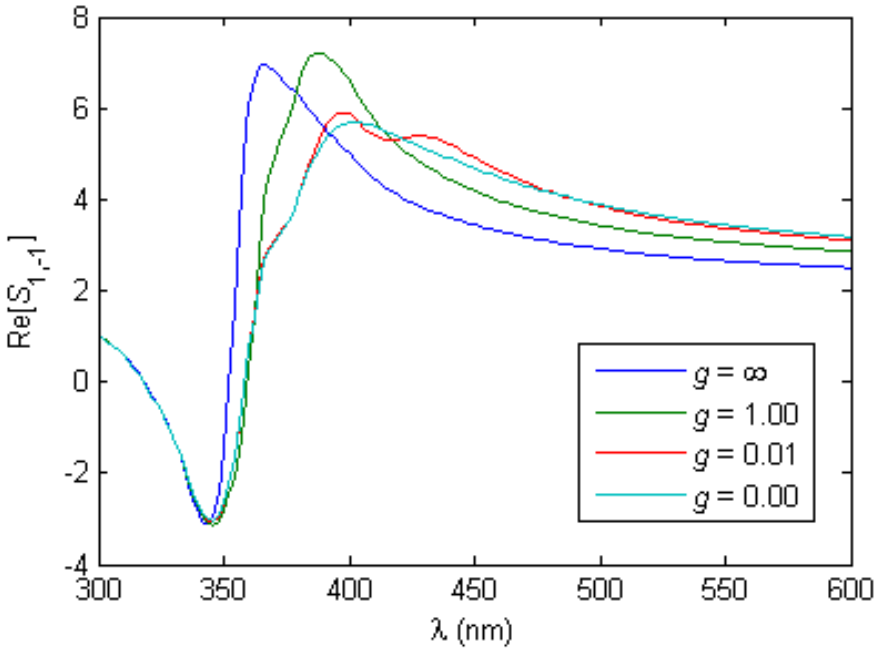

Figure 4.21: The real parts of the induced dipole amplitudes for several values of the gap distance g for an Ag sphere in the vicinity of an infinitely thick Si substrate. The effect of the substrate is relatively less significant in comparison to the G_1 problem.

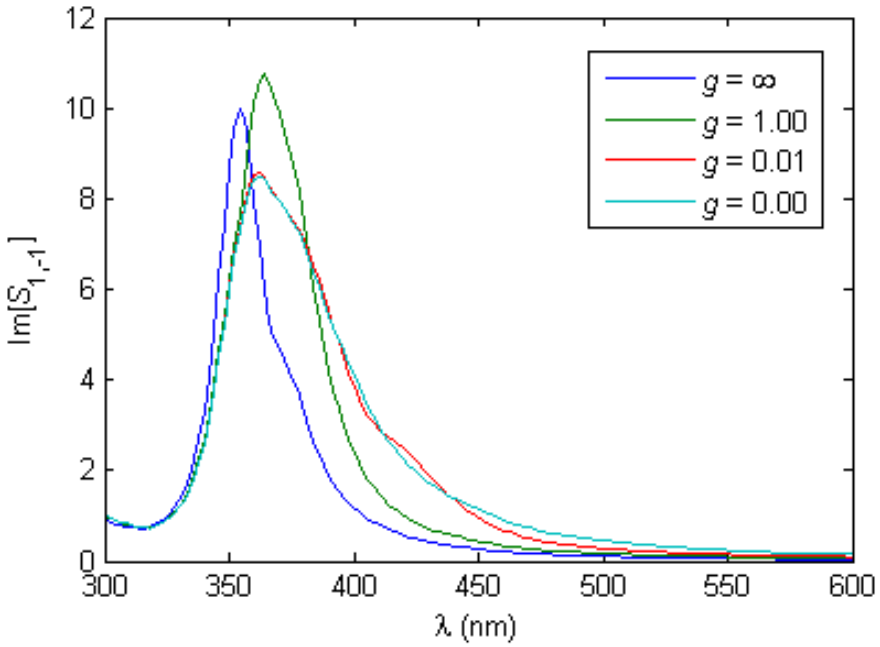

Figure 4.22: The imaginary parts of the induced dipole amplitudes for several values of the gap distance g for an Ag sphere in the vicinity of an infinitely thick Si substrate. The effect of the substrate is relatively less significant in comparison to the G_1 problem. The peak shifts are much smaller. The shifted peaks are eclipsed by the broad continuum as $g \rightarrow 0$. The continuum is also different from that of the equivalent G_2 problem, it is sharper and has a relatively shorter tail.

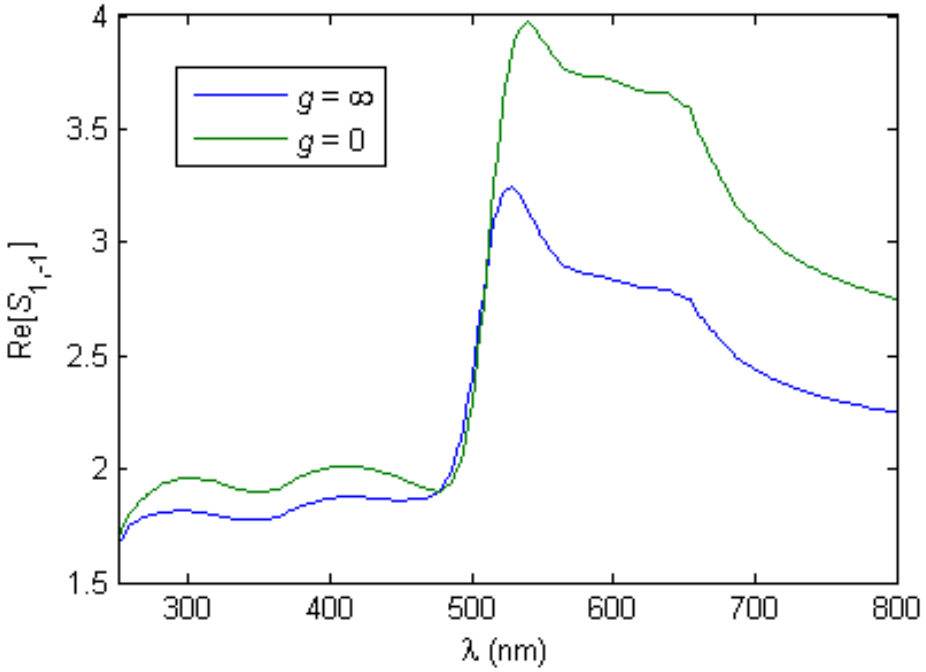

Figure 4.23: The real part of the induced horizontal dipole amplitude for an Au sphere present near a Si substrate. There is ~30% increase in magnitude for $\lambda > 500$ nm.

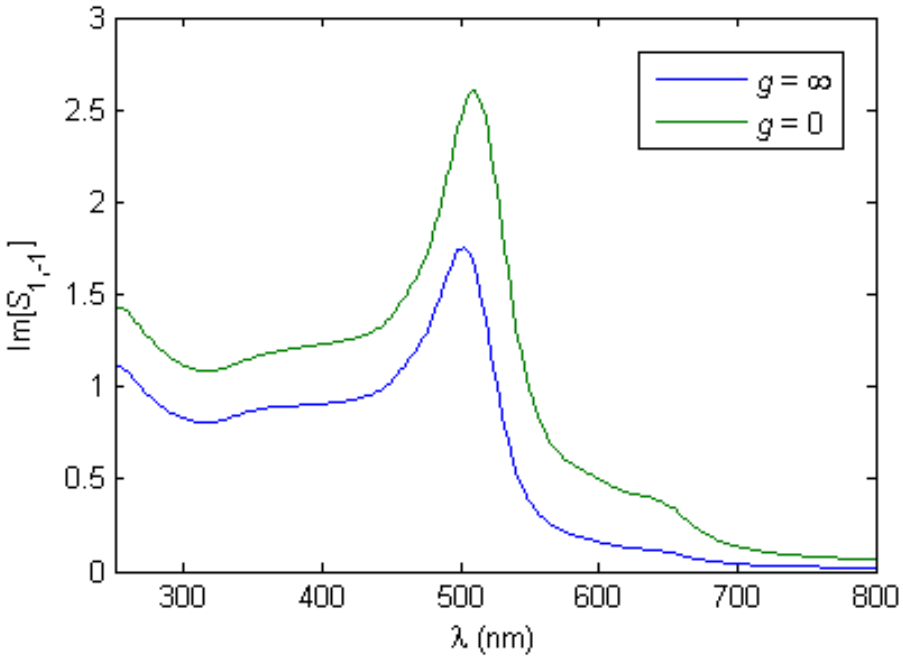

Figure 4.24: The imaginary part of the induced horizontal dipole amplitude for an Au sphere present near a Si substrate. There is an overall increase in value as the sphere is made to approach the substrate.

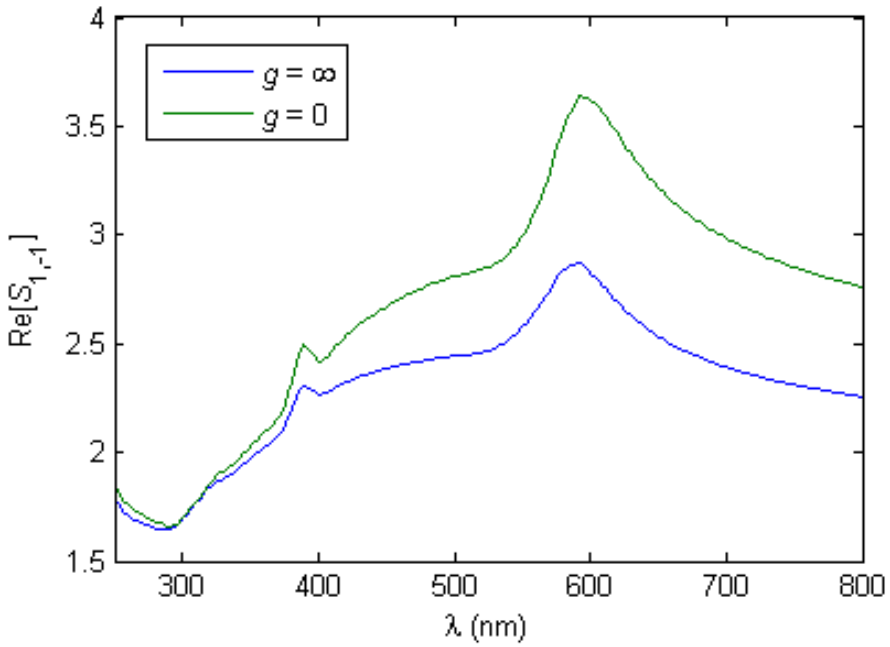

Figure 4.25: The real part of the induced horizontal dipole amplitude for an Au sphere present near a Si substrate. There is ~35% increase in magnitude for $\lambda > 500$ nm.

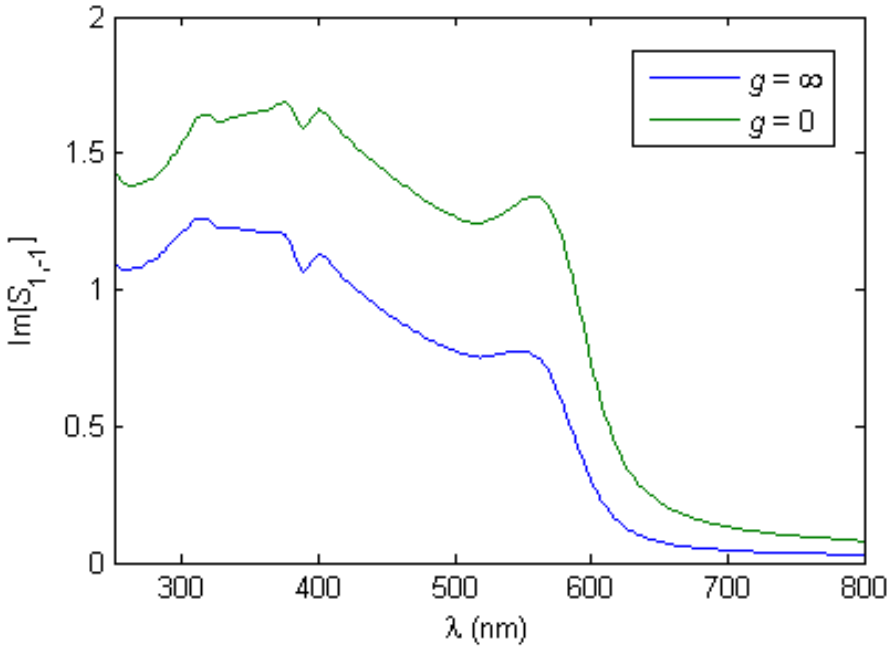

Figure 4.26: The imaginary part of the induced horizontal dipole amplitude for an Au sphere present near a Si substrate. There is an overall increase in value as the sphere is made to approach the substrate.

4.2.3 Effect of Angle

The difference between the responses under G_1 and G_2 excitations points towards an angle dependence of the induced electric dipole **p**. Given an incident field $\mathbf{E}^i$, the evaluation of the induced dipole requires two coupling matrices F_{ij} and D_{ij}. The first relates the applied field to an 'equivalent' thermal gradient **G** and the latter connects the applied gradient to **p**. F_{ij} is given by $F_{ij} = \frac{1}{2}(\delta_{ij} + R_{ij})$ where, $\underline{\mathbf{R}} \equiv \begin{bmatrix} -R^P & 0 & 0 \\ 0 & R^P & 0 \\ 0 & 0 & -R^T \end{bmatrix}$ is a matrix of the reflection coefficients given in the previous section. The matrix D_{ij} is given by $\underline{\mathbf{D}} = \begin{bmatrix} p_1^0 & 0 & 0 \\ 0 & p_2^0 & 0 \\ 0 & 0 & p_2^0 \end{bmatrix}$ where,

p_1^0 and p_2^0 are the the components of the induced dipole for $G_1 = 1$ and $G_2 = 1$ excitations respectively. It turns out that $p_1^0 = -i4\pi\varepsilon a^2 S_{10}$ and $p_2^0 = -i4\pi\varepsilon a^2 S_{1,-1}$. The angle dependence gets into the calculation through the θ^i dependent components of the incident field and the angle dependent values of the reflection coefficients. For an in-plane incident field $\mathbf{E}^i$, $E_3^i = 0$ in the current coordinate system. The components are $\begin{bmatrix} -E^{i0P}\sin\theta^i \\ -E^{i0P}\cos\theta^i \end{bmatrix}$ and the resultant induced dipole is given by $\mathbf{p} = i4\pi\varepsilon a^2 \begin{bmatrix} E^{i0P} S_{10}\sin\theta^i (1-R^P) \\ E^{i0P} S_{1,-1}\cos\theta^i (1+R^P) \end{bmatrix}$. For a transverse incident field, there is only E_3^i and the induced dipole moment is given by $p_3 = -i4\pi\varepsilon a^2 E^{i0T} S_{1,-1}(1-R^T)$. A more concise representation would be the following:

$$\mathbf{p} = 4\pi\varepsilon a^2 \begin{bmatrix} S_{10}\Theta_1 \\ S_{1,-1}\Theta_2 \\ S_{1,-1}\Theta_3 \end{bmatrix} \tag{4.19}$$

where,

$$\Theta_1 \equiv i\sin\theta^i (1-R^P), \tag{4.20a}$$

$$\Theta_2 \equiv i\cos\theta^i (1+R^P) \tag{4.20b}$$

and

$$\Theta_2 \equiv -i(1-R^T). \tag{4.20c}$$

The calculated values of the incident angle dependent functions Θ_i for Si are given in the following Figs. 4.27-4.31. The following equations for the reflection coefficients were used:

$R^P = \frac{\sqrt{\varepsilon_S}\cos\theta^i - \cos\theta^t}{\sqrt{\varepsilon_S}\cos\theta^i + \cos\theta^t}$ and $R^T = \frac{\cos\theta^i - \sqrt{\varepsilon_S}\cos\theta^t}{\cos\theta^i + \sqrt{\varepsilon_S}\cos\theta^t}$ with $\cos\theta^t = \frac{k_2^i}{k^S} = \frac{1}{\sqrt{\varepsilon_S}}\sin\theta^i$ to accommodate a complex value of ε_S. The resulting coefficients are

$$R^P = \frac{\varepsilon_S\cos\theta^i - \sin\theta^i}{\varepsilon_S\cos\theta^i + \sin\theta^i} \tag{4.21}$$

and

$$R^T = \frac{\cos\theta^i - \sin\theta^i}{\cos\theta^i + \sin\theta^i}. \tag{4.22}$$

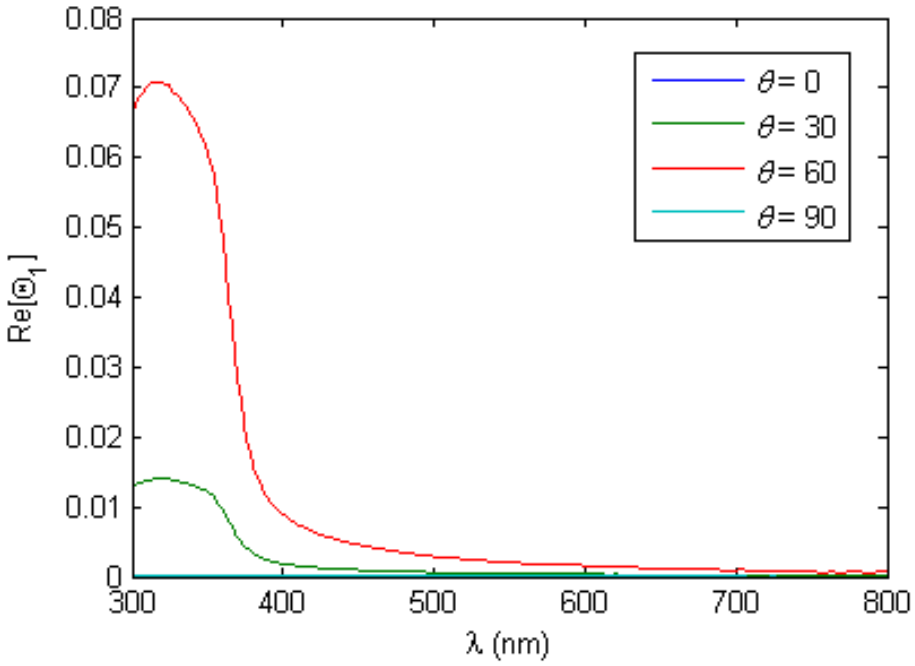

Figure 4.27: The dependence of the real part of the substrate material dependent angle function Θ_1 on the wavelength of the incident light. It is, for most part of the wavelength range of interest, a positive number of the order 0.01. The direct band gap of Si causes values to be relatively large for $\lambda < 400$ nm.

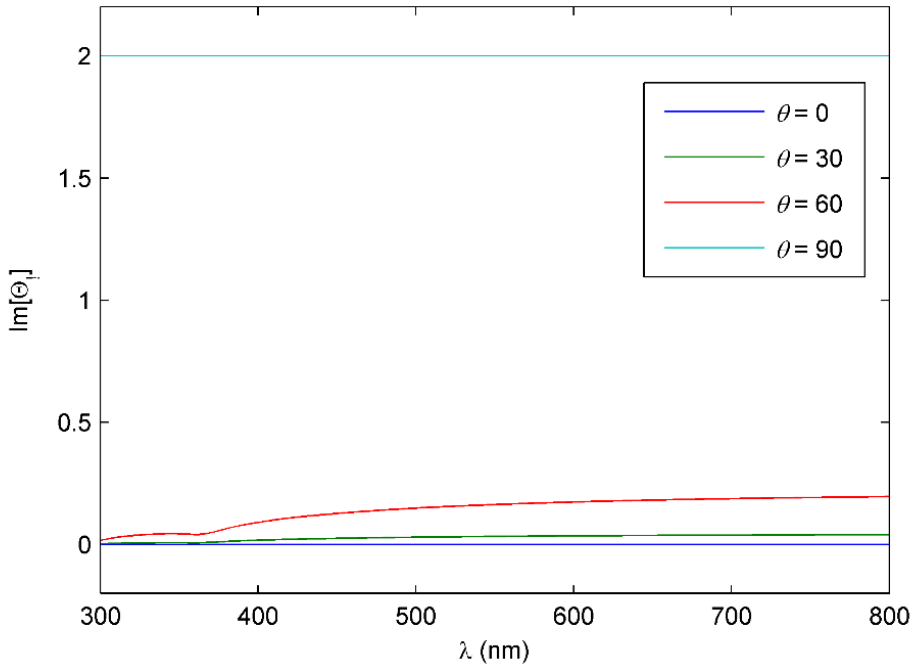

Figure 4.28: The dependence of the imaginary part of the substrate material dependent angle function Θ_1 on the wavelength of the incident light. A strong nonlinear incident angle dependence can be seen. At close to grazing angles, the value approaches 2 monotonically from 0 at normal incidence.

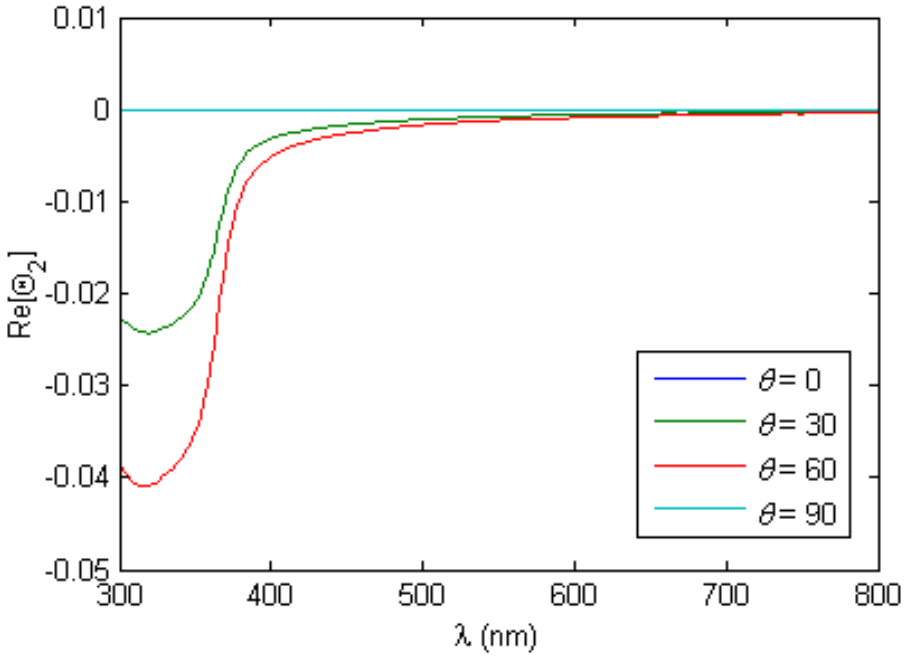

Figure 4.29: The dependence of the real part of the substrate material dependent angle function Θ_2 on the wavelength of the incident light. It is, for most part of the wavelength range of interest, a negative number of the order 0.01. The direct band gap of Si causes values to be relatively large for $\lambda < 400$ nm.

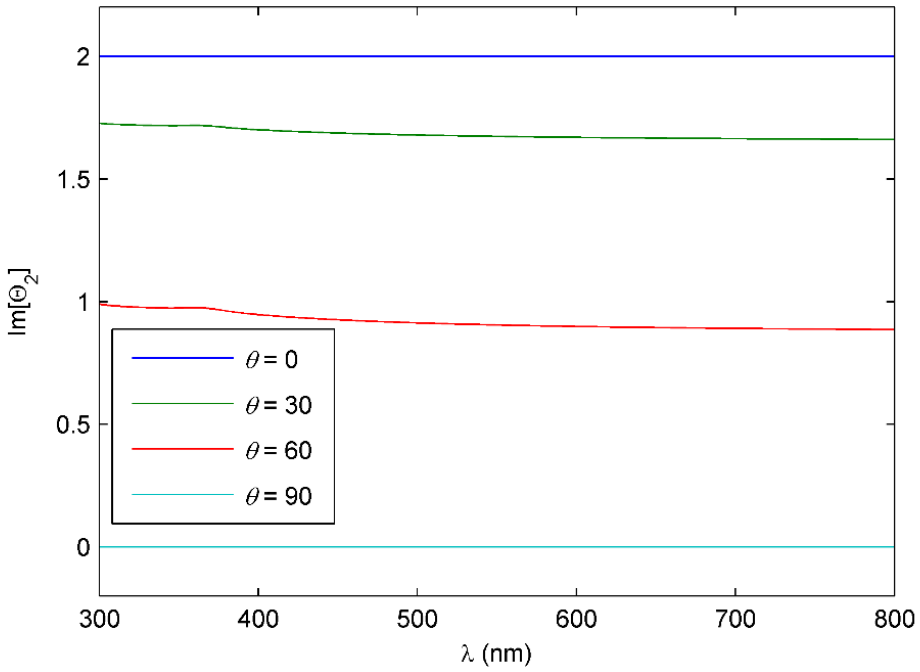

Figure 4.30: The dependence of the imaginary part of the substrate material dependent angle function Θ_2 on the wavelength of the incident light. A nonlinear incident angle dependence can be seen. At close to normal angle, the value approaches 2 monotonically from 0 at grazing incidence.

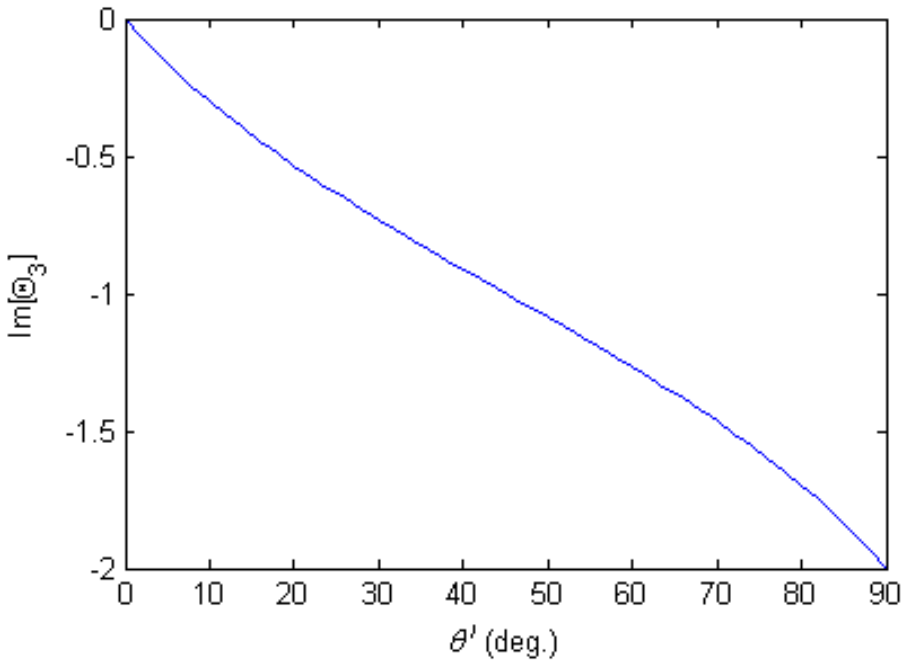

Figure 4.31: The Θ_3 function's dependence in the incident angle. The real part is equal to zero and there is no λ dependence. The incidence angle dependence is very close to being a linear relationship. The resulting dipole moment, p_3 is largest for grazing angle of incidence and equals zero for a normal incidence.

It can be observed from the figures that exciting a vertical dipole requires the use of in-plane polarized light as well as a very wide angle of incidence. The relative value $\frac{\mathrm{Im}[\Theta_1]}{\mathrm{Im}[\Theta_2]}$ exceeds one only for θ^i that is very close 90°. For a randomly polarized light that is incident at angles that are close to normal, as would be the case for sunlight in the context of a solar cell, the induced vertical dipole moment can be expected to be very insignificant. The resulting effects corresponding to the G_1 problem would not be present. The functions Θ_i are only substrate and angle of incidence dependent allowing the possibility of tuning them in such a way that the vertical dipole is induced at angles that are not as wide as those that would be required for a bare

Si surface. The values S_{1m} would also change in such a situation making that design problem somewhat more complicated that just thin-film design.

4.3 CONCLUSIONS

The dependence of the induced electric dipole on gap distance, polarization and the angle of incidence in the presence of a substrate was analyzed in this chapter. The most important aspect on the analysis was the use of the Laplace harmonics to describe the interaction or coupling in greater detail than using just a simple electrostatic dipole, a numerical method such as the finite difference time domain method or experiments to measure the response of nanoparticles present on a substrate to linear electromagnetic excitation [33-36]. The eventual goal was to be able to calculate the trapped light flux within the substrate. Calculations discussed in the literature do not seem to touch upon the fact the induced dipole has a significant dependence on the gap distance and the substrate material. Consider, for example, the work of Catchpole et al. in which the enhancement of photocurrent for a plasmonic solar cell is modeled by assuming that the metal nanoparticles are non-interacting ideal dipoles that radiate of scatter light into the substrate [37]. Interestingly, it was not possible to find, using scholar.google.com, any article within the list of articles citing this reference that discussed a situation where in the nanoparticle is considered to be not just simple radiating dipole source. In that sense, this work can be considered novel. There are several ways in which the trapped flux resulting from the presence of a dipole of an arbitrary orientation can calculated. For substrates that are thick enough to be considered semi-infinite the book by Novotny and Hecht can be used to calculate the exact values of the power that is trapped in the solid angles that are accessible with and without near-field optical effects [38]. For a layered substrate, the method used by Catchpole et al. can be used [37]. However, one has to keep in mind that their method is a concoction of several reported methods and hence needs to be carefully analyzed before trusting. In either case, there are several artifacts that need to be analyzed in order to develop an understanding of the

way the incident light and the location of a nanosphere relative to the substrate affect the amount of in-coupled light disregarding the effect of sphere diameter, especially when there is a finite dissipation in the substrate. In this work, only the induced dipole and its orientation are calculated with sufficient details with regard to the coupling with the substrate. The calculated values can be fed into another calculation framework that is capable to evaluating the trapped light fluence given an arbitrarily oriented electric dipole. The problem of the evaluation of fields given a current source in the vicinity of a layered medium is also an outstanding one because of the difficulties associated with the numerical evaluation of what is known as the 'Sommerfeld integral' that results from the integral representation of the fields—an electric dipole is the simplest case and hence allows for some simplification and permits some kind of numerical acceleration of the integration [39]. As discussed here, in case of a polarizable particle present near a substrate, not only the effect of a dipole near an interface needs to be calculated but also the value of the dipole that is induced as a result of the interaction of the particle substrate system with an incident field. One may argue that the incident field has to emerge from a source, a plane source in case of plane waves or a point source with an infinite amplitude such that its far-field is an incident plane wave etc. In that case, the problem can become more complicated and incident plane wave excitation can be seen as an approximation of the problem. Further, if one thinks about a finite diameter beam as the incident excitation, the nature of its source not being known, then one has to re-represent the beam in terms of plane waves that can be treated as emerging from a sources whose far-fields are the constituent plane waves etc. This would take care of realistic effects such as the Goos-Hänchen shift in the reflected beam—the effect may be necessary to analyze problems in which small clusters of nanospheres are excited using a beam of light. Hence, in a way the problem of simultaneous excitation of a polarizable object or

antenna in the vicinity of a substrate that is potentially layered was partially studied here. All this assuming classical linear electromagnetic effects. The use of either intense light, diffuse light or very low photon rate light and, for that matter, very tiny particles such that effects of quantum confinement become significant, would require a very significant change in the way the problem is formulated. Of course, the main idea is that all those problems can be built from the current one as long as the "extra" effects are relatively "small".

Here, it was found that, inclusion of up to $O(ka)$ effects also leads to coupling effects that are rich in new physics and are inherently non-linear in terms of parameters such as the distance between the sphere are the substrate, sphere and substrate permittivities, wavelength and sphere diameter. There is a very clear polarization, and angle of incidence dependence. It is, perhaps, obvious from the point-of-view of basic optics of interfaces. Under differently oriented excitations, the induced electric dipole remains oriented in the same direction as the applied field, however, its complex valued amplitude changes. The total power radiated by a dipole **p** is given by $P = \left|\left|\mathbf{p}\right|^2\right| \frac{\varepsilon^{1/2}\omega^3}{12\pi\varepsilon_0 c^3}$ depends only on the amplitude of the complex vector amplitude. The amplitude $\left|p\right|$ undergoes a maximum in a manner similar to the peak in the imaginary part of the dipole amplitudes discussed in this chapter. Clearly, for a given distance between the sphere and the substrate, the effect of sphere-substrate coupling need to be considered.

The intrinsic resonant behavior of a sphere is also significantly affected by its presence near a substrate. The effects are highly non-linear. Due to multipolar coupling between the sphere and the substrate, several resonances are observed. The resonance locations occur for more and more negative real values of the sphere's permittivity for a fixed small imaginary sphere permittivity. Eventually, as a sphere is made to approach the substrate, resonances shift

toward larger values of sphere's negative real permittivity that correspond to a larger value of the wavelength for metals such as Ag, Au and Cu. The red-shifts seem to depend also on the permittivity of the substrate, or equivalently, through the quantity β_S . This is consistent with the trend reported in literature [33].

A major consequence of the substrate coupling is the broadening of the otherwise relatively narrow wavelength dependent response of an Ag sphere when the sphere is made to touch a Si substrate. Of course, electrical insulation is implied. Such broadening is found to occur under both kinds of excitations. In case of metals that have relatively higher optical resistivity such as Au and Cu, the substrate coupling effect leads insignificant amounts of shifts and broadening. The responses seem to increase in an overall sense by *O*[10%] indicating that only Ag nanospheres seem to lead to a significant change in the spectral response.

5 SEVERAL NANOSPHERES IN A HIGH REFRACTIVE INDEX TRANSPARENT MATRIX

5.1 INTRODUCTION

Nanoparticulate plasmonic composite materials have recently become technologically important, especially in the growing interdisciplinary fields of plasmonics and meta-materials [40-45]. Fabrication of such plasmonic nanocomposites is accomplished through well-established methods such as surfactant mediated self-assembly [14], laser dewetting of thin films [46], sol-gel assembly [47-49], ion-implantation [50, 51] and vacuum evaporation of thin films [8] among others. Technologically, such composites are important in the fields of energy harvesting [6, 14, 15, 52], random lasers [53], sensing [15, 54], photo-catalysis [55] etc. Free electrons in noble metal nanoparticles (NPs) give rise to a characteristic plasmon resonance wherein the NPs absorb and scatter radiation with a marked intensity [4, 30, 42, 56]. The linear optical response of such materials can be described by Maxwell equations in both the dispersed and continuous phases when the particle size is greater than a few nanometers. In the case of metal nanoparticles in a transparent medium, the matrix phase can be treated as a dielectric with real electrical permittivity ε_m while the NPs should be treated as materials with complex, frequency-dependent permittivity ε_p. A plasmon resonance occurs for $\Re(\varepsilon_p / \varepsilon_m) = -2$ in the case of spheres. The overall optical response of such composite materials can be determined by numerically solving Maxwell equations in both phases subject to the continuity of tangential components of magnetic and electric fields at the interface of the embedded particles and the

surrounding matrix phase. Such calculations are possible by utilizing computational techniques such as the finite difference time domain method [57-59]. However, substantial computational effort is required especially near resonant frequencies where steep field gradients necessitate the use of very fine spatial resolution [59]. Hence, theories capable of accurately predicting the average optical properties of random composites could be a valuable tool in knowledge-based design of plasmonic composites.

Composite media are inherently inhomogeneous. Hence, their average electromagnetic behavior depends on the permittivities and volume fractions of the constituent components. Effective medium theories have been used to parameterize the properties of such media [60]. In the case of monodisperse spherical particulate composites, where the particle radius a is much smaller than the wavelength of exciting radiation λ, the effective permittivity can be modeled under the quasistatic approximation wherein the wave nature of the EM fields can be neglected. Specifically, for the case of plasmonic composites in the optical frequency range, the magnetic response in the optical range is the same as that of vacuum and the classical Maxwell-Garnett theory (MGT) [61] can be used to predict the effective permittivity. Similarly, in the case $\lambda << a$, ray optics can be utilized. However, for nanoscopic plasmonic composites in the optical range, λ can be $O(a)$ or $ka \equiv 2\pi\sqrt{\varepsilon}a/\lambda$ is $O(1)$. Hence, the effects of diffraction and scattering by the NPs become significant and simple models designed for either one of the extreme cases are not applicable. Extended Maxwell-Garnett theories have been developed in the literature for this regime [62-65]. However they are correct only up to $O(\phi)$ (ϕ: volume fraction of the dispersed phase) and do not account for the effect of microstructure on the permittivity. In this work, we have developed a self-consistent theoretical framework for the prediction of the

effective linear optical properties of dense random monodisperse spherical particulate plasmonic composites with particle size on the order of the exciting wavelength of radiation. This effective-medium theory (EMT) is based a method employed for the accurate prediction of sound attenuation and phase speed in acoustically resonant monodisperse suspensions of microspheres by Spelt et al. [66]. The microstructure information is incorporated through the static structure factor $S(\mathbf{0})$. It has been shown that the leading order correction term in terms of the particle volume fraction to the velocity field in Stokes flow, i.e., "slow" flow of a viscous liquid in which inertial forces are negligibly small, for infinite randomly distributed monodisperse spheres depends linearly on the static structure factor $S(\mathbf{0})$ [67]. Both Stokes flow equations and Maxwell wave equations, take the form of a vector Helmholtz equation for the fluid velocity and electric field respectively. Hence, the methodology developed by Spelt et al. [66] can be adapted to derive an EMT for electromagnetic wave propagation problems in heterogeneous media. Specifically, the composite medium is represented by a layered structure in which the particle, in its immediate vicinity, is surrounded by the dielectric matrix up to a distance R which is a function of $S(\mathbf{0})$. The structure is assumed to be embedded in an effective continuum whose permittivity ε_{eff} is determined by the self-consistent solution of Maxwell equations. The EMT is mathematically identical to the Maxwell-Garnett model in the limit as the particle diameter d_p and volume fraction ϕ approach zero. However, for finitely large volume fractions the variations in the permittivity with respect to ϕ and d_p are highly nonlinear.

The chapter is organized as follows. Problem formulation is presented in §2. §2A contains the derivation of the ensemble averaged Maxwell equations and in §2B, the EMT is discussed. §3 contains a summary of the solution technique and computational methods used to calculate the conditionally averaged electric field. Analytical and numerical results are discussed

in §4. Results of the scalar EMT is discussed in §4A and those of vector EMT in §4B. Ag nanoparticulate composite in an $\varepsilon_m = 7$ dielectric is used as a model system. A discussion of the conditions under which the effective permittivity is resonant is presented in subsections §§4A and B. Effects of particle radius are also discussed in §4B. §4C contains a discussion of Fano-resonance that results from particle-effective medium coupling. Conclusions are offered in §5.

5.2 ENSEMBLE AVERAGED MAXWELL EQUATION

We consider a random monodisperse, non-overlapping spherical particulate composite in which the electrical permittivity of the matrix is assumed to be real, positive and constant while that of the plasmonic particles is complex and frequency-dependent. Further, as mentioned in the Introduction, we assume that the magnetic permeabilities of the matrix and the particle phase to be equal to that of vacuum, i.e., $\mu_m = \mu_p = \mu_0$. This assumption is justified for dielectric matrices such as glass or water and particles of noble metals such as Ag or Au. The particle diameter is assumed to be much greater than the electron mean free path in the metal. Hence, quantum confinement effects are neglected. The embedding medium is isotropic and homogenous and could either be a liquid or a solid phase. For such a system, ensemble-averaged Maxwell equations can be derived as described below.

Time-harmonic electric and magnetic fields in a source-free homogenous medium satisfy Maxwell's wave equations. For the matrix these equations are given by

$$\nabla \times \mathbf{E}_m = i\omega\mu_m \mathbf{H}_m, \quad \nabla \times \mathbf{H}_m = -i\omega\varepsilon_m \mathbf{E}_m, \tag{5.1}$$

where $\mathbf{E}_m$ and $\mathbf{H}_m$ are the amplitudes of the electric and magnetic fields respectively, ω is the frequency, μ_m and ε_m are the magnetic permeability and electric permittivity respectively, and the subscript *m* denotes the matrix medium. Similar equations apply in the particulate phase with the subscript *m* replaced by the particle phase subscript *p*.

To obtain a macroscopic description of a random composite, we must first obtain ensemble-averaged equations. Let g_p denote an indicator function for the particle phase whose value at a point $\mathbf{x}$ is unity if that point lies inside a particle and zero otherwise. Note that an

ensemble-average of this function is equal to the volume fraction of the particles, i.e., $\langle g_p \rangle(\mathbf{x}) = \phi$, where the angular brackets denote an ensemble-averaged quantity. The ensemble-averaged Maxwell's equations for the random composites are obtained by multiplying the Maxwell's equations for the particle phase by its indicator function g_p and those for the matrix phase by $1-g_p$, and adding the two resulting equations:

$$\nabla \times \langle \mathbf{E} \rangle + \langle \nabla g_p \times (\mathbf{E}_m - \mathbf{E}_p) \rangle = i\omega\mu_0 \langle \mathbf{H} \rangle, \tag{5.2a}$$

$$\nabla \times \langle \mathbf{H} \rangle + \langle \nabla g_p \times (\mathbf{H}_m - \mathbf{H}_p) \rangle = -i\omega \left[\varepsilon_m \langle \mathbf{E} \rangle + (\varepsilon_p - \varepsilon_m) \langle g_p \mathbf{E} \rangle \right]. \tag{5.2b}$$

Note that ∇g_p is zero at all points except at the matrix-particle interface where it is directed along the normal to the interface. Hence, its cross product with the difference in **E** or **H** across the interface is zero due to the fact that the tangential components of the electric and magnetic fields are continuous across the interface. Therefore, the second terms on the left-hand side of Eqs. 2a and 2b vanish. The term in square brackets on the right-hand side of Eq. 5.2b is represents the averaged electric displacement $\langle \mathbf{D} \rangle$ in the medium. We let $\langle \mathbf{D} \rangle = \varepsilon_{eff} \langle \mathbf{E} \rangle$. Hence, the effective permittivity can be defined as

$$\varepsilon_{eff} \langle \mathbf{E} \rangle = \varepsilon_m \langle \mathbf{E} \rangle + (\varepsilon_p - \varepsilon_m) \langle g_p \mathbf{E} \rangle. \tag{5.3}$$

The wavenumber, defined as $k_\nu^2 = \omega^2 \mu_\nu \varepsilon_\nu, \nu = p, m$, also obeys Eq. 3. Hence, the effective wavenumber is given by $k_{eff}^2 = \omega^2 \mu_0 \varepsilon_{eff}$. Eqs. 2a, 2b and 3 can be combined using a curl

operation on Eq. 2a. The resulting $\nabla\times\nabla\times\langle\mathbf{E}\rangle$ term can be shown to be equal to $-\nabla^2\langle\mathbf{E}\rangle$ because $\nabla\cdot(\nabla\langle\mathbf{E}\rangle)=\mathbf{0}$ in the absence of free charge.

The averaged field inside the particles, given by $\langle g_p\mathbf{E}\rangle$, is an unknown quantity defined as:

$$\langle g_p\mathbf{E}\rangle(\mathbf{r}) \equiv \int_{|\mathbf{r}-\mathbf{r}_1|\le a} \langle\mathbf{E}(\mathbf{r})\,|\,\mathbf{r}_1\rangle P(\mathbf{r}_1)\,dV_{\mathbf{r}_1}. \tag{5.4}$$

Here, $P(\mathbf{r}_1)=3\phi/4\pi a^3$ is the probability of finding a particle at $\mathbf{r}_1$, ϕ is the particle volume fraction, and $\langle\mathbf{E}(\mathbf{r})\,|\,\mathbf{r}_1\rangle$ is the conditionally averaged electric field. Since the governing equations are linear and the medium is overall assumed to be macroscopically isotropic, $\langle g_p\mathbf{E}\rangle$ can be expressed as

$$\langle g_p\mathbf{E}\rangle(\mathbf{r}) = \Omega(\phi,k_{eff})\,\phi\langle\mathbf{E}\rangle(\mathbf{r}), \tag{5.5}$$

where Ω is a constant that depends on k_{eff}, ϕ and the microstructure. Combination of Eqs. 3 and 5 gives ε_{eff} or equivalently k_{eff} as follows:

$$k_{eff}^2 = k_m^2 - (k_p^2 - k_m^2)\Omega\phi. \tag{5.6}$$

The ensemble averaged Maxwell equation given by

$$(\nabla^2 + k_{eff}^2)\langle\mathbf{E}\rangle = \mathbf{0}, \tag{5.7}$$

is obtained by eliminating **H** from Eqs. 2a and 2b followed by a substitution of k_{eff}^2 from Eq. 6. Ω can be evaluated by solving Eq. 7 followed by substitution of $\langle \mathbf{E} \rangle$ and $\langle g_p \mathbf{E} \rangle$ into Eqs. 5 and 6. However, because Ω is a function of k_{eff}, Eqs. 6 and 7 need to be solved by an iterative numerical method for the evaluation of the zeros of the following function:

$$\Lambda(k_{eff}^2) = k_{eff}^2 - k_m^2 - \phi(k_p^2 - k_m^2)\Omega(k_{eff}^2) = 0. \tag{5.8}$$

5.2.1 The effective medium model

To determine Ω we must determine the conditionally averaged **E** with one particle fixed and then evaluate the integral in Eq. 4. We shall use an effective medium model that has been shown to provide excellent predictions, consistent with rigorous computations that take into account multi-particle interactions of the conditionally averaged field and effective properties such as elastic moduli, attenuation and speed of acoustic waves, hydraulic permeability, effective viscosity and particle diffusivity in suspensions [21, 66-70]. As illustrated in Fig. 1, in this model, the conditionally-averaged fields satisfy the governing equations for the suspending medium up to a distance *R* from the center of the particle and the governing equations for the effective medium beyond that distance. *R* is related to the static structure factor *S*(**0**) as

$$\frac{R}{a} = \kappa = \left(\frac{1 - S(\mathbf{0})}{\phi} \right)^{\frac{1}{3}}, \tag{5.9}$$

where

$$S(\mathbf{0}) \equiv \int_0^\infty [P(\mathbf{r} \mid \mathbf{r}_1) - P(\mathbf{r}_1)] d\mathbf{r}. \tag{5.10}$$

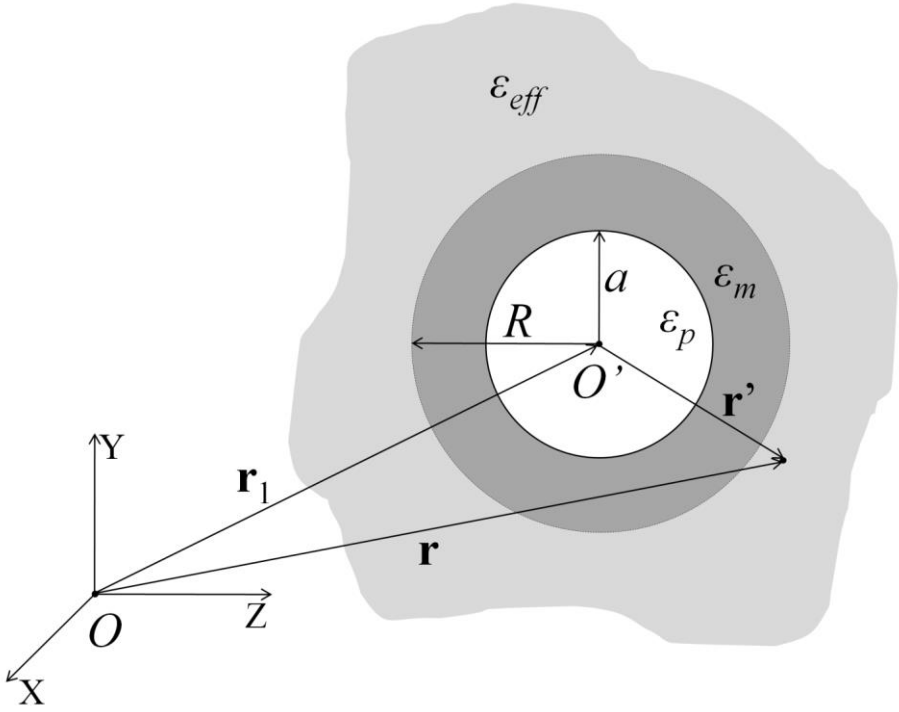

Figure 5.1: A schematic of the geometry considered for the EMT. The problem of finding the conditionally averaged field in a random medium was reduced to the problem of calculating the fields in this geometry. As $r \to \infty$, $\langle \mathbf{E} \rangle (\mathbf{r}) = \hat{\mathbf{x}} \exp(ik_{eff} z)$. The unconditionally averaged wave is assumed to be X-polarized in the present analysis. The choice of $\mathbf{r}_1$ is arbitrary for a given origin *O*.

In Eq. 10, $P(\mathbf{r} \mid \mathbf{r}_1)$ is the conditional probability density of the spheres. The quantity $S(\mathbf{0})$ can be interpreted as the integral of excess probability with respect to the uniform distribution. It needs to be accounted for if the random medium is to be replaced with a homogenous effective medium. In Fig. 1, *O* denotes the origin and *O'* denotes the centre of the particle and the particle is located at $\mathbf{r}_1$. Position vectors $\mathbf{r}'$ originate at *O'* such that $\mathbf{r} = \mathbf{r}_1 + \mathbf{r}'$.

As pointed out by Dodd et al. [68], the above choice of *R* is necessary to ensure that the conditionally averaged field has the correct behavior at large distances from the test particle for the problem of determining the averaged diffusivity of integral membrane proteins. Subsequent studies showed that the above choice also yields excellent estimates of the effective properties even when it has no rigorous basis (as e.g., see [66, 71]). Random suspensions with a hard-sphere potential have a non-zero $S(\mathbf{0})$ even in the dilute limit, which is accurately given by the Carnahan-Starling approximation [72] as:

$$S(\mathbf{0}) = \frac{(1-\phi)^4}{1+4\phi+4\phi^2-4\phi^3+\phi^4}. \tag{5.11}$$

As $\phi \to 0$, $\kappa = 2 - \frac{3}{2}\phi + O(\phi^2)$. On the other hand, well-separated dilute random arrays [41] have $P(\mathbf{r} \mid \mathbf{r}_1) = 0$ for $2 < r' < \phi^{-1/3}$, $S(\mathbf{0}) = 0$ and hence, $\kappa = \phi^{-1/3}$. We study both cases to elucidate the differences between them. Our effective medium theory is used to evaluate $\langle \mathbf{E}(\mathbf{r}) \mid \mathbf{r}_1 \rangle$ in Eq. 4.

5.3 SOLUTION TECHNIQUE

This section is devoted to a discussion on the determination of $\langle \mathbf{E}(\mathbf{r}) | \mathbf{r}_1 \rangle$ for $r' < a$, and subsequently, the numerical calculation of ε_{eff}. We first show that for composites with spheres that are small compared to the wavelength of the exciting light (or equivalently, as $ka \to 0$), $\langle \mathbf{E}(\mathbf{r}) | \mathbf{r}_1 \rangle$ and hence ε_{eff} can be determined analytically by solving the electrostatic Maxwell equations (which is equivalent to setting $ka = 0$). Further, we show that both the electrostatic approximation and Maxwell wave equations can be reduced to Laplace equation for a scalar potential in the limit as $ka \to 0$. However, the boundary conditions for these two problems are different from each other. Since only a scalar potential is necessary to describe a static **E** field, the resulting EMT is referred to as the '*scalar EMT*'. Thereafter, an iterative method for the numerical evaluation of ε_{eff} using Maxwell wave equations for arbitrary large values of *ka* is outlined. EMT based on Maxwell wave equations is referred to as the '*vector EMT*' as it involves solution of a vector Helmholtz equation. The boundary conditions for these two problems differ from each other as explained below.

5.3.1 Scalar EMT

In this section, we will show that in the limit as $ka \to 0$, Maxwell wave equations given by $(\nabla^2 + k^2)\mathbf{E} = \mathbf{0}$ can be approximated by the electrostatic Maxwell equation given by $\nabla \cdot \mathbf{E}_S = 0$ for which $ka \equiv 0$ even though these equations require different boundary conditions. The electrostatic approximation is valid only for problems with a spherical symmetry and hence is not applicable to systems involving multiple spheres or non-spherical particles.

The static electric field $\mathbf{E}_S$ obeys $\nabla \cdot \mathbf{E}_S = 0$ and hence, can be represented as the gradient of a scalar potential Θ such that $\mathbf{E}_s = \nabla\Theta$. Therefore, $\nabla^2\Theta = 0$. Across an interface containing no free charge, Θ and the electric displacement $\mathbf{D}_s \equiv \varepsilon \mathbf{E}_s$ are continuous. Therefore, across a spherical interface between the particle and the medium shown in Fig. 1,

$$\Theta_p = \Theta_m \tag{5.12a}$$

and

$$\varepsilon_p \left.\frac{\partial\Theta}{\partial r}\right|_p = \varepsilon_m \left.\frac{\partial\Theta}{\partial r}\right|_m . \tag{5.12b}$$

At an interface with no free charge and current, **E** and **H** are required to have continuous tangential components. A comparative analysis can be performed by decomposing **E** and **H** into toroidal Ψ and poloidal Φ scalar potentials in the following way [17, 66, 73]. Let

$$\mathbf{E} = \nabla \times (\mathbf{r}\Psi) + \nabla \times \nabla \times (\mathbf{r}\Phi) \tag{5.13a}$$

and

$$\mathbf{H} = -i\omega\varepsilon \nabla \times (\mathbf{r}\Phi) + \frac{1}{i\omega\mu_0} \nabla \times \nabla \times (\mathbf{r}\Psi), \tag{5.13b}$$

where Ψ and Φ are solutions to the scalar Helmholtz equation. Tangential components $E_\theta, E_\phi, H_\theta$ and H_ϕ can be expressed as follows [42-43]:

$$E_\theta = \frac{1}{\sin\theta}\frac{\partial\Psi}{\partial\phi} + \frac{1}{r}\frac{\partial^2(r\Phi)}{\partial r\,\partial\theta}, \tag{5.14a}$$

$$E_\phi = -\frac{\partial \Psi}{\partial \theta} + \frac{1}{r}\frac{\partial^2 (r\,\Phi)}{\partial r\,\partial \phi}, \tag{5.14b}$$

$$H_\theta = \frac{-i\omega\varepsilon}{\sin\theta}\frac{\partial \Phi}{\partial \phi} + \frac{1}{i\omega\mu_0\, r}\frac{\partial^2 (r\,\Psi)}{\partial r\,\partial \theta}, \tag{5.14c}$$

and

$$H_\phi = i\omega\varepsilon\frac{\partial \Phi}{\partial \theta} + \frac{1}{i\omega\mu_0\, r}\frac{\partial^2 (r\,\Psi)}{\partial r\,\partial \phi}. \tag{5.14d}$$

Continuity of the above tangential components of **E** and **H** at the interface necessitate that

$$\Psi_p = \Psi_m, \tag{5.15a}$$

$$\left.\frac{\partial}{\partial r}(r\,\Psi)\right|_p = \left.\frac{\partial}{\partial r}(r\,\Psi)\right|_m, \tag{5.15b}$$

$$\varepsilon_p \Phi_p = \varepsilon_m \Phi_m \tag{5.15c}$$

and

$$\left.\frac{\partial}{\partial r}(r\,\Phi)\right|_p = \left.\frac{\partial}{\partial r}(r\,\Phi)\right|_m. \tag{5.15d}$$

As $ka \to 0$, $\nabla^2 \Psi = 0$ and $\nabla^2 \Phi = 0$. For a non-magnetic system, $\boldsymbol{\Psi}$ is an indeterminable constant that does not contribute to **E** as seen from Eq. 13a. Hence, although the governing equations for the electrostatic and wave problems are identical, their boundary conditions differ from each other.

As discussed in §2A, our EMT is based on estimating the conditionally averaged fields using an effective medium model shown in Fig. 1. Hence, $\langle \Theta(\mathbf{r}) | \mathbf{r}_1 \rangle$ and $\langle \Phi(\mathbf{r}) | \mathbf{r}_1 \rangle$ are obtained by the solution of Laplace equations for Θ and Φ subject to the boundary conditions given in Eqs. 13 and 15 respectively. In order to solve the Laplace problem, the unconditionally averaged far-field given by $\langle \mathbf{E} \rangle = \hat{\mathbf{x}} \exp(i\mathbf{k}_{eff} \cdot \mathbf{r})$ can be expressed in terms of the first Laplace harmonic in the following way. One may consider rotating the coordinate system in Fig. 1 about the y-axis such that $\hat{\mathbf{x}}$ is replaced by $\hat{\mathbf{z}}$ and hence **E** points in the direction of the zenith. Since, $\mathbf{r} = \mathbf{r}_1 + \mathbf{r}'$, $\exp(i\mathbf{k}_{eff} \cdot \mathbf{r}) \to \exp(i\mathbf{k}_{eff} \cdot \mathbf{r}_1)$ as $r' \to 0$. Hence, far field scalar potentials $\langle \Theta \rangle$ and $\langle \Phi \rangle = \exp(i\mathbf{k}_{eff} \cdot \mathbf{r}_1) r' \cos\theta$. $\langle \mathbf{E}(\mathbf{r}) | \mathbf{r}_1 \rangle$ and $\langle \mathbf{E}_S(\mathbf{r}) | \mathbf{r}_1 \rangle$ are given by $\nabla \langle \Theta(\mathbf{r}) | \mathbf{r}_1 \rangle$ and $\nabla \langle \Phi(\mathbf{r}) | \mathbf{r}_1 \rangle$ respectively. We find that the coefficient of the first regular harmonic is identical for Θ and Φ and consequently $\langle \mathbf{E}(\mathbf{r}) | \mathbf{r}_1 \rangle = \langle \mathbf{E}_S(\mathbf{r}) | \mathbf{r}_1 \rangle$

$$= \exp(i\mathbf{k}_{eff} \cdot \mathbf{r}_1) \frac{3\varepsilon_m}{\varepsilon_p + 2\varepsilon_m} \hat{\mathbf{z}}, \; r' < a \tag{5.16}$$

for a sphere in an infinite matrix. A similar procedure can be employed to show that

$$\langle \mathbf{E}_S(\mathbf{r}) | \mathbf{r}_1 \rangle = \exp(i\mathbf{k}_{eff} \cdot \mathbf{r}_1) \frac{9\varepsilon_m \varepsilon_{eff}}{(\varepsilon_p + 2\varepsilon_m)(2\varepsilon_{eff} + \varepsilon_m) - 2\kappa^{-3}(\varepsilon_p - \varepsilon_m)(\varepsilon_{eff} - \varepsilon_m)} \hat{\mathbf{z}}, \; r' < a \tag{5.17}$$

for a sphere an *effective medium* shown in Fig. 1. The exponential term in Eqs. 16 and 17 is a phase factor that depends on the location of the sphere. Eqs 4, 5 and 6 can be used in that order to obtain an expression for ε_{eff}. Required algebraic manipulations are discussed in §3B below. Exact expressions for ε_{eff} are presented §4A.

5.3.2 Vector EMT

The determination of $\langle \mathbf{E}(\mathbf{r}) | \mathbf{r}_1 \rangle$ for a finitely large value of *ka* requires the solution of the vector Helmholtz equation for a 2-layer sphere geometry shown in Fig. 1. **E** inside a particle can be found by utilizing a multipole expansion. The solution given by Hightower and Richardson [74] was adapted here to obtain the following relations for $\langle \mathbf{E}(\mathbf{r}) | \mathbf{r}_1 \rangle$ for $r' < a$:

$$\langle E_r(\mathbf{r}) \mid \mathbf{r}_1 \rangle = \exp(i\,\mathbf{k}_{eff} \cdot \mathbf{r}_1) \frac{-i \sin\theta' \cos\phi'}{k_p^2 r'^2} \sum_{n=1}^{\infty} d_n\, i^n (2n+1)\, \pi_n(\theta')\, \psi_n(k_p r'), \tag{5.18a}$$

$$\begin{aligned} \langle E_\theta(\mathbf{r}) \mid \mathbf{r}_1 \rangle &= \exp(i\mathbf{k}_{eff} \cdot \mathbf{r}_1) \frac{\cos\phi'}{k_p\, r'} \\ &\times \sum_{n=1}^{\infty} i^n \frac{(2n+1)}{n(n+1)} [c_n\, \pi_n(\theta')\, \psi_n(k_p r') - i\, d_n\, \tau_n(\theta')\, \psi_n'(k_p r')] \end{aligned} \tag{5.18b}$$

and

$$\begin{aligned} \langle E_\phi(\mathbf{r}) \mid \mathbf{r}_1 \rangle &= \exp(i\mathbf{k}_{eff} \cdot \mathbf{r}_1) \frac{\sin\phi'}{k_p\, r'} \\ &\times \sum_{n=1}^{\infty} -i^n \frac{(2n+1)}{n(n+1)} [c_n\, \tau_n(\theta')\, \psi_n(k_p r') - i\, d_n\, \pi_n(\theta')\, \psi_n'(k_p r')]. \end{aligned} \tag{5.18c}$$

In Eqs. 18a-c, primed coordinates (r', θ', ϕ') are with respect to the origin *O'*, *n* is the order of the multipole, $\pi_n = \dfrac{P_n^1(\cos\theta)}{\sin\theta}$ and $\tau_n = \dfrac{dP_n^1(\cos\theta)}{d\theta}$ are the polar angle dependent functions related to the associated Legendre polynomials P_n^1 of degree one, $\psi_n(z) \equiv z j_n(z)$ are Riccati-Bessel functions associated with the spherical Bessel functions $j_n(z)$ and c_n and d_n are the corresponding

Mie coefficients [56]. The expressions of c_n and d_n are given in Appendix A. In general, both c_n and d_n are functions of a and k_{eff} [56].

Bessel functions and their derivatives were calculated using established iterative techniques [18]. The volume integral of $\langle \mathbf{E}(\mathbf{r}) | \mathbf{r}_1 \rangle$ over the particle volume was determined to evaluate $\langle g_p \mathbf{E} \rangle$ and subsequently Ω using Eqs. 4 and 5. Phase factors $\exp(i\mathbf{k}_{eff} \cdot \mathbf{r}_1)$ in Eqs. 18 were expressed as $\exp(i\mathbf{k}_{eff} \cdot \mathbf{r}) \exp(-i\mathbf{k}_{eff} \cdot \mathbf{r}')$ so that $\exp(i\mathbf{k}_{eff} \cdot \mathbf{r})$ in the right-hand side of Eq. 5 would cancel out with the left-hand side. A two dimensional composite Simpson's rule [75] was used since the analytical evaluation of the integral in Eq. 4 over r and θ was not possible due to the presence of the exponential term $\exp(-i\mathbf{k}_{eff} \cdot \mathbf{r}')$. Only the x-component of $\langle g_p \mathbf{E} \rangle$ was found to be non-zero, consistent with the isotropic nature of the effective medium. k_{eff} and equivalently ε_{eff} were calculated by finding the zeros of Λ in Eq. 7 using Newton-Raphson iterations. Since, Λ was not necessarily analytic in the complex variable k_{eff}, it was treated as a function of two variables which were the real and imaginary parts of k_{eff} necessitating the use of a two dimensional Newton-Raphson method [76]. For large ϕ, Eq. 8 permitted multiple solutions that were close to one other. Hence, the solution corresponding to the limit as $\phi \to 0$ was traced by using zero order continuation. The procedure was repeated for λ values in the visible range (300-800 nm). Permittivity data for noble metals was obtained from Ref. [11]. All computations were performed using MATLAB.

5.4 RESULTS AND DISCUSSION

5.4.1 Scalar EMT

In the limit as $\phi \to 0$, $\varepsilon_{eff} \to \varepsilon_m$. Hence, due to the absence of particle-effective medium coupling, $\langle \mathbf{E}(\mathbf{r}) | \mathbf{r}_1 \rangle$ is given by Eq. 16. The corresponding ε_{eff} is given by the following equation:

$$\varepsilon_{eff} / \varepsilon_m = 1 + 3\beta\phi, \quad \beta = \left(\frac{\varepsilon_p - \varepsilon_m}{\varepsilon_p + 2\varepsilon_m} \right). \tag{5.19}$$

Here, β is the electric polarizability per unit volume for a small sphere. As will be shown later in this section, the linear dependence shown in Eq. 19 is a general result that is independent of the mircostructure since β is a material property. In the case of a finitely large ϕ and arbitrary κ, $\langle \mathbf{E}(\mathbf{r}) | \mathbf{r}_1 \rangle$ is given by Eq. 17 for which ε_{eff} is found to be the following:

$$\varepsilon_{eff} / \varepsilon_m = 1 + \frac{9\varepsilon_{eff}}{(2\varepsilon_{eff} + \varepsilon_m) - 2\kappa^{-3}\beta(\varepsilon_{eff} - \varepsilon_m)} \gamma, \; \gamma \equiv \beta\phi. \tag{5.20}$$

For a well-separated system, $\kappa = \phi^{-1/3}$, which in conjunction with Eq. 20 gives the following result:

$$\varepsilon_{eff} / \varepsilon_m = \frac{1 + 2\gamma}{1 - \gamma} = 1 + 3\gamma + 3\gamma^2 + O(\gamma^3). \tag{5.21}$$

Eq. 21 is identical to the classical Maxwell-Garnett theory (MGT) which is also a scalar EMT in which the presence of other particles is accounted through the modification of the averaged far-

field [61, 77]. The lower bound, $\kappa = 1$, can be substituted in Eq. 20 to give the well-known Bruggeman mixing rule (BMR):

$$\phi\left(\frac{\varepsilon_p - \varepsilon_{eff}}{\varepsilon_p + 2\varepsilon_{eff}}\right) + (1-\phi)\left(\frac{\varepsilon_m - \varepsilon_{eff}}{\varepsilon_m + 2\varepsilon_{eff}}\right) = 0, \tag{5.22}$$

that is based on a symmetric mixing approach for the inclusions and matrix phase. As a consequence, BMR can model percolation effects [60]. A similar concentric-shell model with a variable shell thickness was also proposed by Hashin and Shtrikman [60]. However, the dependence of the shell thickness parameter κ on the microstructure was not demonstrated. MGT and BMR can be seen as the upper and lower Hashin-Strikman bounds of the scalar EMT. Garcia et al., among others, have derived self-consistent mixing rules for ternary plasmonic composites based on Hashin-Strikman formalism [13]. Within the framework of the EMT presented in this work, κ is a *physical parameter* that can be determined from the structure factor (or equivalently the radial distribution function) of the composite. Conversely, if κ were to be determined by fitting spectroscopic data to the EMT predictions, it can be used to glean microstructure information regarding the distribution of particles within the composite.

For a random system, κ can be expanded about $\phi = 0$ using Eqs. 9 and 11 to give $\kappa = 2 - \frac{4}{3}\phi + O(\phi^2)$. This can be substituted in Eq. 20 to obtain the following expansion for ε_{eff} valid for $\gamma << 1$:

$$\varepsilon_{eff} / \varepsilon_m = 1 + 3\gamma + \frac{3}{4}(\beta + 4)\gamma^2 + O(\gamma^3). \tag{5.23}$$

Note that all scalar EMTs based on Eq. 20 indeed yield $\varepsilon_{eff} = \varepsilon_p$ for $\phi = 1$.

5.4.1.1 Resonance conditions

A particle undergoes an electric resonance when $\langle \mathbf{E}(\mathbf{r}) | \mathbf{r}_1 \rangle$ is singular. For a finitely large ϕ, however, a different resonance condition that takes into account the particle-effective medium coupling effect will result. Hence, in this section, a discussion on the conditions under which scalar ε_{eff} shows a resonance is presented.

Resonance of a single sphere requires that

$$|\beta| \to \infty, \text{ or equivalently, } \varepsilon_p = -2\varepsilon_m \tag{5.24}$$

as can seen from Eqs. 16 and 19. Presence of an effective medium, on the other hand, leads to a condition that the denominator in Eqs. 17 and 20 vanish. Hence, one obtains a resonance condition given by:

$$2\beta\left(\frac{\varepsilon_{eff}-1}{2\varepsilon_{eff}+1}\right) = \kappa^3. \tag{5.25}$$

In the specific case of a well-separated system (or MGT), substitution of $\kappa = \phi^{-1/3}$ in Eq. 25 gives the following resonance condition:

$$\beta \approx \frac{1}{\phi}. \tag{5.26}$$

The above equation can also be obtained by letting the denominator in Eq. 21 to be zero. Similar to the way by which Eq. 26 was obtained, a substitution of $\kappa = 2 - \frac{4}{3}\phi + O(\phi^2)$ in Eq. 25 under

the limit as $\gamma \to 0$, leads to the following resonance condition for random hard-sphere composites:

$$\beta \approx \frac{2}{\sqrt{\phi}}. \tag{5.27}$$

As seen from Eqs. 26 and 27, for dense systems the resonance wavelength is different from that of a single particle. Hence, the scaling of β with ϕ depends on the microstructure of the system through the static structure factor. This trend is consistent with the reported red-shift in plasmon resonance for ion-implanted composites [51]. We note that substitution of $\kappa = 1$ in Eq. 25 in the limit as $\gamma \to 0$ gives the resonance condition in the 'Bruggeman limit' as $\beta \approx 1/2\sqrt{\phi}$.

Since the equations for dense systems (Eqs. 17, 20 and 24) include particle-effective medium coupling, they are implicit in ε_{eff}. Conversely, the inverse problem, i.e. when ε_{eff} is given and ε_p or ϕ are unknown, is explicit in all cases. Hereafter, we only consider the solution of Eq. 20 that approaches unity as $\phi \to 0$.

5.4.1.2 Ag Plasmonic composite

Resonant plasmonic nanospheres made of noble metals such as Ag, Au and Cu have an ε_p that has a large negative real part and a small positive imaginary part for the visible range of the electromagnetic spectrum as shown in Fig. 2. Their β values show a resonance as a consequence. We consider Ag in our further discussion since it has the smallest $\mathrm{Im}[\varepsilon_p]$ over a broad wavelength range and hence the most prominent β. Further, a medium with a relatively large ε_m can shift this resonance to the red region and make it more prominent. For this work we

will consider $\varepsilon_m = 7$. Semiconductors such as ZnO, Si, TiO_2 etc. have similar values of ε_m.

Values of β for Ag spheres in an $\varepsilon_m = 7$ medium are shown in Fig. 3.

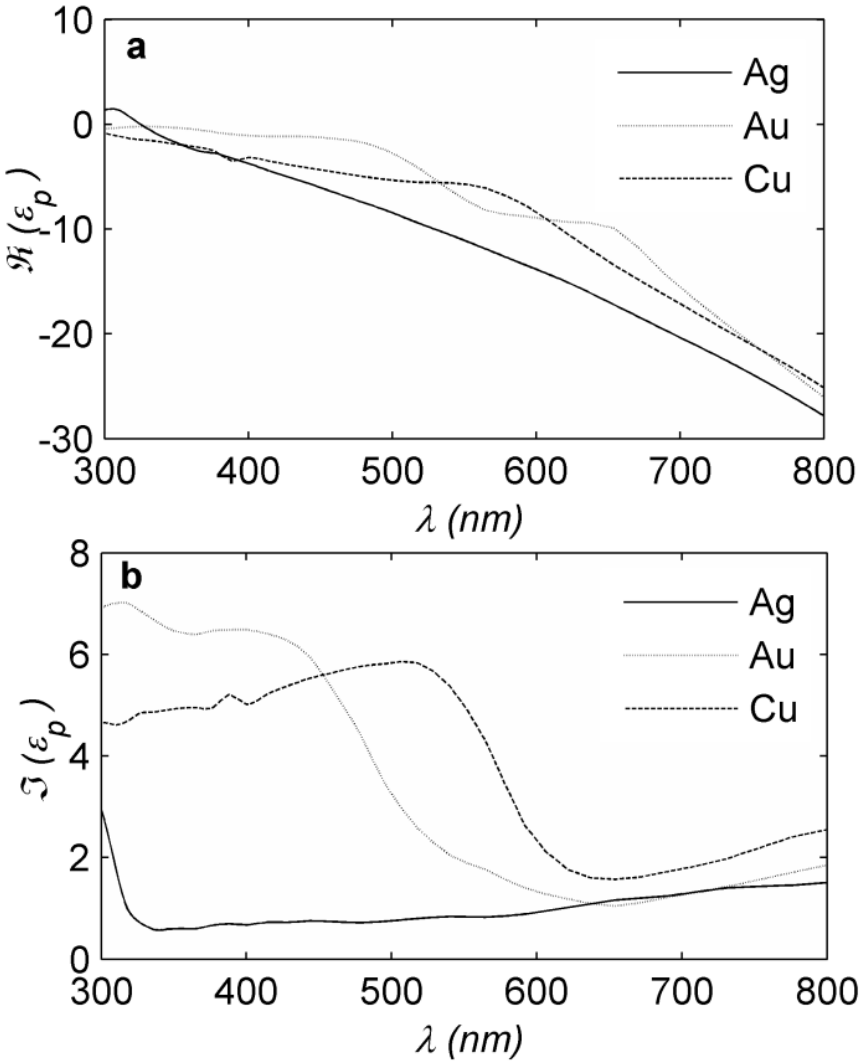

Figure 5.2: Real and imaginary parts of the permittivity of high optical conductivity metals Ag, Au and Cu that are considered in this work. Permittivity data is taken from Ref. [11]. Ag has the lowest imaginary permittivity over a broad range of wavelengths.

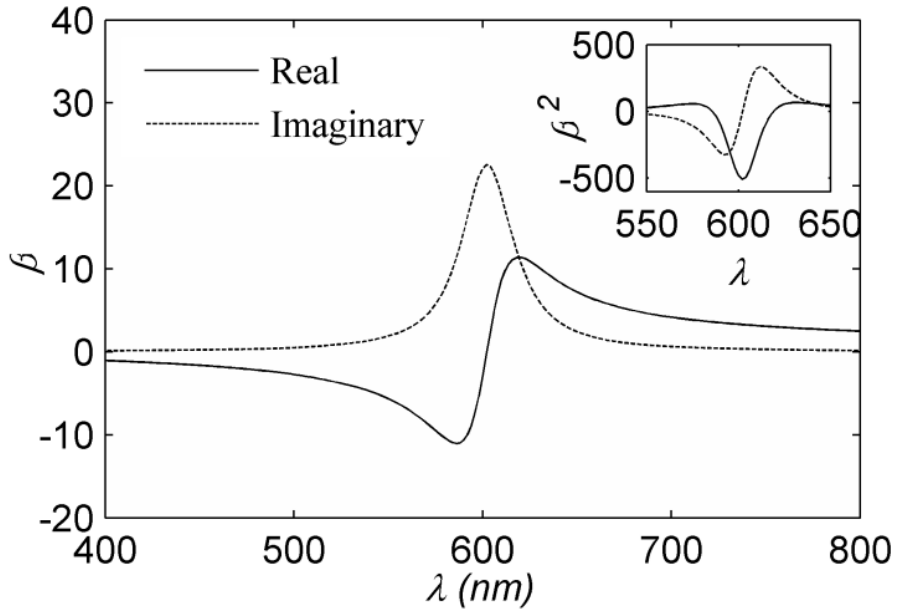

Figure 5.3: β for Ag spheres in a $\varepsilon_m = 7$ medium. Resonance occurs for $\lambda \approx 600$ nm and $\beta \approx 23i$. $\Im(\beta)$ is a small number away from resonance and $\Re(\beta)$ changes sign from negative to positive on moving from blue to red regions about resonance.

The permittivity of high conductivity metals such as Ag can be evaluated approximately by using the Drude model given by $\varepsilon_p = 1 - \dfrac{\omega_p^2}{\omega^2 + i\omega\omega_c}$ [1]. Here, plasma frequency $\omega_p \approx 2.321\times10^{15}$ Hz and collision frequency $\omega_c \approx 5.513\times10^{12}$ Hz for Ag in the visible range [78]. The peak in $\Im(\beta)$ occurs at the resonance frequency given by $\omega_R = \dfrac{\omega_p}{\sqrt{2\varepsilon_m + 1}}$ or equivalently resonance wavelength $\lambda_R = \dfrac{2\pi c\sqrt{2\varepsilon_m + 1}}{\omega_p}$ where *c* is the speed of light in vacuum. Hence, the resonance wavelength for small spheres scales as $\sqrt{2\varepsilon_m + 1}$ resulting in a red-shift as ε_m is increased. The peak value β_R at resonance is given by $\beta_R = -\left(\dfrac{\varepsilon_m - 1}{2\varepsilon_m + 1}\right) + i\dfrac{\omega_p}{\omega_c}\dfrac{3\varepsilon_m}{(2\varepsilon_m + 1)^{3/2}}$ for a Drude metal.

The real and imaginary parts of β represent the reactive and dissipative components respectively. At resonance ($\lambda \approx 600$ nm), $\Im(\beta)$ is a large positive number and $\Re(\beta) = 0$ as shown in Fig. 3. As $|\gamma| \to 0$, the dissipative term for all scalar EMTs is given by $\Im(\varepsilon_{eff} / \varepsilon_m) \approx 3\phi\,\Im(\beta)$. The quadratic term for random systems is $-\frac{3}{4}[\Im(\beta)]^3\phi^2$. As a result, $\Im(\varepsilon_{eff})$ is highly non-linear in ϕ. For β shown in Fig. 3, $\Im(\varepsilon_{eff} / \varepsilon_m) \approx 69\phi - 9125.25\phi^2$ at resonance. In contrast, it is identically zero for a well-separated composite. Hence, quadratic coupling does not lead to any loss in a well-separated composite. $\Re(\varepsilon_{eff} / \varepsilon_m)$ is identically one under resonance for a random system. Hence, the reaction originates only from the medium. For a well-separated system, quadratic and even powered coupling contributes to the reaction such that $\Re(\varepsilon_{eff} / \varepsilon_m) \approx 1 - 3[\Im(\beta)\phi]^2$.

At off-resonance, $\Re(\beta)$ is greater than zero for $\lambda > \lambda_R$ and less than zero for $\lambda < \lambda_R$. $\Im(\beta)$ is smaller in comparison for the most part. For instance, at $\lambda \approx 680$ nm, $\beta = 4.973 + 0.973i$; and at $\lambda \approx 520$ nm, $\beta = -3.546 + 0.816i$. The red-regions exhibit a "concentration resonance" which occurs when the resonance condition given in Eq. 24 is satisfied. In case of a well-separated system, the condition is $\beta\phi = 1$ and for a random system, it is $\beta^2\phi \approx 4$ as given in Eqs. 25 and 26. Fig. 4 shows $\Im(\varepsilon_{eff} / \varepsilon_m)$ as a function of ϕ for $\lambda \approx 680$ nm. A peak appears at $\phi \approx 13\%$ for a random system and at $\phi \approx 20\%$ for a well-separated system. The peak for a random system is less prominent compared to that for a well-separated system. The resonance concentration shifts to higher values of ϕ as ε_m is decreased.

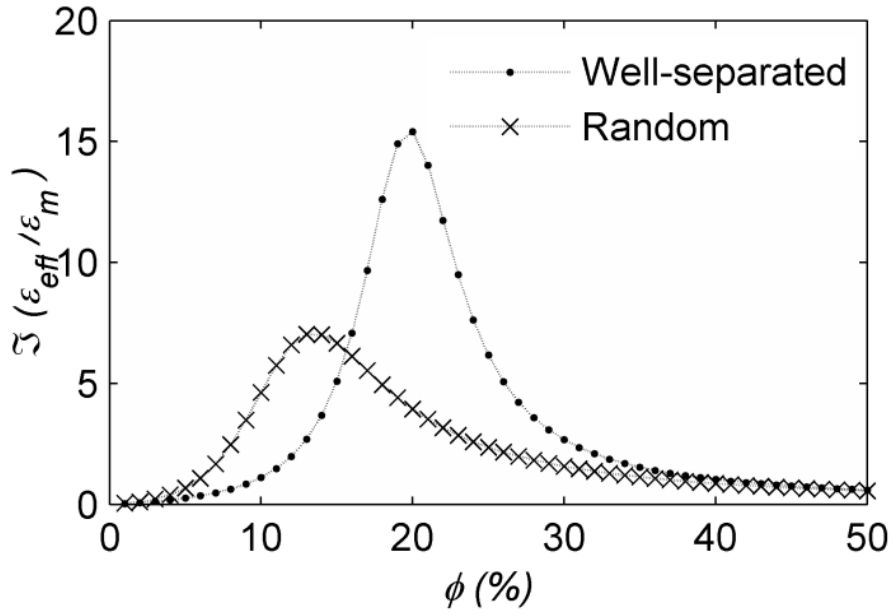

Figure 5.4: $\Im(\varepsilon_{eff})$ predicted by the scalar EMT for random and well-separated microstructures. Here, $\lambda \approx 680$ nm and $\beta = 4.973 + 0.973i$. β has a resonance peak at $\lambda \approx 600$ nm as shown in Fig. 3.

Fig.5.5 shows the effect of ϕ on ε_{eff}. It is evident that a well-separated system couples more intensely with the incident field as compared to a random one. Peaks corresponding to random systems occur for λ values that are larger than those for well-separated systems due to the difference in the scaling of β with respect to ϕ under resonance as shown in Eqs. 26 and 27. The quadratic coefficient for a random system is $\frac{3}{4}\beta^3 + 3\beta^2$ (Eq. 22) in comparison to $3\beta^2$ (Eq. 21) for a well-separated system. The coefficients of the cubic and higher order terms in ϕ also depend on higher powers of β for a random system. Hence, the resonance condition for the coefficient of the quadratic term in the power series expansion of $\varepsilon_{eff}(\phi)$ will depend on that of the linear term while the resonance condition for cubic coefficient will depend on those of the

quadratic and linear terms, etc. As a consequence, the peak in $\Im(\varepsilon_{eff})$ for random systems is not symmetric about its maximum and is broader in comparison to that for a well-separated system or a single sphere.

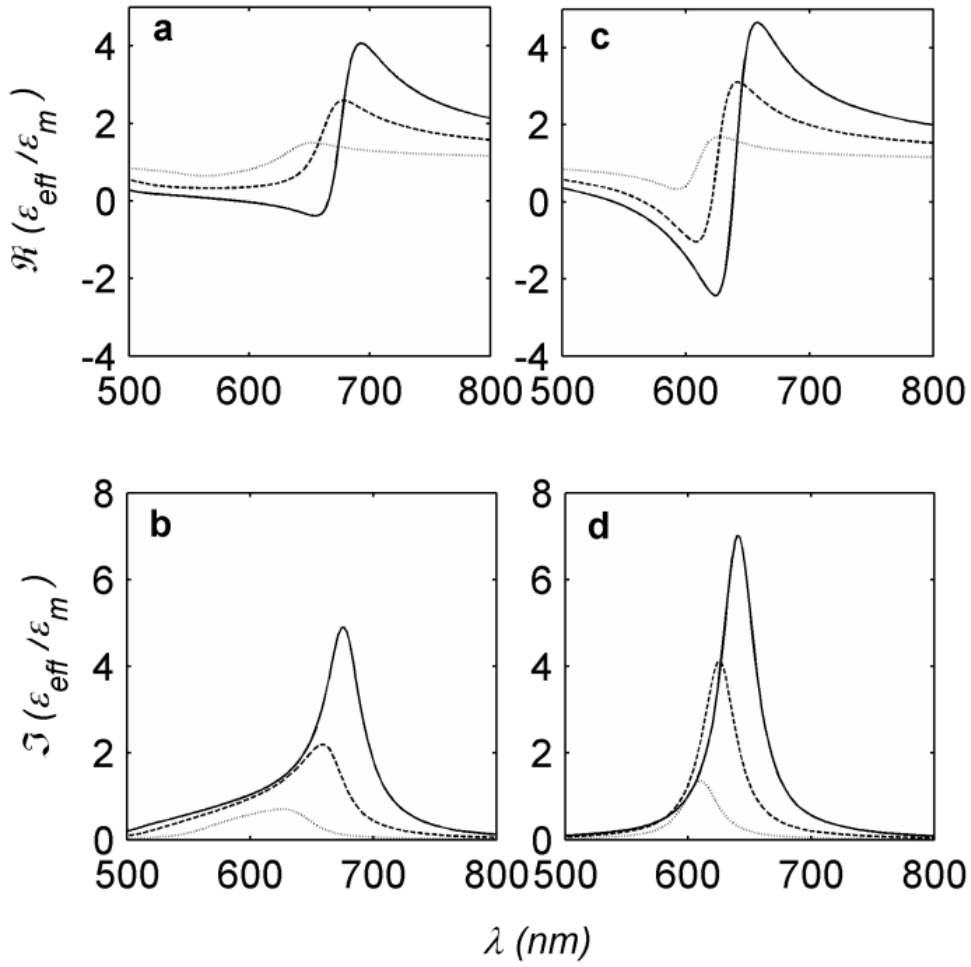

Figure 5.5: ε_{eff} for a composite with Ag NPs in an $\varepsilon_m = 7$ medium calculated with the scalar EMT. Random (a, b) and well-separated random composites (c, d) for $\phi = 2\%$ (solid), 6% (dashed) and 10% (dotted) were considered. The resonance peak is more red-shifted and broad for a random system. A well separated system shows a more intense resonance with a symmetric peak in comparison. Stronger coupling in a random system leads to a tail in the blue region.

5.4.2 Vector EMT

This section describes the effect of *ka* on numerically calculated values of ε_{eff} . An analysis of vector EMT in the limit as $\phi \to 0$ and $ka \to 0$ is first presented. Resonance analysis in the limit as $\phi \to 0$ is presented in §4B-I followed by a discussion on the numerical results for finitely large ϕ and ka will follow in §4B-II.

In the vector EMT, $\langle \mathbf{E}(\mathbf{r}) | \mathbf{r}_1 \rangle$ is not a constant vector but depends on the toroidal (corresponding to coefficients c_n) and poloidal (corresponding to coefficients d_n) multipoles shown in Eqs. 18. Only poloidal modes are capable of generating $\langle E_r | \mathbf{r}_1 \rangle$ which only toroidal modes generate $\langle H_r | \mathbf{r}_1 \rangle$. Hence, we will refer to the poloidal modes as the electric modes and the toroidal modes as magnetic modes following the standard convention [17].

For subsequent analysis, the following expansion is used to express the dependence of ε_{eff} on ϕ

$$\varepsilon_{eff} / \varepsilon_m = 1 + A\phi + B\phi^2 + O(\phi^3). \tag{5.28}$$

As in §3A, only the linear and quadratic coefficients are of interest here. Coefficients *A* and *B* in Eq. 28 depend on *ka*, ε_p, and ε_m. Riccati-Bessel functions in Eqs. 18 can be expanded into a Taylor series as $\psi_n(z) = C_n z^{n+1} + O(z^{n+3})$ where $C_n = \dfrac{\sqrt{\pi}}{4\Gamma(n+3/2)}$, where Γ denotes the gamma function. Hence, as $z \to 0$ or equivalently $k_p a \to 0$, the terms corresponding the c_1 mode in Eqs. 18 are $O(z)$, while those corresponding to the d_1 mode are $O(1)$. As a result, only the d_1 term contributes significantly as $z \to 0$. In the limit as $\phi \to 0$, only the linear coefficient *A*

in Eq. 28 is relevant irrespective of the microstructure. $\langle \mathbf{E}(\mathbf{r}) | \mathbf{r}_1 \rangle$ from Eqs. 18 can be used together with Eq. 4 and 5 to obtain the parameter Ω. It can be shown that $\Omega = d_1$ and as $k_p a \to 0$, where d_1 is given by $d_1 = \frac{3}{(\varepsilon_p + 2)}\left[1 + i\frac{2}{3}\beta(k^* a)^3\right] + O\left[(k^* a)^6\right]$. Subsequently, *A* can obtained by using Eq. 6 as:

$$A = 3\beta + i2\beta^2(k^* a)^3 + O\left[(k^* a)^6\right], \tag{5.29}$$

where, $k^* = k_p / n_{eff}$. Note that as $\phi \to 0$, $n_{eff} \to n_m$ and hence, k^* can be modified appropriately in the dilute limit. Mallet et al. [62] have recently re-derived MGT for finitely large particles that can exhibit scattering using rigorous Foldy-Lax multiple scattering equations (see Eq. 22 in [62]). The linear term is identical to the one obtained here in Eq. 29. The cubic dependence on the particle radius implies that the size effect becomes significant only when $\left|\beta^2(k^* a)^3\right|$ is $O(1)$. Since β^2 is a large negative number at resonance as shown in Fig. 3 inset, size effects become significant even for relatively small radii for resonant systems. For example $\left|\beta^2\right| = 500$ at resonance for an Ag sphere shown in Fig. 3. Hence, $\left|\beta^2(k^* a)^3\right| = 1/2$ for $\left|k^* a\right| \approx 0.063$. Here, since $k^* = 0.0005 + 0.0147i$ nm^{-1}, a relatively small radius of $a \approx 34$ nm can significantly affect ε_{eff} even in the dilute limit.

5.4.2.1 Resonance conditions

Resonance occurs when $\langle \mathbf{E}(\mathbf{r}) | \mathbf{r}_1 \rangle$ given by Eqs. 18 is singular. In turn, this requires that the coefficients c_n and d_n are singular. Magnetic resonances represented by singular c_ns do not

occur in plasmonic systems since $\mu_p = \mu_m = \mu_0$. Vector EMT exhibits only electric multipole resonances that correspond to d_n that are given in Appendix A. The conditions are complicated for Helmholtz multipoles as they involve the Riccati-Bessel functions. However, the underlying physical aspects can be appreciated by utilizing the simpler Laplace multipoles [79]. The n^{th} Laplace multipole has a size independent polarizability β_n defined as:

$$\beta_n \equiv \frac{\varepsilon_p - \varepsilon_m}{\varepsilon_p + \frac{n+1}{n}\varepsilon_m}. \tag{5.30}$$

A dipole resonance requires that $\beta_1 \to \infty$ or equivalently $\varepsilon_p = -2\varepsilon_m$; quadrupole resonance occurs when $\beta_2 \to \infty$ or $\varepsilon_p = -\frac{3}{2}\varepsilon_m$ and so on [53]. Hence, higher order multipoles become resonant at smaller negative values of ε_p, or equivalently for smaller values of λ as inferred from the ε_p - λ curve shown in Fig. 2. Mie coefficients A_n, a_n and d_n are polynomials of k^*a and β_n in the limit as $k^*a \to 0$ such that higher order β_n become significant only for an $O(1)$ k^*a [2, 56]. For an arbitrary k^*a, Helmholtz multipole electric polarizabilities d_n depend on k^*a [2] such that their resonance peak red-shifts with k^*a. Hence, both *A* and *B* red-shift as k^*a increases.

The above mentioned physical trends in the resonance conditions are also seen in the numerical results obtained for the vector EMT. Fig. 6 shows *A* as a function of λ for diameters d_p = 10, 30, 50 and 100 nm. Here, $k^*a \approx \frac{0.45 d_p \sqrt{\varepsilon_p}}{\lambda}$, where d_p and λ are in nm. *A* was calculated by fitting the data for ε_{eff} obtained for $\phi = 0.01\%$ to Eq. 28 as:

$$A = \frac{1}{\phi}\left(\frac{\varepsilon_{eff}}{\varepsilon_m} - 1\right). \tag{5.31}$$

For a small value of d_p such as 10 nm, only the dipole mode is significant. Hence, $A = 3\beta$. Relatively larger particles, e.g. d_p = 50 nm, show a significant quadrupole resonance. The dotted curves in Fig. 6 shows a quadrupole peak at $\lambda \approx 580$ nm. A further larger d_p = 100 nm results in an octupole peak as depicted in the insets of Fig. 6. Each peak red-shifts for larger d_p. For example, the quadrupole peak for d_p = 100 nm occurs at $\lambda \approx 650$ nm. **E** becomes highly localized at the particle surface for relatively large $k^* a$ values. Consequently, the magnitude of A and ε_{eff} are diminished for relatively large d_p values as shown in Fig. 6. In the large size limit ($k^* a \to \infty$), A = 0. Further an inspection of Eqs. 3 and 18 shows that $\varepsilon_{eff} = \varepsilon_m$ for arbitrarily large ϕ, in the limit as $k^* a \to \infty$. This is consistent with the ray optics scenario.

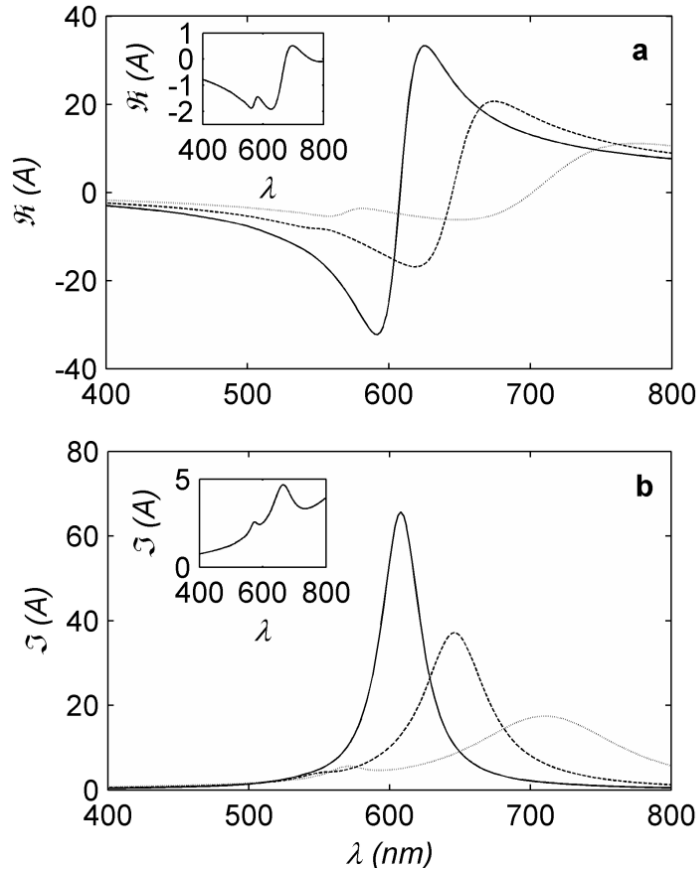

Figure 5.6: Linear coefficient *A* for composites in an $\varepsilon_m = 7$ matrix with Ag NPs with diameters $d_p = 10$ (solid), 30 (dashed), 50 (dotted) and 100 nm (inset). Here, $k^* a \approx \frac{0.45 d_p \sqrt{\varepsilon_p}}{\lambda} < 1$ only for the blue curve. Quadrupolar and octupolar resonance peaks are present for large particles as seen in the curves in the insets. Dipole resonance is most prominent and red-shifts as d_p is increased. The linear coefficient becomes less significant for large particles as they screen most of the E field from their interior.

By neglecting cubic and higher order terms in Eq. 28, the coefficient *B* was obtained using the following expression with $\phi = 1\%$:

$$B = \frac{1}{\phi^2}\left(\frac{\varepsilon_{eff}}{\varepsilon_m} - 1 - A\phi\right). \tag{5.32}$$

Fig. 7 shows the values of *B* calculated for random (κ given by Eqs. 9 and 11) and well-separated ($\kappa = \phi^{-1/3}$) random systems. *B* represents the strength of interparticle coupling. Hence, random systems have a larger *B*. The n^{th} multipole decay as $r^{-(n+2)}$ in general. Hence, dipoles can couple most strongly due to a r^{-3} dependence while higher order multipoles such as quadrupole and octupole couple weakly. The dotted ($d_p = 30$ nm) and dashed ($d_p = 50$ nm) curves and the solid curve in the inset ($d_p = 100$ nm) in Fig. 7 have a lower magnitude in comparison to the solid curve as a result. In fig. 7b, the solid curve for $d_p = 10$ nm shows a prominent radiant peak for $\lambda \approx 610$ nm with $\Im(B) \approx -3000$. For larger particles such as the ones with $d_p =$ 30 and 50 nm, peak values of $\Im(B)$ are greatly diminished due to reduced coupling. Hence, the dashed curves in Fig. 7b, have a peak at ~ -900 and the dotted curve at ~ -100. The corresponding *A* values do not vary proportionately as can be seen from Fig. 6. Hence, linear approximation is appropriate only for large d_p values. This is not surprising since for a given ϕ, increasing d_p results in reducing particle number density, and consequently interparticle coupling. The linear approximation is also applicable to well-separated systems since they have small values of *B* in comparison to a random system. A maximum in $\Im(B)$ also occurs upon increasing d_p while keeping ϕ and λ constant leading to a size resonance. Thus, ε_{eff} exhibits resonances as a function of all system parameters.

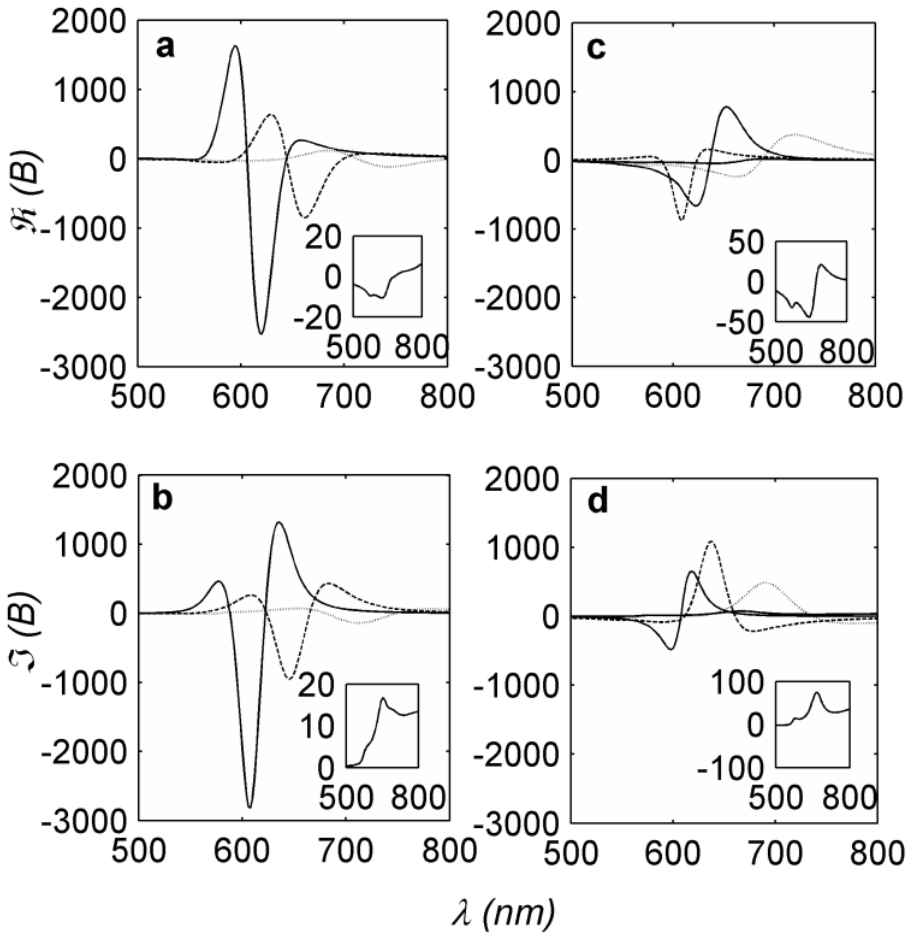

Figure 5.7: Quadratic coefficient *B* calculated for random (a, b) and well-separated random (c, d) composites in an $\varepsilon_m = 7$ matrix containing Ag NPs with diameters $d_p = 10$ (solid), 30 (dashed), 50 (dotted) and 100 nm (inset). Here, $k^* a \approx \dfrac{0.45 d_p \sqrt{\varepsilon_p}}{\lambda} < 1$ is less than one only for the solid curve that is given by $\dfrac{3}{4}(\beta + 4)\beta^2$ for (a) and (b); and $3\beta^2$ for (c) and (d). Weak coupling in well-separated random systems leads to a smaller *B* in comparison to random systems.

5.4.2.2 Fano Resonance

High conductivity metals are typically described by adding to the Drude model a number of Lorentz oscillators that capture effects of lattice polarizability and inter-band and intra-band electron transitions [80]. The Lorentz model is based on a damped harmonic oscillator with finite

mass. The Drude model, however, does not include the harmonic force and hence is able to model free electrons well. The Lorentz model predicts a symmetric profile for the intensity vs. frequency curve for systems with a small damping. Interestingly, β that is based on a Drude model for ε_p has a lineshape of a Lorentz oscillator. Hence, a single plasmonic particle is a Lorentz oscillator. In the limit as $\phi \to 0$, the susceptibility of the effective medium is given by $\chi_{eff} = \varepsilon_{eff} / \varepsilon_m - 1 = 3\beta\phi + O(\phi^2)$. Hence, the effective medium is also a Lorentz oscillator in the limit as $\phi \to 0$. However, the coupling between the particle and the effective medium becomes stronger, i.e., for large ϕ or small κ, ε_{eff} can be expected to possess the characteristics of a coupled oscillator system which deviates from the Lorentzian symmetric lineshape. It is well-known that an unusual lineshape that is asymmetric about the extremum, known as Fano resonance, is observed in resonant coupled oscillator systems such as plasmonic nanostructures [10-12, 81].

Within the framework of the EMT presented here, for a given ϕ, κ represents the extent of coupling between the particle and the effective medium. Consequently, ε_{eff} - λ curves show unusual resonance shapes for relatively small values of κ. Fig. 8 shows a plot of ε_{eff} for Ag NP composite in an $\varepsilon_m = 7$ matrix for $\phi = 5\%$. The scalar EMT was used in the calculations. Hence, the results are representative of those for small particles. For random systems, κ has two bounds: an upper bound given by $\kappa = \phi^{-1/3}$ for a system with well-separated particles and a lower one given by $\kappa = 1$ representing a locally dense composite, which we refer to as the Bruggeman limit. Close to the upper bound, the particle-effective medium coupling is relatively weak resulting in a symmetric Lorentzian ε_{eff} even for relatively large ϕ. This can be seen in the

shape of the solid curve in Fig. 8. The dashed curve in Fig. 9 is the locus for the upper bound in the κ-ϕ space. Black circles in Fig. 9 denote the locations at which the shape of ε_{eff} - λ curve is Lorentzian. As κ is reduced, the shapes of the curves become distorted due to increased coupling. The resonance location shifts to larger values of λ and the resonant peak becomes broader. $\Im(\varepsilon_{eff}/\varepsilon_m)$ has an asymmetric shape for intermediate values of κ as shown in dashed curves in Fig. 8. The κ-ϕ space locations for which an asymmetric response is predicted are shown in Fig. 9 as grey circles. For κ values that are close to unity, $\Im(\varepsilon_{eff}/\varepsilon_m)$ curve becomes very broad as can be seen from the dotted lines in Fig. 8. Unfilled circles in Fig. 9 represent this type of response. The trends in Figs. 8 and 9 are also present in composites with a finitely large *ka*.

Fano resonance can also be understood as the interference between the absorbing and radiating modes in plasmonic structures [10, 81]. Our analysis in the limit as $\phi \to 0$ suggests that the interference manifests through the Taylor coefficients of ε_{eff}. A negative extreme in the imaginary quadratic coefficient $\Im(B)$ (Fig. 7b and d), for example, represents a coupled "radiating mode" that is present in conjunction with the "absorbing mode" of a single particle given by a positive $\Im(A)$ (Fig. 6b).

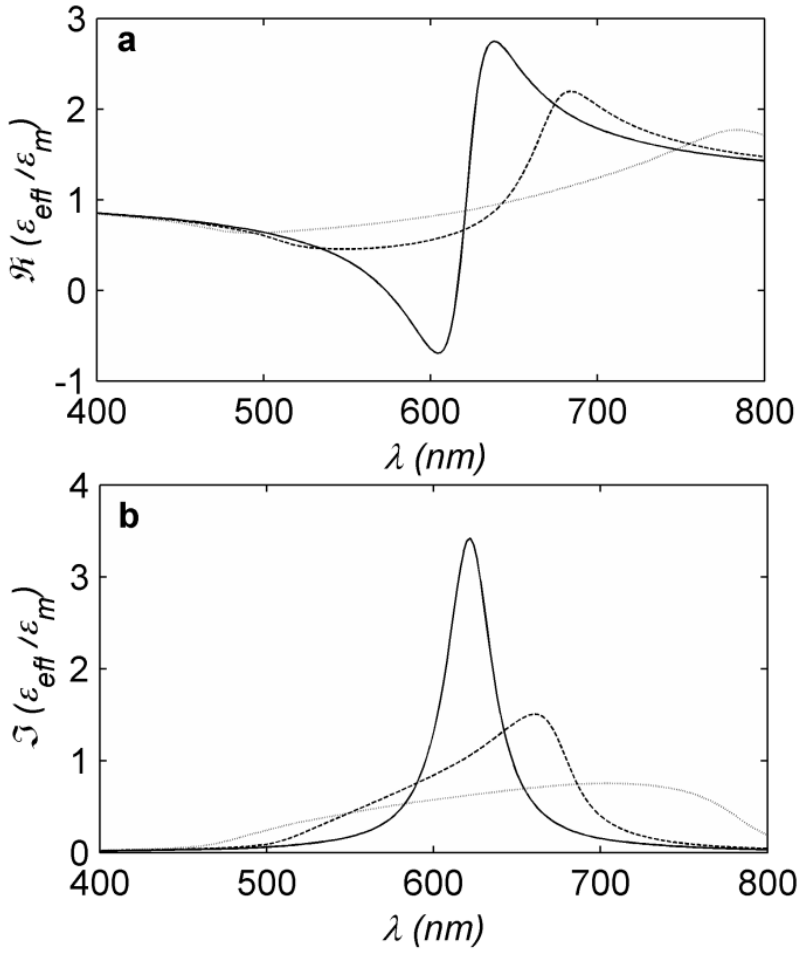

Figure 5.8: Effect of κ on ε_{eff} for $\phi = 5\%$. Microstructures with $\kappa = \phi^{-1/3} \approx 2.71$ (solid curve), $\kappa \approx 1.75$ (dashed curve) and $\kappa \approx 1.25$ (dotted curve). Small values of κ lead to a stronger coupling that distorts the Lorentzian shape of ε_{eff} even for relatively small values of ϕ such as 5%. Calculations were performed with the scalar EMT.

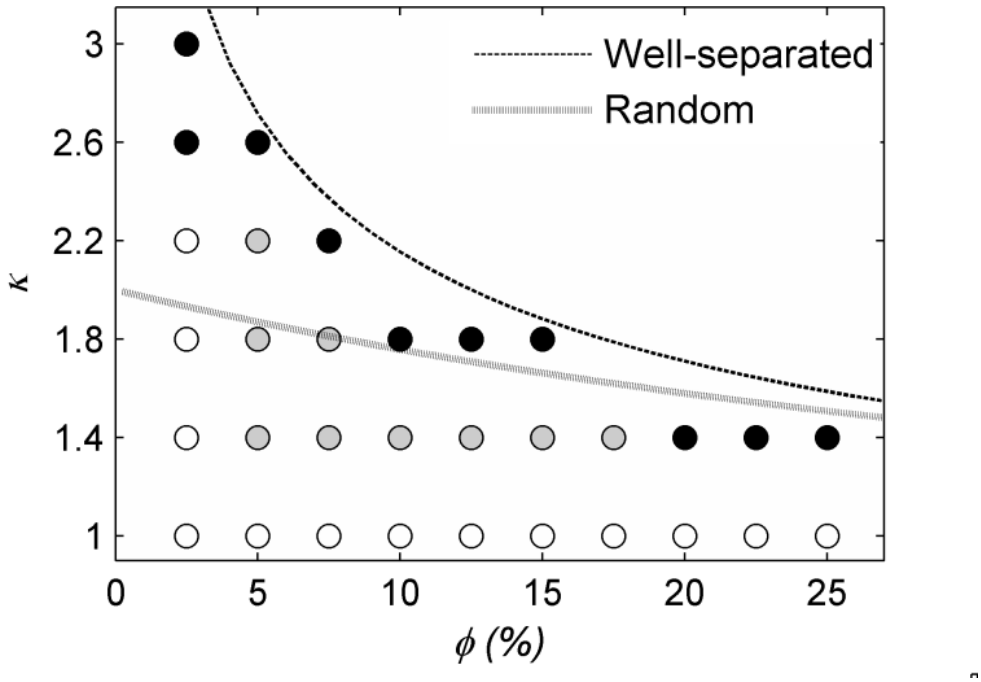

Figure 5.9: Characterization of the dielectric response of a random plasmonic composite in the κ - ϕ space. The dashed line represents the upper bound for a random composite with well-separated particles and the grey dotted line represents a random hard sphere composite. Locations of Lorentzian and Fano responses are shown in black and grey circles respectively. Unfilled circles denote locations in which broad lineshapes are observed.

5.5 CONCLUSIONS

Plasmonic nanoparticles undergo an electric resonance when their electric dipole polarizability β is a large positive imaginary number. As a result, the particles absorb intensely. For a relatively large volume fraction ϕ and/or when particle size is comparable to that of the exciting wavelength, interparticle coupling becomes important. Consequently, the effective permittivity ε_{eff} can no longer be treated as the sum of the polarizabilities of the individual particles and, hence does not vary linearly with ϕ. Hence, quadratic and higher order effects in ϕ on the polarizability have to be determined to obtain accurate predictions of ε_{eff}.

In this work, we have developed an EMT to account for such nonlinear effects on the effective permittivity of dense random dispersions of equi-sized spheres of high optical-conductivity metals such as Ag, Au and Cu. The EMT is based on the idea that the region surrounding a given particle in a composite can be modeled as an effective continuum that begins after a distance $R=\kappa a$ from the centre of the particle (κ >1). Within this framework, κ is interpreted as a microstructure parameter that correlates with the static structure factor of the composite. For a homogenous random composite, κ is bounded such that $1<\kappa<\phi^{-1/3}$. The upper bound corresponds to a well-separated random system that can be modeled as a Maxwell-Garnett composite. The lower bound corresponds to Bruggeman's mixing rule which, as in the case of MGT, is based on the electrostatic approximation [60]. In general, a random hard-sphere microstructure would have a κ value that lies in between these two bounds, which, in principle can be determined from the knowledge of the radial distribution function. Hence κ is a *physical* rather than an adjustable fitting parameter. Conversely, if κ were to be determined by fitting

spectroscopic data to the EMT predictions, it can be used to better understand the internal microstructure of the composite.

The scalar (electrostatic) approximation is valid only for particles much smaller than the exciting wavelength. The EMT presented here takes into account both the microstructure and finite size effects in a self-consistent fashion. Specifically, two scenarios were examined, one in which $ka \to 0$ in which the conditionally averaged electric field can be obtained by the solution of the Laplace equation for the electrostatic potential (Scalar EMT) and a more general case for finitely large spheres for which a solution of vector Helmholtz equation for **E** is required (Vector EMT).

Resonance conditions for individual particles were found to depend on κ and ϕ. In the limit as $ka \to 0$, the scaling of the particle polarizability at resonance with ϕ depends on the microstructure. A well-separated random composite has an ε_{eff} resonance when $\beta \approx 1/\phi$. In contrast, for random hard-sphere composite the resonance condition is given by $\beta \approx 2/\sqrt{\phi}$. Hence, for a given ϕ, the resonance peak is more red-shifted for random systems. For finite sized spheres, the vector EMT problem was solved numerically to obtain the a quadratic approximation for ε_{eff} as a function of ϕ. As the particle size is increased, ε_{eff} vs. λ curve exhibit multiple peaks corresponding to quadrupolar, octupolar, and higher order resonances in addition to the dipolar resonance. Size effect on ε_{eff} becomes significant when $\left|\beta^2 \left(k^* a\right)^3\right|$ is $O(1)$. Hence, for composites consisting of high conductivity metals such as Ag in a medium with large refractive index in the visible range such as TiO_2, ZnO and Si, size effects could manifest even for particle diameters of a few 10s of nm.

Particle-effective medium coupling gives rise to a non-Lorentzian resonance behavior in ε_{eff}. In order to characterize the resonant optical response in the κ - ϕ space, a "phase diagram" was constructed. Three regions were identified based on the lineshape of $\Im(\varepsilon_{eff})$: (i). Lorentzian (symmetric peak), (ii). Fano (distinctly asymmetric peak), and (iii). Bruggeman (broad). For an Ag NPs in a high refractive index medium, Fano resonance region is enveloped by the Lorentzian (large κ or large ϕ) and Bruggeman (small κ or small ϕ) regions. Overall, the predictions of the EMT are in qualitative agreement with experimental trends observed for plasmonic composites [51]. This work motivates experimental investigations to quantify the effect of volume fraction on the optical response of plasmonic nanocomposites with well-characterized microstructures. As discussed in Appendix B, the EMT presented here can be extended to describe linear optical response of polydisperse and multiple species systems by adapting the methodology described by Koo and Sangani [71]. Further, extension of the EMT to predict non-linear optical properties could be done by utilizing the approach adopted by Garcia et al. [82].

APPENDIX 5A: C_N AND D_N

Mie coefficients, c_n and d_n, for **E** inside a particle in a layered sphere geometry shown in Fig. 1 are discussed in §3. Hightower and Richardson showed that they can be calculated in the following fashion [44].

$$c_n = \left[\frac{k_p\psi_n(k_m a) - B_n k_p \chi_n(k_m a)}{k_m\psi_n(k_p a)}\right]\left[\frac{k_m\psi_n(k_{eff} R) - b_n k_m \zeta_n(k_{eff} R)}{\psi_n(k_m R) - B_n \chi_n(k_m R)}\right] \tag{5.33a}$$

and

$$d_n = \left[\frac{\psi_n(k_m a) - A_n \chi_n(k_m a)}{\psi_n(k_p a)}\right]\left[\frac{\psi_n(k_{eff} R) - a_n \zeta_n(k_{eff} R)}{\psi_n(k_m R) - A_n \chi_n(k_m R)}\right]. \tag{5.33b}$$

Here, $k_\nu, \nu = p,m,eff$ denotes the wavenumber in the particle, medium and effective medium respectively. Particle radius is a and R is the shell radius as shown in Fig. 1. Riccati-Bessel functions ψ_n, χ_n and ζ_n are defined as:

$$\psi_n(z) \equiv z j_n(z), \tag{5.34a}$$

$$\chi_n(z) \equiv -z y_n(z) \tag{5.34b}$$

and

$$\zeta_n(z) \equiv z h_n^{(1)}(z). \tag{5.34c}$$

Here, j_n , y_n and $h_n^{(1)}$, respectively, are the regular, singular and outward propagating spherical Bessel functions. Note that spherical Hankel functions of the first kind are defined as: $h_n^{(1)} \equiv j_n + iy_n$ [45]. The coefficients A_n and B_n have the following form:

$$A_n = \frac{k_m \psi_n(k_m a)\psi_n'(k_p a) - \psi_n'(k_m a)\psi_n(k_p a)}{k_m \chi_n(k_m a)\psi_n'(k_p a) - \chi_n'(k_m a)\psi_n(k_p a)} \tag{5.35a}$$

and

$$B_n = \frac{k_m \psi_n'(k_m a)\psi_n(k_p a) - \psi_n(k_m a)\psi_n'(k_p a)}{k_m \chi_n(k_m a)\psi_n'(k_p a) - \chi_n'(k_m a)\psi_n(k_p a)}. \tag{5.35b}$$

The primes in Eqs. A3 denote a differentiation. The coefficients a_n and b_n in Eqs. A1 have the following form:

$$a_n = \frac{\psi_n(k_{eff} R)\left[\psi_n'(k_m R) - A_n \chi_n'(k_m R)\right] - k_m \psi_n'(k_{eff} R)\left[\psi_n(k_m R) - A_n \chi_n(k_m R)\right]}{\zeta_n(k_{eff} R)\left[\psi_n'(k_m R) - A_n \chi_n'(k_m R)\right] - k_m \zeta_n'(k_{eff} R)\left[\psi_n(k_m R) - A_n \chi_n(k_m R)\right]} \tag{5.36a}$$

and

$$b_n = \frac{k_m \psi_n(k_{eff} R)\left[\psi_n'(k_m R) - B_n \chi_n'(k_m R)\right] - \psi_n'(k_{eff} R)\left[\psi_n(k_m R) - B_n \chi_n(k_m R)\right]}{k_m \zeta_n(k_{eff} R)\left[\psi_n'(k_m R) - B_n \chi_n'(k_m R)\right] - k_m \zeta_n'(k_{eff} R)\left[\psi_n(k_m R) - B_n \chi_n(k_m R)\right]}. \tag{5.36b}$$

APPENDIX 5B: EXTENSIONS TO POLYDISPERSE AND/OR MULTIPLE SPECIES COMPOSITES

Let the composite be made of *N* different types of spherical particles. Particle type *q* has a radius a_q, permittivity ε_q and occupies a volume fraction ϕ_q. Note that $\sum \phi_q = 1 - \phi_m$ where ϕ_m is the volume fraction of the matrix. Further, let indicator functions $g_q(\mathbf{r})$ indicate the locations of the q^{th} type of particles. The effective permittivity of such a composite can be expressed as:

$$\varepsilon_{eff} = \varepsilon_m + \sum_{q=1}^{N} \left[(\varepsilon_q - \varepsilon_m) \left\langle g_q \mathbf{E} \right\rangle \right] \tag{5.37}$$

The averaged field inside a q^{th} type particle, $\left\langle g_q \mathbf{E} \right\rangle(\mathbf{r})$, can be evaluated using Eq. 4 by replacing the subscript *p* with *q* and particle centre locations $\mathbf{r}_1$ with $\mathbf{r}_q$. Eq. 8 can be modified in a manner similar to Eq. B1 to give the following objective function $\Lambda(k_{eff}^2)$:

$$\Lambda(k_{eff}^2) = k_{eff}^2 - k_m^2 - \sum_{q=1}^{N} \left[\phi_q (k_q^2 - k_m^2) \Omega_q (k_{eff}^2) \right] \tag{5.38}$$

where, the constants Ω_q need to be evaluated. The conditionally averaged field in the integral of Eq. 4 should be evaluated for each q^{th} type of particle. For this purpose, $\left\langle \mathbf{E}(\mathbf{r}) | \mathbf{r}_q \right\rangle$ can be evaluated by solving Eq. 7 simultaneously for all *q* spheres. The effective medium model of Fig. 1, will now have *q*+1 layers for each q^{th} particle. The layers arise from the terms in the summation in Eqs. B1 and B2.

A bidisperse system is considered here to demonstrate the abovementioned methodology. In this case, a 1^{st} type particle is surrounded by a medium with permittivity ε_m up to a radius R_{11} followed by an effective medium with permittivity $\varepsilon_{eff,1} = \varepsilon_m + \phi_1(\varepsilon_1 - \varepsilon_m)\Omega_1$ up to a radius R_{12} followed by the gross effective medium with permittivity $\varepsilon_{eff} = \varepsilon_m + \phi_1(\varepsilon_1 - \varepsilon_m)\Omega_1 + \phi_2(\varepsilon_2 - \varepsilon_m)\Omega_2$. For a 2^{nd} type particle, the layered structure has the radii and permittivity values of ε_m, R_{21}, $\varepsilon_{eff,2}$, R_{22} and ε_{eff}. The non-dimensional radii can be defined as $\kappa_{qr} \equiv R_{qr}/a_q$ for the r^{th} layer around the q^{th} particle (q = 1, 2). The radii are related to the static structure factors $S_{qr}(\mathbf{0})$ through an expression similar to Eqs. 9 and 10 given by [71]:

$$\kappa_{qr} = \left(\frac{\delta_{qr} - S_{qr}(\mathbf{0})}{\phi_q} \right)^{\frac{1}{3}}. \tag{5.38}$$

In Eq. B3, δ_{qr} is the Kronecker delta. The structure factors are defined in the following manner:

$$S_{qr} = \int \left[P(\mathbf{r}, a_q \middle| \mathbf{0}, a_r) - P(\mathbf{r}, a_q) \right] dV_{\mathbf{r}}. \tag{5.39}$$

Here, $P(\mathbf{r}, a_q \middle| \mathbf{0}, a_r)$ is the probability density of finding a q^{th} type particle at **r** given an r^{th} type of particle at the origin **0**. However, evaluation of $S_{qr}(\mathbf{0})$ is rather complicated even for a bidisperse system as discussed in Ref. [71]. We will note that for hard-sphere random systems, in the limit as $\phi_1 + \phi_2 \to 0$, $S_{qr} = \delta_{qr} - \phi_q(a_q + a_r)^3 / a_q^3$.

6 CONCLUSIONS

In this dissertation, two simple problems related to the analysis of interaction among metallic nanospheres that undergo a plasmon resonance under optical electromagnetic excitation were studied from the perspective of developing fundamental numerical and theoretical insight into the problem of modeling "plasmon enhanced" devices that very a hot research topic at the time of the beginning of the author's doctoral work. Several papers on the topic of how metal spheres interact under the influence of an externally applied optical field, with one another and with substrate, motivated this work. Specifically, the experimental and analytical work of Pillai et al. [8] and Catchpole et al. [37], respectively, in which it was shown that the presence of noble metal nanoparticles on the surface of a Si device, thin film or wafer, lead to an increase in the photocurrent under the influence of the same amount of light fluence; and the analytical work of Garcia et al. [13] in which it was shown that relatively simple effective medium theories or "mixing rules" can be used to model the optical transmittance of space filling composites of plasmonic metal nanoparticles embedded in a transparent dielectric matrix.

The simplest version the nanoparticle coated device is assumed here to be that comprising of a sphere present in the vicinity of a dielectric slab. Further, in order to break the problem down to its bare fundamentals, it was assumed that the diameter of the sphere is such that wave effects can be neglected for the calculation of the effects of field coupling. However, the problem was solved not in the electrostatic condition but rather in the limit as the dimensionless wavenumber in the full wave equation's solution tended to zero. Interestingly, the problem is somewhat comparable to the electrostatic problem and it can be mapped onto the solution of the electrostatic or static heat conduction problem with the use of a linear transformation on the multipole coefficients. A general MATLAB program was developed to

evaluate the field values for a system comprising of several spheres that have different diameters and permittivities. Further, a MATLAB program was developed to visualize the field represented by a set of multipole coefficient. In light of time constraints, neither the general code nor the visualization program were utilized for the purpose of this work. Instead, the specific problem of sphere-semi-infinite slab coupling was studied in detail. There also, the calculations related to the evaluation of the fields on the substrate side were not possible during the course of this doctoral work. Several interesting physical artifacts were uncovered in the seemingly simple problem of sphere-slab coupling. The induced dipole and its resonances as a function of wavelength of incident light were studied in detail. Effects all parameters on the induced dipole were studied. Several new insights into the problem were inferred. These included the events associated with the peak, i.e., peak birth, peak motion and peak disappearance as the sphere was moved closer to the substrate; the fact that horizontal excitation lead to the same effects that were relatively less prominent as compared to the effects associated with vertical excitation; the resonances completely disappeared when the sphere was made to touch the substrate; and that the relatively high optical resistivity of Au and Cu showed almost not peak motion but only an overall increase in the magnitude of the induced dipole moment. It was found a substrate with a relatively large permittivity was required for a stronger coupling in addition to the fact that a relatively large imaginary permittivity of the sphere reduced the special effects. Certain wavelength regions that did not seem accessible for Ag nanospheres seem to become accessible as a result of coupling in conjunction with the angle of incidence. The relative increase in the radiated power of the induced dipoles scales as $\eta \equiv \frac{|S_{1m}|^2_{g>0}}{|S_{1m}|^2_{g\to\infty}}$ due to the substrate effect. The effect of the distance *g* on the in-coupled in the limit as $ka \to 0$ is negligible since it is expected

to contribute through an exponential term given by $\exp[ika(1+g)]$. The change in the induced dipole, however, has a finer scale of dependence on g allowing for a $\eta(\mathrm{g},\lambda)$ factor of change in the in-coupled or trapped power. This very significant for the design of devices in with molecular spacers are used to stabilize the nanospheres prior to their deposition on the substrate [7]. The presence for such spacers in the eventual processed device need to be accounted for with the aid of $\eta(\mathrm{g},\lambda)$.

The problem of several spheres present as inclusions in a 3-dimentional matrix was studied to develop an understanding of how such composites respond to linear electromagnetic excitation. The problem was analyzed, again, in the simplest possible way to develop basic insights into the optical response and resonances within such composites. In addition, a goal was to reconcile several effective medium theories (EMTs) in one fairly general framework under which the structural information of the composite could be incorporated and adjusted. Several EMTs that were and are used in the plasmonics literature were based on the Maxwell-Garnett EMT. The microstructural information, it was found, is actually implicitly incorporated in the Maxwell-Garnett EMT. Two special cases corresponding to a random distribution of the nanospheres were studied in the limit as the spheres were assumed small and when they had a finite radius. The structural information was incorporated using a layered-sphere geometry in which the radii and the constituents of the layers were assigned values based on the radial distribution function of the composite. The composite was such that it filled 3-dimensional space, without an end or boundary. This way, the issues related to the edge effects such as reflection and deviation from the asymptotic behavior of the ensemble averaged fields was avoided. For such a composite, only bulk effective permittivity could be evaluated. It was found that the dimensionless layer radius could be throttled to generate a rich variety of behaviors for a

fixed material system and volume fraction. Because of its connection with the radial distribution function, the generated effective permittivities represented a range in which an actual value may found. One of the bounds of this range corresponded to the Maxwell-Garnett EMT and the other the Bruggeman EMT. These results were succinct only for the ‘Scalar EMT’ that corresponded to small sphere composite. Finite size effects were incorporated in what was called ‘Vector EMT’. First few coefficients in the Taylor expansion of the effective permittivity were evaluated numerically. Optical attenuation was found to become broadband for relatively dense composites for other parameters held fixed. The dependence was found to be highly non-linear for composites in which a single sphere’s response was strong. A stronger response required sufficient permittivity contrast by having a relatively high medium permittivity.

7 REFERENCES

1. N. W. Ashcroft and N. D. Mermin, *Solid state physics* (Holt, Rinehart and Winston, New York, 1976).
2. S. N. Wani, A. S. Sangani, and R. Sureshkumar, "Effective permittivity of dense random particulate plasmonic composites," J. Opt. Soc. Am. B **29**, 1443-1455 (2012).
3. B. R. Johnson, "Light scattering by a multilayer sphere," Appl. Opt. **35**, 3286-3296 (1996).
4. S. A. Maier, *Plasmonics* (Springer Science+Business Media, LLC, [New York], 2007).
5. P. K. Jain, X. Huang, I. H. El-Sayed, and M. A. El-Sayed, "Noble Metals on the Nanoscale: Optical and Photothermal Properties and Some Applications in Imaging, Sensing, Biology, and Medicine," Accounts of Chemical Research **41**, 1578-1586 (2008).
6. H. A. Atwater and A. Polman, "Plasmonics for improved photovoltaic devices," Nat Mater **9**, 205-213 (2010).
7. M. Israelowitz, J. Amey, T. Cong, and R. Sureshkumar, "Spin Coated Plasmonic Nanoparticle Interfaces for Photocurrent Enhancement in Thin Film Si Solar Cells," Journal of Nanomaterials **2014**, 9 (2014).
8. S. Pillai, K. R. Catchpole, T. Trupke, and M. A. Green, "Surface plasmon enhanced silicon solar cells," Journal of Applied Physics **101**, 093105-093108 (2007).
9. J. Vuckovic, M. Loncar, and A. Scherer, "Surface plasmon enhanced light-emitting diode," Quantum Electronics, IEEE Journal of **36**, 1131-1144 (2000).
10. N. J. Halas, S. Lal, W.-S. Chang, S. Link, and P. Nordlander, "Plasmons in Strongly Coupled Metallic Nanostructures," Chemical Reviews **111**, 3913-3961 (2011).

11. B. Luk'yanchuk, N. I. Zheludev, S. A. Maier, N. J. Halas, P. Nordlander, H. Giessen, and C. T. Chong, "The Fano resonance in plasmonic nanostructures and metamaterials," Nat Mater **9**, 707-715 (2010).

12. A. E. Miroshnichenko, S. Flach, and Y. S. Kivshar, "Fano resonances in nanoscale structures," Reviews of Modern Physics **82**, 2257-2298 (2010).

13. H. Garcia, J. Trice, R. Kalyanaraman, and R. Sureshkumar, "Self-consistent determination of plasmonic resonances in ternary nanocomposites," Physical Review B **75**, 045439 (2007).

14. T. Cong, S. N. Wani, P. A. Paynter, and R. Sureshkumar, "Structure and optical properties of self-assembled multicomponent plasmonic nanogels," Applied Physics Letters **99**, 043112-043112-043113 (2011).

15. S. Torkamani, S. N. Wani, Y. J. Tang, and R. Sureshkumar, "Plasmon-enhanced microalgal growth in miniphotobioreactors," Applied Physics Letters **97**, 043703-043703 (2010).

16. R. F. Harrington, *Time-harmonic electromagnetic fields* (IEEE Press, New York, 2001).

17. R. F. Harrington, *Time-harmonic elektromagnetic fields* (IEEE Press, New York, 2001).

18. M. Abramowitz and I. A. Stegun, *Handbook of mathematical functions : with formulas, graphs, and mathematical tables* (Dover Publications, New York, 1970).

19. M. Epton and B. Dembart, "Multipole Translation Theory for the Three-Dimensional Laplace and Helmholtz Equations," SIAM Journal on Scientific Computing **16**, 865-897 (1995).

20. G. Mo and A. S. Sangani, "A method for computing Stokes flow interactions among spherical objects and its application to suspensions of drops and porous particles," Physics of Fluids (1994-present) **6**, 1637-1652 (1994).

21. A. S. Sangani, "A pairwise interaction theory for determining the linear acoustic properties of dilute bubbly liquids," Journal of Fluid Mechanics **232**, 221-284 (1991).

22. "Mathworks Inc.", retrieved www.mathworks.com.

23. "Tikhonov Regularization", retrieved 05/21/2014, http://en.wikipedia.org/wiki/Tikhonov_regularization.

24. M. Polyanskiy, "Refractive Index Database," (2014).

25. C. Kittel, *Introduction to solid state physics* (Wiley, New York, 1966).

26. "Si Properties" (Ioffe Institute), retrieved September, 2014, http://www.ioffe.ru/SVA/NSM/Semicond/Si/index.html.

27. S. C. Warren and E. Thimsen, "Plasmonic solar water splitting," Energy & Environmental Science **5**, 5133-5146 (2012).

28. Z. Liu, W. Hou, P. Pavaskar, M. Aykol, and S. B. Cronin, "Plasmon Resonant Enhancement of Photocatalytic Water Splitting Under Visible Illumination," Nano Letters **11**, 1111-1116 (2011).

29. S. Pillai, F. J. Beck, K. R. Catchpole, Z. Ouyang, and M. A. Green, "The effect of dielectric spacer thickness on surface plasmon enhanced solar cells for front and rear side depositions," Journal of Applied Physics **109**, - (2011).

30. E. Ozbay, "Plasmonics: Merging Photonics and Electronics at Nanoscale Dimensions," Science **311**, 189-193 (2006).

31. H. A. Atwater, "The promise of plasmonics," Sci Am **296**, 56-63 (2007).

32. W. Lukosz and R. E. Kunz, "Light emission by magnetic and electric dipoles close to a plane interface. I. Total radiated power," J. Opt. Soc. Am. **67**, 1607-1615 (1977).

33. M. Duval Malinsky, K. L. Kelly, G. C. Schatz, and R. P. Van Duyne, "Nanosphere Lithography: Effect of Substrate on the Localized Surface Plasmon Resonance Spectrum of Silver Nanoparticles," The Journal of Physical Chemistry B **105**, 2343-2350 (2001).

34. A. Pinchuk, A. Hilger, G. von Plessen, and U. Kreibig, "Substrate effect on the optical response of silver nanoparticles," Nanotechnology **15**, 1890 (2004).

35. Y. Wu and P. Nordlander, "Finite-Difference Time-Domain Modeling of the Optical Properties of Nanoparticles near Dielectric Substrates†," The Journal of Physical Chemistry C **114**, 7302-7307 (2009).

36. M. S. Golden, A. C. Bjonnes, and R. M. Georgiadis, "Distance- and Wavelength-Dependent Dielectric Function of Au Nanoparticles by Angle-Resolved Surface Plasmon Resonance Imaging," The Journal of Physical Chemistry C **114**, 8837-8843 (2010).

37. K. R. Catchpole and S. Pillai, "Absorption enhancement due to scattering by dipoles into silicon waveguides," Journal of Applied Physics **100**, - (2006).

38. L. H. B. Novotny, *Principles of nano-optics* (Cambridge University Press, Cambridge, 2006).

39. J. A. Kong, "6.635 Advanced Electromagnetism, Spring 2003. (MIT OpenCourseWare: Massachusetts Institute of Technology)," (2003).

40. J. Biener, G. W. Nyce, A. M. Hodge, M. M. Biener, A. V. Hamza, and S. A. Maier, "Nanoporous plasmonic metamaterials," Advanced Materials **20**, 1211-1217 (2008).

41. V. E. Ferry, J. N. Munday, and H. A. Atwater, "Design Considerations for Plasmonic Photovoltaics," Advanced Materials **22**, 4794-4808 (2010).

42. S. A. Maier, M. L. Brongersma, P. G. Kik, S. Meltzer, A. A. G. Requicha, and H. A. Atwater, "Plasmonics -- A Route to Nanoscale Optical Devices," Advanced materials. **13**, 1505 (2001).

43. W. A. Murray and W. L. Barnes, "Plasmonic Materials," Advanced Materials **19**, 3771-3782 (2007).

44. J. Yao, A.-P. Le, S. K. Gray, J. S. Moore, J. A. Rogers, and R. G. Nuzzo, "Functional Nanostructured Plasmonic Materials," Advanced Materials **22**, 1102-1110 (2010).

45. P. R. West, S. Ishii, G. V. Naik, N. K. Emani, V. M. Shalaev, and A. Boltasseva, "Searching for better plasmonic materials," Laser & Photonics Reviews **4**, 795-808 (2010).

46. J. Trice, D. Thomas, C. Favazza, R. Sureshkumar, and R. Kalyanaraman, "Pulsed-laser-induced dewetting in nanoscopic metal films: Theory and experiments," Physical Review B **75**, 235439 (2007).

47. T. Li, J. Moon, A. A. Morrone, J. J. Mecholsky, D. R. Talham, and J. H. Adair, "Preparation of Ag/SiO2 Nanosize Composites by a Reverse Micelle and Sol−Gel Technique," Langmuir **15**, 4328-4334 (1999).

48. D. D. Smith, L. A. Snow, L. Sibille, and E. Ignont, "Tunable optical properties of metal nanoparticle sol–gel composites," Journal of Non-Crystalline Solids **285**, 256-263 (2001).

49. L. M. Liz-Marzán, "Tailoring Surface Plasmons through the Morphology and Assembly of Metal Nanoparticles," Langmuir **22**, 32-41 (2005).

50. A. Biswas, O. C. Aktas, U. Schurmann, U. Saeed, V. Zaporojtchenko, F. Faupel, and T. Strunskus, "Tunable multiple plasmon resonance wavelengths response from

multicomponent polymer-metal nanocomposite systems," Applied Physics Letters **84**, 2655-2657 (2004).

51. Z. Liu, H. Wang, H. Li, and X. Wang, "Red shift of plasmon resonance frequency due to the interacting Ag nanoparticles embedded in single crystal SiO[sub 2] by implantation," Applied Physics Letters **72**, 1823-1825 (1998).

52. D. Erickson, D. Sinton, and D. Psaltis, "Optofluidics for energy applications," Nat Photon **5**, 583-590 (2011).

53. O. Popov, A. Zilbershtein, and D. Davidov, "- Random lasing from dye-gold nanoparticles in polymer films: Enhanced gain at the surface-plasmon-resonance wavelength," **- 89**(2006).

54. T. Okamoto, I. Yamaguchi, and T. Kobayashi, "Local plasmon sensor with gold colloid monolayers deposited upon glass substrates," Opt. Lett. **25**, 372-374 (2000).

55. A. Dawson and P. V. Kamat, "Semiconductor−Metal Nanocomposites. Photoinduced Fusion and Photocatalysis of Gold-Capped TiO2 (TiO2/Gold) Nanoparticles," The Journal of Physical Chemistry B **105**, 960-966 (2001).

56. C. F. Bohren and D. R. Huffman, *Absorption and Scattering of Light by Small Particles* (John Wiley & Sons, New York [etc.], 1998).

57. C. Oubre and P. Nordlander, "Optical Properties of Metallodielectric Nanostructures Calculated Using the Finite Difference Time Domain Method," The Journal of Physical Chemistry B **108**, 17740-17747 (2004).

58. A. Taflove and S. C. Hagness, *Computational electrodynamics : the finite-difference time-domain method* (Artech House, Boston, 2005).

59. F. Kaminski, V. Sandoghdar, and M. Agio, "Finite-Difference Time-Domain Modeling of Decay Rates in the Near Field of Metal Nanostructures," Journal of Computational and Theoretical Nanoscience **4**, 635-643.

60. T. C. Choy, *Effective medium theory* (Oxford University Press, Oxford, 1999).

61. Garnett, "Colours in Metal Glasses and in Metallic Films," Royal Society of London Philosophical Transactions Series A **203**, 385-420 (1904).

62. P. Mallet, C. A. Guérin, and A. Sentenac, "Maxwell-Garnett mixing rule in the presence of multiple scattering: Derivation and accuracy," Physical Review B **72**, 014205 (2005).

63. R. Ruppin, "Evaluation of extended Maxwell-Garnett theories," Optics Communications **182**, 273-279 (2000).

64. V. Yannopapas, "Effective-medium description of disordered photonic alloys," J. Opt. Soc. Am. B **23**, 1414-1419 (2006).

65. D. M. a. A. N. W. Wood, "Effective medium theory of the optical properties of small particle composites," Philos. Mag. **35**, 269-280 (1977).

66. P. D. M. Spelt, M. A. Norato, A. S. Sangani, M. S. Greenwood, and L. L. Tavlarides, "Attenuation of sound in concentrated suspensions: theory and experiments," Journal of Fluid Mechanics **430**, 51-86 (2001).

67. G. Mo and A. Sangani, "- A method for computing Stokes flow interactions among spherical objects and its application to suspensions of drops and porous particles," - **6**(1994).

68. T. L. Dodd, D. A. Hammer, A. S. Sangani, and D. L. Koch, "Numerical simulations of the effect of hydrodynamic interactions on diffusivities of integral membrane proteins," Journal of Fluid Mechanics **293**, 147-180 (1995).

69. A. Sangani and C. Yao, "- Bulk thermal conductivity of composites with spherical inclusions," **- 63**(1988).

70. A. S. Sangani and W. Lu, "Elastic coefficients of composites containing spherical inclusions in a periodic array," Journal of the Mechanics and Physics of Solids **35**, 1-21 (1987).

71. S. Koo and A. S. Sangani, "Effective-medium theories for predicting hydrodynamic transport properties of bidisperse suspensions," Phys. Fluids **14**(2002).

72. N. F. Carnahan and K. E. Starling, "Equation of State for Nonattracting Rigid Spheres," The Journal of Chemical Physics **51**, 635-636 (1969).

73. S. Chandrasekhar, *Hydrodynamic and hydromagnetic stability* (Clarendon Press, Oxford, 1961).

74. R. L. Hightower and C. B. Richardson, "Resonant Mie scattering from a layered sphere," Appl. Opt. **27**, 4850-4855 (1988).

75. D. Zwillinger, *Handbook of integration* (Jones and Bartlett, Boston, 1992).

76. C. T. Kelley, *Iterative methods for linear and nonlinear equations* (Society for Industrial and Applied Mathematics, Philadelphia, 1995).

77. A. H. Sihvola, *Electromagnetic mixing formulas and applications* (Institution of Electrical Engineers, London, [Angleterre], 1999).

78. M. G. Blaber, M. D. Arnold, and M. J. Ford, "Search for the Ideal Plasmonic Nanoshell: The Effects of Surface Scattering and Alternatives to Gold and Silver," The Journal of Physical Chemistry C **113**, 3041-3045 (2009).

79. K. L. Kelly, E. Coronado, L. L. Zhao, and G. C. Schatz, "The Optical Properties of Metal Nanoparticles: The Influence of Size, Shape, and Dielectric Environment," The Journal of Physical Chemistry B **107**, 668-677 (2002).

80. E. D. Palik, *Handbook of optical constants of solids* (Academic Press, Orlando, 1985).

81. U. Fano, "Effects of Configuration Interaction on Intensities and Phase Shifts," Physical Review **124**, 1866 (1961).

82. H. Garcia, R. Kalyanaraman, and R. Sureshkumar, "Nonlinear optical properties of multi-metal nanocomposites in a glass matrix," Journal of Physics B: Atomic, Molecular and Optical Physics **42**, 175401 (2009).

VITA

Author's Name: Satvik Navin Wani

Country of Origin: India

Degrees Awarded: Ph. D., Chemical Engineering, Syracuse University, Syracuse, USA (2010-15)

M. S., Energy, Environmental and Chemical Engineering, Washington University in St. Louis, St. Louis, USA (2008-10)

M. Tech and B. Tech (Dual Degree Program), Metallurgical Engineering and Materials Science, Indian Institute of Technology, Mumbai, India (2001-06)